Estimate of Atmospheric Predictability and Development of Prediction Model Using Ensemble Forecast Assimilation in Nonlinear Dynamical System

January 2004

Daisuke NOHARA

Estimate of Atmospheric Predictability and Development of Prediction Model Using Ensemble Forecast Assimilation in Nonlinear Dynamical System

A Dissertation Submitted to
the Graduate School of Life and Environmental Science,
the University of Tsukuba
in Partial Fulfillment of the Requirements
for the Degree of Doctor of Philosophy in Science

Daisuke NOHARA

Contents

Abstract

In this study, a limit of predictability for the atmosphere is estimated based on analog weather maps in the historical data, and a new type of ensemble forecast assimilation technique is developed in order to improve the forecast skill in the nonlinear dynamical system. The limit of the predictability (denoted as P) is defined as the time taken for the initial difference (E_0) of the analog pair to reach the climate noise level which is defined by one standard deviation from the long term mean of the fluctuation in the observed atmosphere. Although a total of 185,547,600 pairs of the weather maps are searched, there are no good analog pairs to investigate the difference growth rate for a sufficiently small E_0 of the analog pairs. For this reason, the behavior of E_0 is explained by a quadratic error growth model. Regressing the quadratic error growth model to the scattergram between P and E_0, it is estimated that P would extend 2.88 days when E_0 is reduced to $1/e$ for sufficiently small E_0. The limit of predictability P varies depending on variable by the atmospheric boundary condition such as El Niño, La Niña, Pacific/North American (PNA), and North Atlantic Oscillation (NAO). In the case of PNA+ and NAO-, the differences of the analog pairs grow slower than the average showing the e-folding time of 3.17 and 3.07 days, respectively. Conversely, in the case of La Niña and PNA-, the differences grow faster than the average showing the e-folding time of 2.72 and 2.69 days, respectively. These results are also verified by hindcast datasets.

The forecast assimilation is an analysis technique in which a true value contained in each ensemble forecast is accumulated into a single assimilated forecast such as a data assimilation. For the experiments, we used a Lorenz model, and a Kalman filter is applied for the forecast assimilation. The experiments are started by calculating 101 members of the ensemble forecast in which the initial error with Gaussian distribution is superimposed around the truth, and one of the members is arbitrarily selected as a control forecast. The experiments of the forecast assimilation are repeated 5000 times for different sectors of the solution trajectory to obtain the statistical significance of the results. The distribution of the ensemble members is stretched by a linear error growth at the beginning of the forecast. After that, the nonlinear effect becomes dominant to distort the distribution. The forecast assimilation is then started when the errors of the ensemble forecasts have grown to a certain threshold. It is demonstrated that the forecast skill of the assimilated forecast is always superior to the control forecast. In the range of the small root mean square (RMS) error of the ensemble forecast, the skill of the assimilated forecast is inferior to the ordinary ensemble mean. However, for the sufficiently large RMS error before the saturation, it is shown that the skill of the assimilated forecast is superior to the ensemble mean. The result suggests that the forecast assimilation is one of the viable approaches to the medium or extended range forecast.

Key Words: 3D-Var, atmospheric predictability, boundary condition, forecast assimilation, hindcast, Kalman filter, initial condition, Lorenz model

List of Figures

List of Tables

Chapter 1

Introduction

Recently, a numerical weather prediction system is indispensable to a weather forecast. Since the numerical weather prediction system has been developing through the improved representation of physical processes, the utilization of more accurate methods of data assimilation, the increased availability of data (e.g., satellite, aircraft, etc.), and the increased power of supercomputers, the predictability of the weather forecast is nowadays increasing (Kalnay 2002). The predictability limit of the global forecast is about 8 days (Kalnay 2002). While the forecasting skill has steadily increased, and the range of skillful forecasts has been steadily extended, it has also been established that the deterministic prediction of the instantaneous state of the weather is impossible for an extended range. This limit of predictability was first pointed out by Lorenz (1963) who subsequently demonstrated that, due to the inherent nature of instability and nonlinearity, atmospheric flows with only slightly different initial states will depart from each other and evolve eventually to flows that are just randomly related. It is our contention that deterministic medium-range forecasting may be impossible beyond two weeks of the chaotic barrier, even if we can have a perfect prediction model.

In this matter, there are two major issues for the weather forecasting: developing a better numerical weather prediction system, and investigating the limit of the atmospheric predictability. This study deals with these two subjects.

1.1 Atmospheric Predictability

Previous studies of the limit of the predictability for the atmosphere are divided into two groups; one with empirical approach using analog pairs in the historical weather maps and the other with dynamical approach using numerical model experiments (Lorenz 1969a). The empirical approach estimates the limit of the predictability of the atmosphere based on the growth rate of the difference between the two analog weather maps (e.g., Lorenz 1969b; Gutzler and Shukla 1984). Although Lorenz (1969b) can not find good analog pairs, he presumed that the small difference of the good analog pairs would be double in about 2.5 days. Similar to Lorenz's approach, Gutzler and Shukla (1984) estimates the doubling time as nearly 8 days. It is difficult, however, to estimate the predictability for small error using this approach because it is highly improbable that the truly good analog pair will be found in the historical data (van den Dool 1994).

On the other hand, the dynamical approach estimates the limit of the predictability with "identical twin" experiments in which two integrations, started from slightly different initial conditions, diverge from each other, providing information about the limit of the predictability (e.g., Lorenz 1982; Dalcher and Kalnay 1987; Schubert and Suarez 1989; Chen 1989; Simons et al. 1995). Lorenz (1982) estimates a doubling time for small errors of only 2.4 days, using a quadratic error growth model constructed from the growth of the root mean square (RMS) error in 500 hPa geopotential height between two forecasts. With

the same approach, the doubling time for the recent forecast model developed by European Center for Medium-Range Weather Forecasts (ECMWF) appears to be around 1.5 days (Simons et al. 1995). Dalcher and Kalnay (1987), however, points out that the doubling time of small error is not a good measure of the error growth because the result is very sensitive for small error to the quadratic error growth model. Therefore, they defined the limit of predictability as the time taken for the error to reach 95 % of the climatological mean range of fluctuation in 500 hPa geopotential height, and found that the limit of predictability is close to 20 days in winter. In a similar way as Dalcher and Kalnay (1987), Chen (1989) adopted the limit of the predictability as the time taken for the error to reach one standard deviation from the climatological mean range of fluctuation, and found the limit of the predictability is about 14 days without using the Lorenz's error growth model. However, in order to extrapolate his result to the small initial error, Chen (1989) assumes a linear relationship between the initial error and the limit of predictability. Such a linear relationship is used further by Toth (1991) in a study of predictability based on circulation analogues. From those experiments, it is concluded that the limit of predictability is of the order of two weeks. Nohara and Tanaka (2001) suggests that the limit of predictability obeys a logarithmic function rather than a linear function of the initial error using the historical weather maps and the barotropic model produced by Tanaka (1991; 1998). The predictability for the barotropic atmosphere increases about 6.3 days when the initial error is reduced to 1/10 (with the e-folding time of 2.8 days).

Meanwhile, the forecast skill of the seasonal mean is higher during El Niño winter than normal winter (Chen and van den Dool 1997; Barsugli et al. 1999; Shukla et al. 2000). The El Niño is defined by that the warm sea surface temperature (SST) anomaly appears over the eastern tropical Pacific and persists for a few month or more. Conversely, the La Niña is defined by that the cold SST anomaly appears over the eastern tropical Pacific and persists for a few month or more. The strong external forcings, such as El Niño

and La Niña, significantly impact the planetary scale circulation over the extratropics (e.g., Lau and Nath 1994). The forcings derive some persistent circulation pattern such as the Pacific-North American (PNA) pattern. The PNA is one of the most prominent teleconnection patterns and located over the North Pacific and over North America. Additionally, the North Atlantic Oscillation (NAO), which is associated with a north-south dipole structure in the pressure field over the North Atlantic, is also considered as one of the most prominent teleconnection patterns. Since the synoptic scale cyclone activity over the extratropics directly attributes to the initial error growth for the operational forecasting, it is expected that the external forcings indirectly affect the initial error growth. In previous studies using the numerical experiments, the initial errors during the positive phase of PNA years have smaller growth rate than the negative phase of PNA (Lin and Derome 1996; Sheng 2002).

The dynamical approaches are the primary method for the estimate of the atmospheric predictability. However, the results using the dynamical approaches potentially depend on the characteristics of the numerical model. Therefore, it is necessary to estimate the atmospheric predictability interms of the empirical approach with the historical analog pairs.

1.2 Development of Prediction System

In order to extend the predictable period, many operational weather forecasting centers have been developing the numerical forecasting system (reviewed by Kalnay et al. 1998) in the following three factors: (1) the improvement of the numerical models (high resolution and nonhydrostatic model, improved physical processes), (2) the development of the data

assimilation system, which result in improved initial conditions for the models, (3) development of the ensemble forecast system in which several model forecasts are performed by introducing perturbations in the initial conditions or in the models themselves. Figure 1.1 shows the historic evolution of the operational forecast skill by the National Centers for Environmental Prediction (NCEP) forecast models over the North America. The S1 score (Teweles and Wobus 1954) measures the relative error in the horizontal gradient of the height of the 500 hPa for the forecasts over the North America. The values S1=70% and S1=20% are empirically determined to correspond respectively to a useless and a perfect forecast when the score was designed. The forecast skill is gradually advanced by the evolution of the numerical models and data assimilation. Figure 1.1 also shows that the 72-h forecasts of today are as skillful as the 36-h forecasts 10-20 years ago.

For further improvement of the forecast skill, an ensemble of numerical forecasts from slightly perturbed initial conditions is used for the medium range forecasts at many operational weather forecasting centers. Since the ensemble forecast is based on a probabilistic weather prediction, it is necessary to create a probability density function as diversely as possible for the ensemble members. Therefore, at ECMWF, the ensemble forecast system is constructed by an initial perturbation that is a linear combinations of singular vectors (Molteni et al. 1996; Buizza 1997; Gelaro et al. 1997; Buizza et al. 2000). The singular vectors specify the directions of the greatest growth of the linearized system over a predetermined time interval. At the NCEP, a breeding method is introduced for the ensemble forecast system in which the initial perturbation is a linear combination of bred vectors (Toth and Kalney 1993, 1997). The bred vectors are perturbations created in directions where past forecast errors have grown rapidly. Additionally, Houtekamer and Derome (1995) introduced a perturbed observation method. This method adds random errors to the observation and includes different parameters in the physical parameterization of the model in different ensembles. Hamill et al. (2000) shows that the perturbed observation

method performs better than the singular vector or breeding method. These ensemble forecasts have contributed to the progress of the medium range forecast in the 1990's. Recently, a multi-model ensemble system has become more popular (Harrison et al. 1999; Krishnamurti et al. 1999; Doblas-Reyes et al. 2000; Palmer et al. 2000; Kenneth et al. 2002; Alhamed and Lakshmivarahan 2002). The ensemble members are constructed by many operational forecasts from different operational centers that run competitive state-of-the-art operational analysis and model forecasts. The ensemble average of the multi-model ensemble is more skillful than the best individual forecasts (Fritsch et al. 2000).

The skill of the ensemble forecasts is improved by statistical analyses as an ensemble mean and an ensemble spread (Murphy 1988). Krishnamurti et al. (1999) has shown that if the multi-model ensemble includes correction of the systematic errors by regression (called superensemble), the seasonal forecast skill (Krishnamurti et al. 2000; Kharin and Zwier 2002) and Atlantic hurricane forecast (Williford et al. 2003) is significantly improved. Additionally, a cluster analysis of multi-model ensemble is suggested by Alhamed and Lakshmivarahan (2002).

Using these ensemble forecasts, some statistical analyses like the ensemble mean perform well in the nonlinear system. Certainly, if the ensemble members distribute hyper cubic or ellipsoid around the truth, the location of the ensemble mean indicates the truth and it becomes the best forecast. Nevertheless, the actual distribution is folded by the nonlinear effect as the forecast progresses. Then, the ensemble mean is detached from the center of the distribution of the ensemble members, since the ensemble mean is only the average of the ensemble members. If one statistical analysis includes not only the temporal result of the ensemble members but also the time evolution with dynamical process of the forecast error growth, it may be expected that the skill of the new analyzed

forecast is better than the ordinary ensemble mean. For the statistical and dynamical analysis, the ensemble members are accumulated into a single forecast by a Kalman filter (Kalman and Bucy 1961) as in the atmospheric and oceanic data assimilation. This is called forecast assimilation (Nohara and Tanaka 2003). The Kalman filter assimilates the explicit description of the evolution of the forecast error, so it is competent for the forecast assimilation.
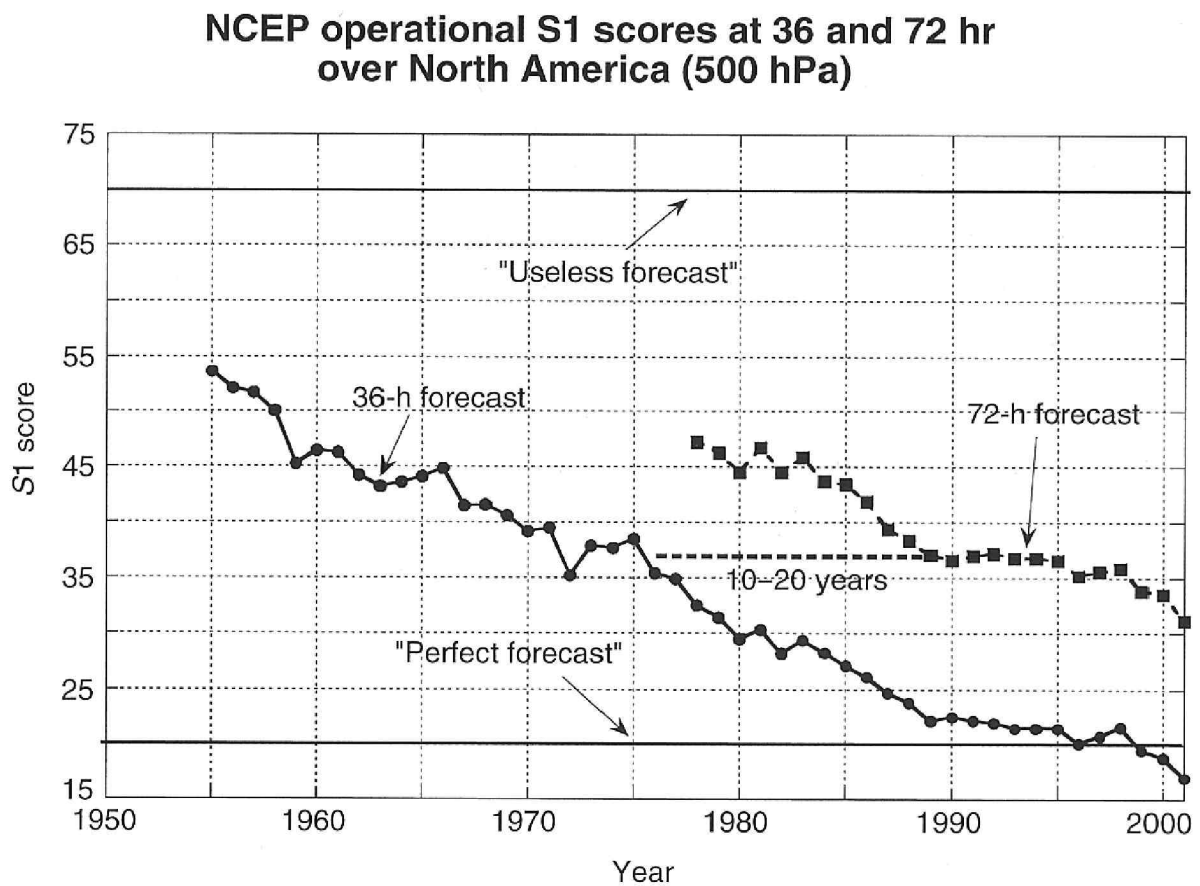
Figure 1.1: Historical evolution of the operational forecast skill of the NCEP models over the North America (500 hPa). The S1 score measures the relative error in the horizontal pressure gradient, averaged over the region on interest. The values S1=70% and S1=20% were empirically determined to correspond respectively to a useless and a perfect forecast when the score was designed. (From Kalnay 2002)

1.3 Objectives

The purpose of this studies are to estimate the atmospheric predictability using empirical approach and to construct a new technique of the forecast assimilation using the ensemble members in order to improve the forecast skill. The atmospheric predictability is estimated as follows. First, many good analog pairs are sought in the observed atmosphere using historical dataset of NCEP/National Center for Atmospheric Research (NCAR) reanalysis. The behavior of the difference for the good analog pairs is the key to estimate the atmospheric predictability. Next, the roles of the boundary conditions, such as El Niño, La Niña, and the basic flow patterns, such as PNA, and NAO, for the atmospheric predictability are investigated using the observed atmospheric data. Finally, the roles of the boundary condition and the basic flow patterns for the atmospheric predictability are verified by the hindcast datasets.

In the next, the forecast assimilation is developed and verified as follows. In order to examine the performance of the forecast assimilation technique, this study uses a simple dynamical system of the Lorenz model (Lorenz, 1963), which has been comprehensively studied for the chaotic behavior and the nonlinear dynamics (Sparrow 1982; Mukougawa et al. 1991). For the forecast assimilation of the ensemble members, this study uses three dimensional variational analysis (3D-Var) and the Kalman filter formulated by Kalman and Bucy (1961).

This paper is organized in chapters as follows. In Chapter 2, the method and results of the estimate of the atmospheric predictability are presented by the previous observation and hindcast datasets. In Chapter 3, the forecast assimilation is introduced and the performance of the forecast assimilation is assessed for the Lorenz model. The results of

the atmospheric predictability and the forecast assimilation are discussed in Chapter 4.

Finally, the conclusions are given in Chapter 5.

Chapter 2

Atmospheric Predictability

2.1 Experimental Design

2.1.1 Data

The dataset used in this study is NCEP/NCAR reanalysis. A detailed documentation is described by Kalnay et al. (1996) and Kistler et al. (2001). The reanalysis data assimilation system includes the NCEP global spectral model operational in 1995, with 28 sigma vertical levels and a triangular truncation of 62 waves, equivalent to about 210 km horizontal resolution. The analysis scheme is a three-dimensional variational (3D-VAR) scheme cast in spectral space denoted by the spectral statistical interpolation (Parrish and Derber 1992). The dataset for this study contains four times daily (00Z, 06Z, 12Z, 18Z) meteorological variables of geopotential height at 2.5° longitude by 2.5° latitude grids on 500 hPa for 55 years from January 1948 though December 2002.

Also used is Optimum Interpolation Sea Surface Temperature (OI-SST) produced by Reynolds and Smith (1994) from 1950 though 2002. The dataset contains December-

January-February (DJF) mean of averaged SST over the Niño-3.4 region (5.0°N-5.0°S, 170°-120°W).

2.1.2 Seeking Analog Pair

First, seeking for the analog pair in the past observed atmosphere is necessary to estimate the atmospheric predictability. The difference between the analogous two weather maps is increasing as the time proceeds. Then if we can find the sufficient small difference of the analog pair, the subsequent increasing difference with respect to time suggests the inherent error growth rate in the atmosphere. Therefore, the key to the successful analysis for discussing the error growth is to search for sufficiently good analog pairs.

In this study, the analog is defined by a root mean square (RMS) difference between the two weather maps. For each two maps $Z(a)$ and $Z(b)$, where $Z_i(a)$ and $Z_i(b)$ are 500 hPa geopotential height scaled by the cosine of latitude for grid points $i = 1, 2, ..., N$ (N the total number of gridpoints), the area-weighted RMS difference is given by

$$\text{RMS} = \left(\frac{1}{w} \sum_{i=1}^{N} \left(Z_i(b) - Z_i(a) \right)^2 \right)^{1/2}, \tag{2.1}$$

where

$$w = \sum_{i=1}^{N} \cos \theta_i. \tag{2.2}$$

The RMS is calculated for 20 °N to 90 °N region. The RMS score has a minimum value (RMS=0) for a perfect analogous pair. So, the best analog pair is the minimum RMS among the all combinations of the weather maps.

Although the similar approach was attempted by Lorenz (1969b), Gutzler and Shukla (1984), and Toth (1991), they failed to determine the limit of predictability since they

could not find sufficient analog pairs for 500 hPa geopotential height to discuss the atmospheric predictability. From other method, van den Dool (1994) showed that it was necessary to take a historical data library of the order 10^{30} years in order to find two observed flows that match within the current observation error over the Northern Hemisphere. It is shown therefore that estimating the atmospheric predictability is difficult only using the analog pair. It is necessary to modify the theoretical error growth model for estimating the atmospheric predictability, which is explained in next section.

2.1.3   Quadratic Error Growth Model

In order to estimate the atmospheric predictability, a quadratic error growth model is suggested by Lorenz (1969a, 1982). The error growth model is written as

$$\frac{dE}{dt} = \alpha E - \frac{\alpha}{E_\infty} E^2, \qquad (2.3)$$

where E is the RMS difference in 500 hPa geopotential height between two weather maps, α is a difference growth rate in small E between the analog weather maps, and E_∞ is a saturated difference value that is defined as the climatological mean of the atmospheric fluctuation. The equation allows an exponential growth of difference with a growth rate given by α for small differences for the first term in Eq. (2.3), and the error will saturate for the second term at a sufficiently long time. In previous studies, the difference growth was fitted on this equation to obtain α (Lorenz 1969b; Lorenz 1982; Stroe and Royer 1993; Savijarvi 1995) because it is convenient to understand the behavior of the small difference. However, since the term dE/dt is very sensitive to compute due to the differential form, it is difficult to fit the relation between dE/dt and E for a small difference. Therefore this study attempts to fit the difference growths of the analog pairs on the integrated form of Eq. (2.3).

The integral form of this equation is given by Stroe and Royer (1993) as

$$E = \frac{E_\infty}{1 + \left(\dfrac{E_\infty}{E_0} - 1\right) e^{-\alpha t}}, \tag{2.4}$$

where E_0 is an initial RMS difference between two weather maps. The RMS difference of the analog pair increases as time proceeds, and exceeds a climate noise level E_l which is defined by one standard deviation from the long term mean of the fluctuation in the observed atmosphere. When RMS difference reaches the noise level, it may be no longer considered as an analog pair. For the analogy in the weather prediction, it may be the criterion that the predictability is lost. For this reason, the limit of the predictability P is defined as the time taken for the initial difference E_0 to reach the climate noise level E_l. Following Nohara and Tanaka (2001), Eq. (2.4) is rewritten for the limit of predictability P using E_0 as

$$P = -\frac{1}{\alpha} \left\{ \log \left[\frac{E_0}{E_\infty - E_0} \right] + \log \left[\frac{E_\infty - E_l}{E_l} \right] \right\}. \tag{2.5}$$

Using Eq. (2.5), the regression between P and E_0 derives the error growth rate α. If E_0 is closed to 0, then the relation between P and E_0 will be logarithmic, and $1/\alpha$ indicates an e-folding time of the difference growth. Nohara and Tanaka (2001) confirmed that α can be estimated by using only large initial difference based on the numerical model examinations.

2.1.4   Hindcast Experiments

A hindcast dataset (Hamill et al. 2003) is a retrospective forecast for every day from November 1978 to the present using a frozen version of the operational Medium-Range Forecast model at NCEP, which was an operational forecast model between January and June of 1998. The hindcast is generated by 15 days forecast from 1978 to 2002 using

0000 UTC initial conditions from NCEP/NCAR reanalysis (Kalnay et al. 1996). The dataset for this study contains the daily 15 days hindcast with meteorological variables of geopotential height at 2.5° longitude by 2.5° latitude grids on 500 hPa for 23 winters (DJF) from December 1979 to February 2002.

The hindcast is compared with the NCEP/NCAR reanalysis as the verifying truth. The hindcast skill is indicated by the RMS error, for example a 3 days hindcast from the initial states at 0000 UTC 1 January 2000 is compared with 0000 UTC 4 January 2000 in the NCEP/NCAR reanalysis dataset. Since the initial state of the hindcast is same as the NCEP/NCAR reanalysis, the RMS error of the 0 days hindcast equals to 0 m. However, the error of the hindcast increases over time due to the imperfect model for the forecast, inevitable initial error included in the reanalysis, and the dynamical instability.

2.2 Results

2.2.1 Atmospheric Predictability

In order to estimate the atmospheric predictability, it is necessary to find many good analogous pairs of weather maps. The analog pairs are searched for the four times daily NCEP/NCAR reanalysis during the months of December, January, February – a total of 19170 maps during the 54 years. First, RMS for all combinations of all weather maps are calculated. Following Nohara and Tanaka (2001), every weather map for a single winters is compared with all maps of other winters. This procedure is chosen to ensure that a good analog pair is not merely due to persistence, but actually represents a recurrence of a circulation pattern. The total number of combinations compared by this procedure, 185,457,600, is much larger than that in previous studies.

Figure 2.1 shows the frequency distribution of RMS difference resulted from all combinations of weather maps. The frequency peak is seen about 120 m RMS difference and the average RMS difference for all combinations is 121.84 m. This value corresponds to the expected value of the difference between two randomly chosen weather maps. The standard deviation is 15.01 m, with a larger spread in the higher values. Only 16.1% of the samples in all combinations are less than one standard deviation from the mean. This result implies that it is extremely difficult to find a very analogous pair comparable to the current observation error (about 10 m of RMS).

Table 2.1 contains a sample list of the best ten independent analog pairs. Because some flow patterns persist one day or more, many of the best analog pairs are chosen from the same synoptic situation with one or more days apart. Following Gutzler and Shukla

(1984), the dependent analog pairs are subjectively removed by examining the list of the best analog pairs. The dependent analog pairs are defined as pairs by before and after 10 days from the most analogous date. The total number of the independent analog pair is reduced to 21530. It is found that the best analog pair is about half of the average value of the RMS difference. Figure 2.2 shows the mean geopotential height at 500 hPa for the top 1000 of the independent analog pairs. Marked troughs are located at the east of Asia and North America, and ridges are over the northeastern Pacific and Atlantic. Since the map is similar to the atmospheric climatology of 500 hPa geopotential height during the winter, it is indicated that the map is not averaged by the specific weather pattern as a blocking pattern.

Figure 2.3 shows the distribution of grown difference for the top 1000 of the independent analog pairs for 3 days from the most analogous date. The shaded region indicates that RMS difference of the analog pair easily grows in short time. The regions are located at the northeastern Pacific and the north Atlantic to the Europe, where is well-known as the storm tracks during winter (Hosikins and Hodges 2002).

The similarity of the best analog pair can be confirmed visually. Figure 2.4 illustrates the maps of 500 hPa geopotential heights of the best analog pair for (a) 0600Z 28, January 1956, (b) 0600Z 13, February 1961, (c) the difference between (a) and (b) with negative contours shaded. Their contour interval is 60 m. This pair is very similar over the Atlantic to the Siberia, but not over the North Pacific to the Alaska. The figure shows that the difference in the geopotential height is at most 300 m over North Pacific.

The RMS difference of the best analog pair gradually increases as time proceeds. Figure 2.5 shows the time variation of the RMS difference. The solid curve represents the RMS difference for the best analog pair. The solid and dashed straight lines represent the

climatological mean (121.8 m) and the one standard deviation of atmospheric fluctuation from the mean (106.8 m), respectively. Hereafter, the range above the dashed line is referred to a climatological noise range. The RMS difference linearly increases from the 0th to the 3rd day and reaches the climatological noise range at the 3rd day. After the 3rd day, the RMS becomes stable to the 12th day. When the RMS reaches the noise range for the first time from the analogous date, it may be no longer considered as the analog pair. For the analogy in weather prediction, it may be the criterion that the predictability is lost. For this reason, the limit of predictability P is defined as the time taken for the RMS to reach the noise range. In this case, P for the best analog pair is about 3 days.

Similar to the above result, the limit of the predictability P for the all independent analog pairs are calculated. Figure 2.6 shows a scatter diagram of P as a function of the initial RMS difference E_0. The distribution of P is widely spread regardless of E_0. The solid curve is the best fit of the regression using Eq. (2.5), and the regression yields:

$$P = -2.88 \log \left(\frac{E_0}{E_\infty - E_0} \right) + 5.7. \tag{2.6}$$

In spite of the spread distribution of P, a standard error of the coefficient of the first term is 0.03 because the total number of the independent analog pair is 21530. This equation means that the limit of predictability P extends 2.88 days when the initial RMS difference E_0 reduced to $1/e$ for sufficiently small E_0.

Table 2.1: The list of the best ten independent analog pairs and their RMS difference.

	Dates of the pair	RMS (m)
1	06Z 28, Jan. 1956 - 06Z 13, Feb. 1961	59.23
2	12Z 4, Dec. 1964 - 18Z 12, Dec. 1974	59.40
3	18Z 31, Jan. 1955 - 18Z 12, Feb. 1974	59.80
4	00Z 7, Jan. 1964 - 12Z 2, Jan. 1989	60.53
5	00Z 19, Dec. 1952 - 06Z 7, Jan. 1961	60.87
6	00Z 26, Dec. 1956 - 00Z 18, Jan. 1991	61.29
7	06Z 25, Jan. 1957 - 18Z 3, Dec. 1972	61.75
8	00Z 23, Dec. 1952 - 18Z 7, Dec. 1974	61.97
9	18Z 25, Dec. 1950 - 12Z 24, Dec. 1976	62.32
10	18Z 6, Dec. 1949 - 00Z 19, Dec. 1974	62.48
	average of RMS difference of all pairs =	121.8
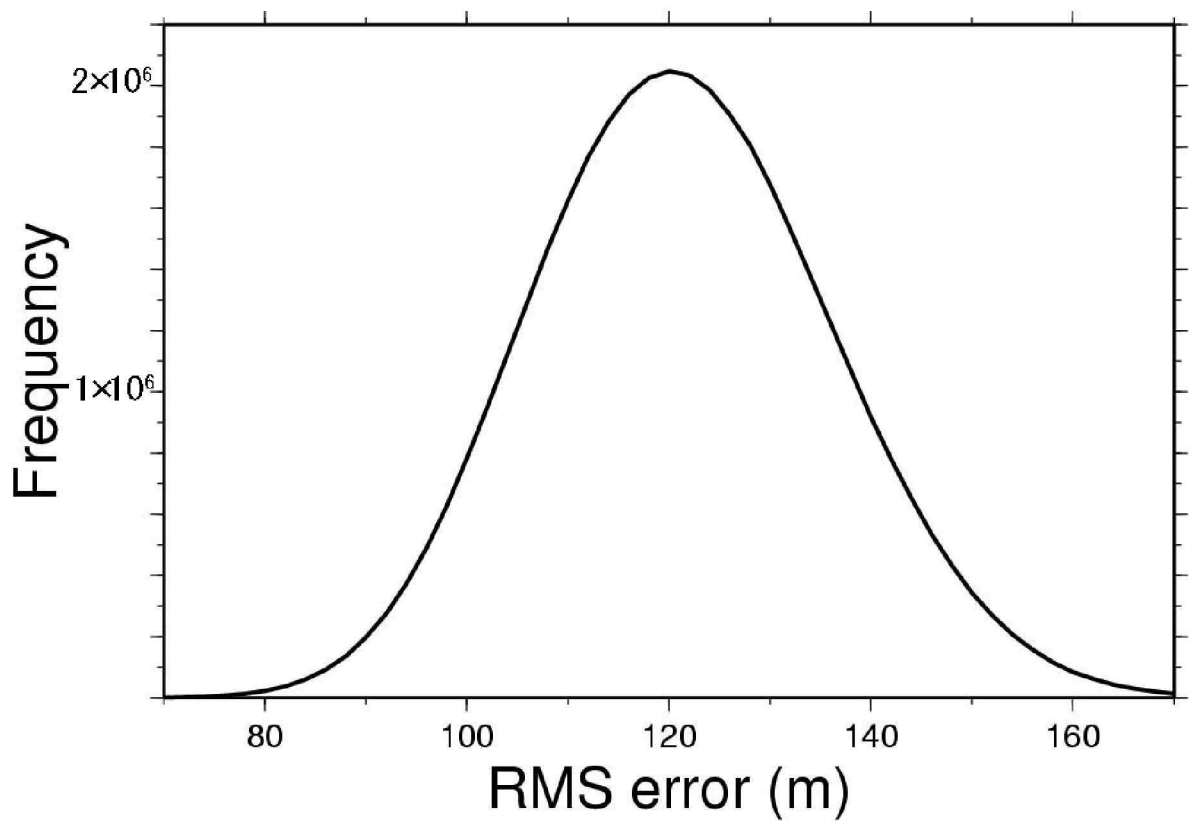
Figure 2.1: Frequency distribution of RMS difference resulted from all combinations of weather maps.

Geopotential Height
Mean
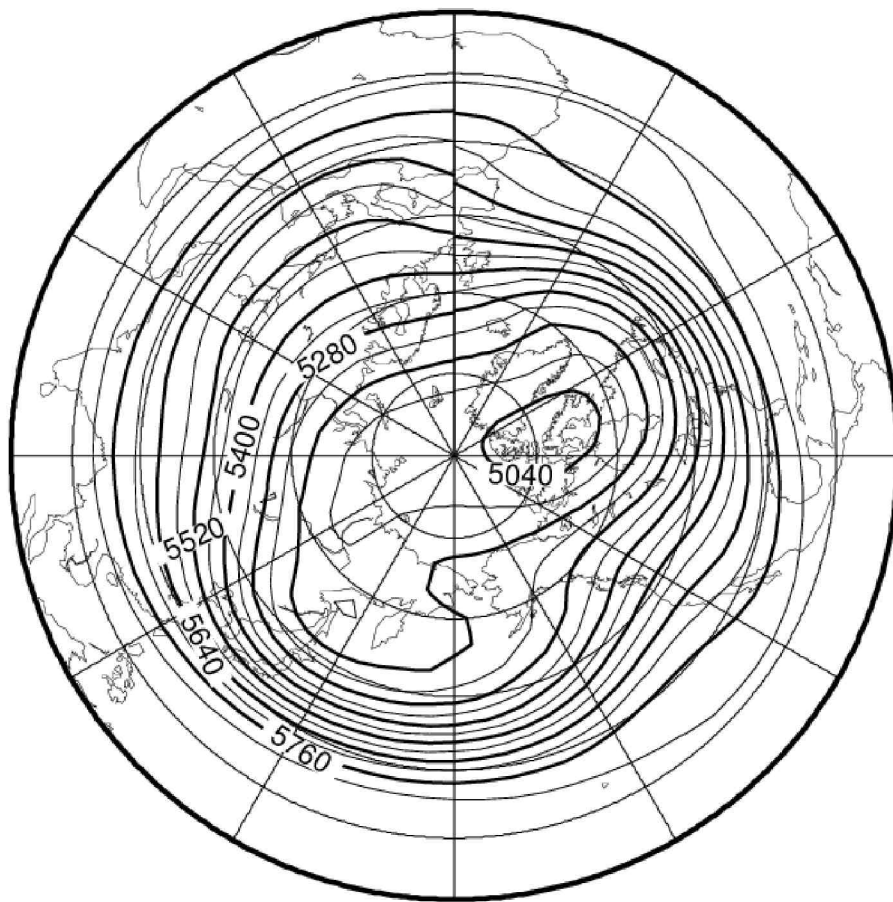
Figure 2.2: Map of the mean geopotential height at 500 hPa for the top 100 of the independent analog pairs. The contour interval is 60 m.
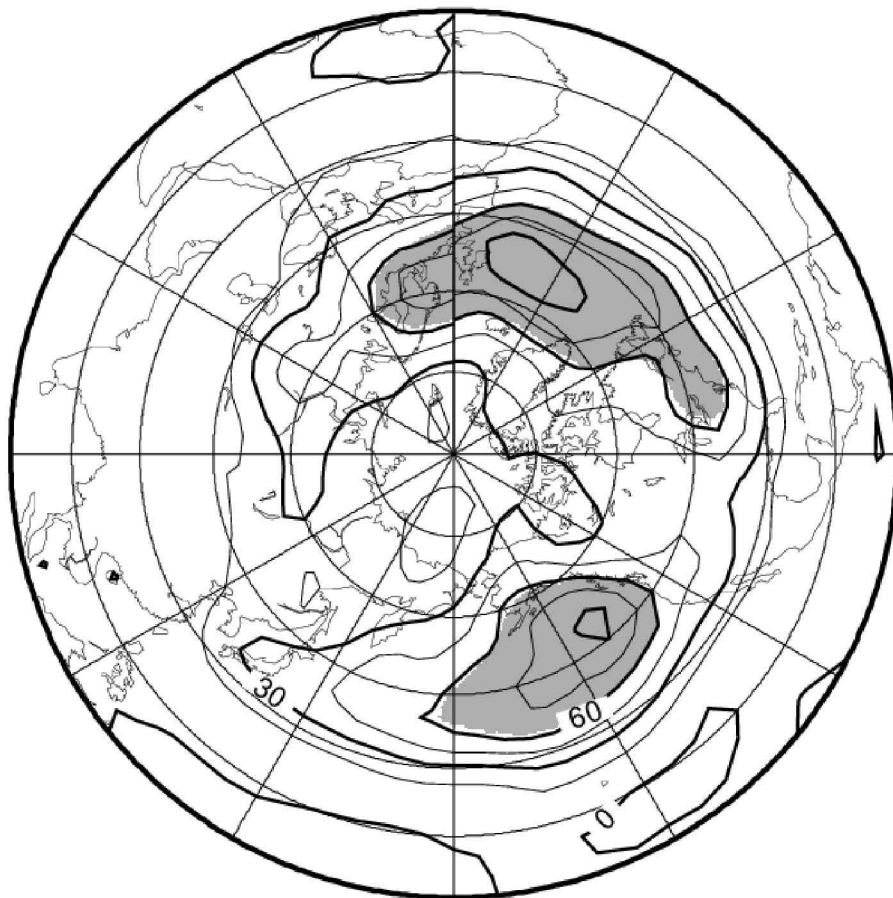
Figure 2.3: Map of the distribution of the grown difference for the top 1000 of the independent analog pairs for 3 days from the most analogous date. The contour interval is 15 m, and the RMS difference above 60 m are shaded.
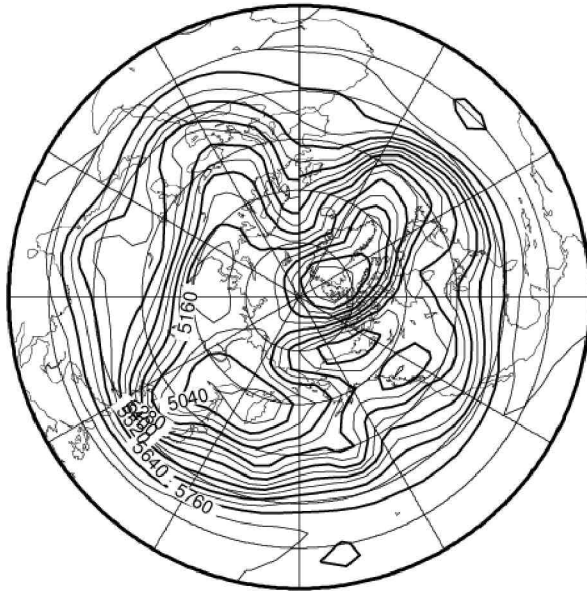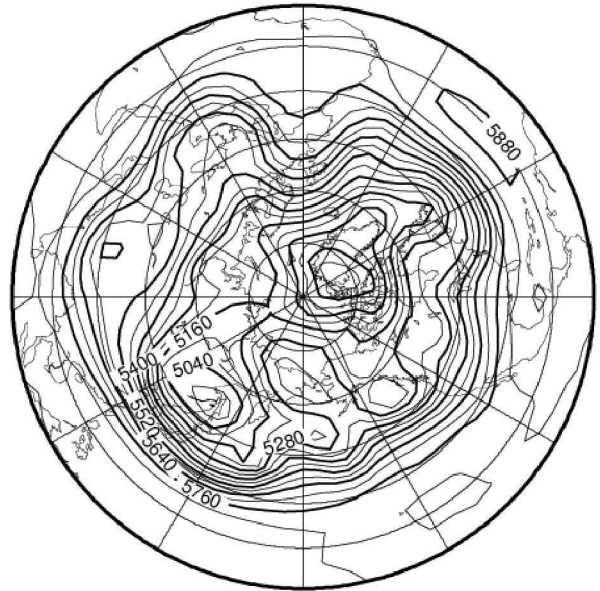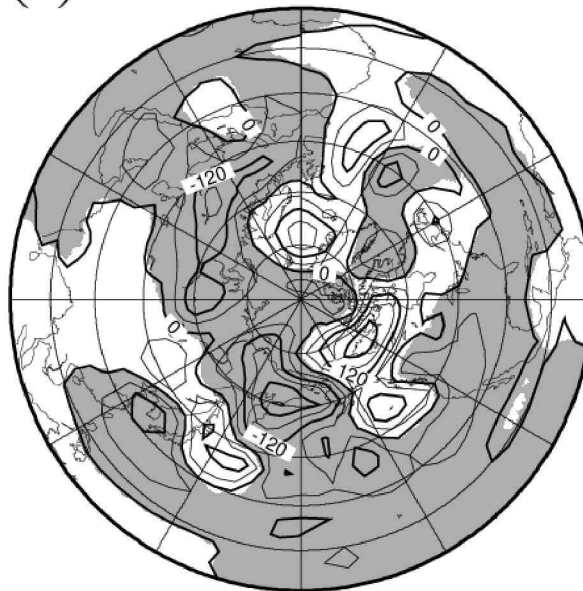
Figure 2.4: Maps of the 500hPa geopotential height. Shown are the best analog pair for (a) 0600Z 28, January 1956, (b) 0600Z 13, February 1961, (c) the difference between (a) and (b) with negative contours shaded. The contour interval is 60 m.
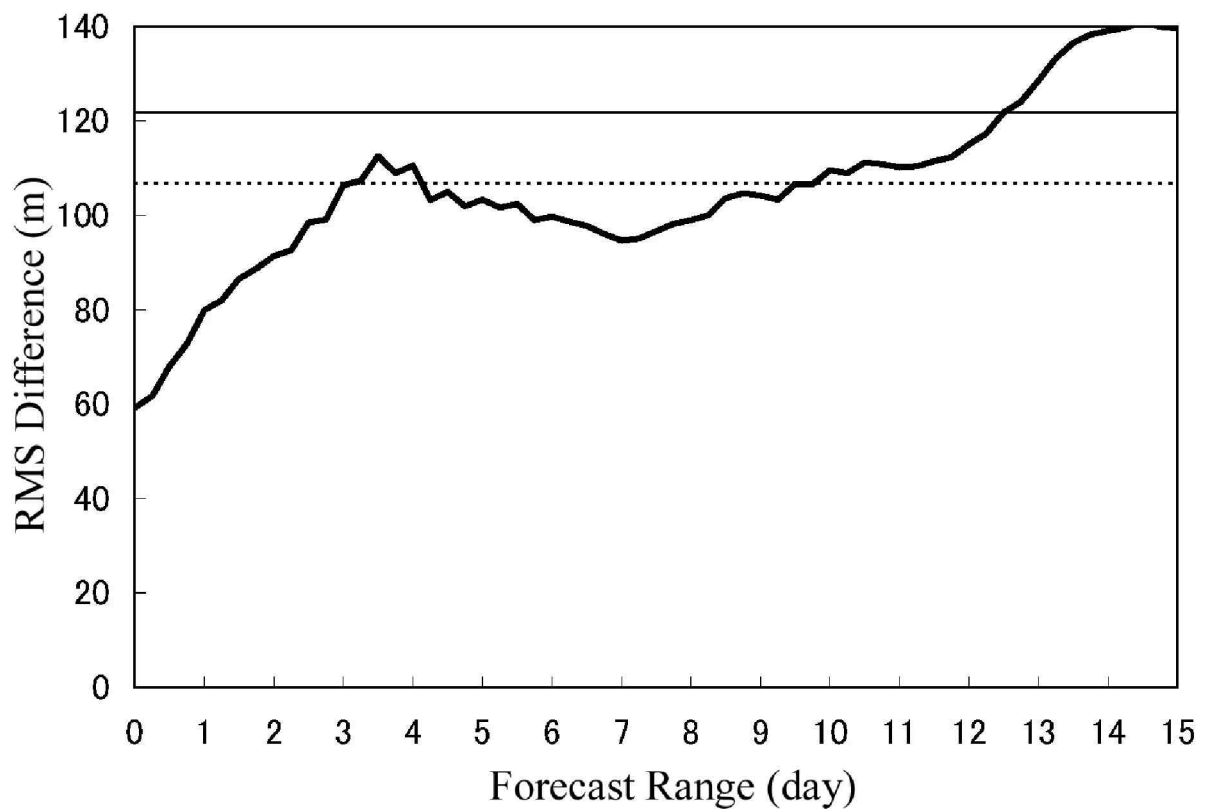
Figure 2.5: Time variation of the RMS difference. The solid curve represents the RMS error for the best analog pair. The solid and dashed straight lines represent the climatological mean (121.8 m) and the one standard deviation of fluctuation from the mean (106.8 m), respectively.
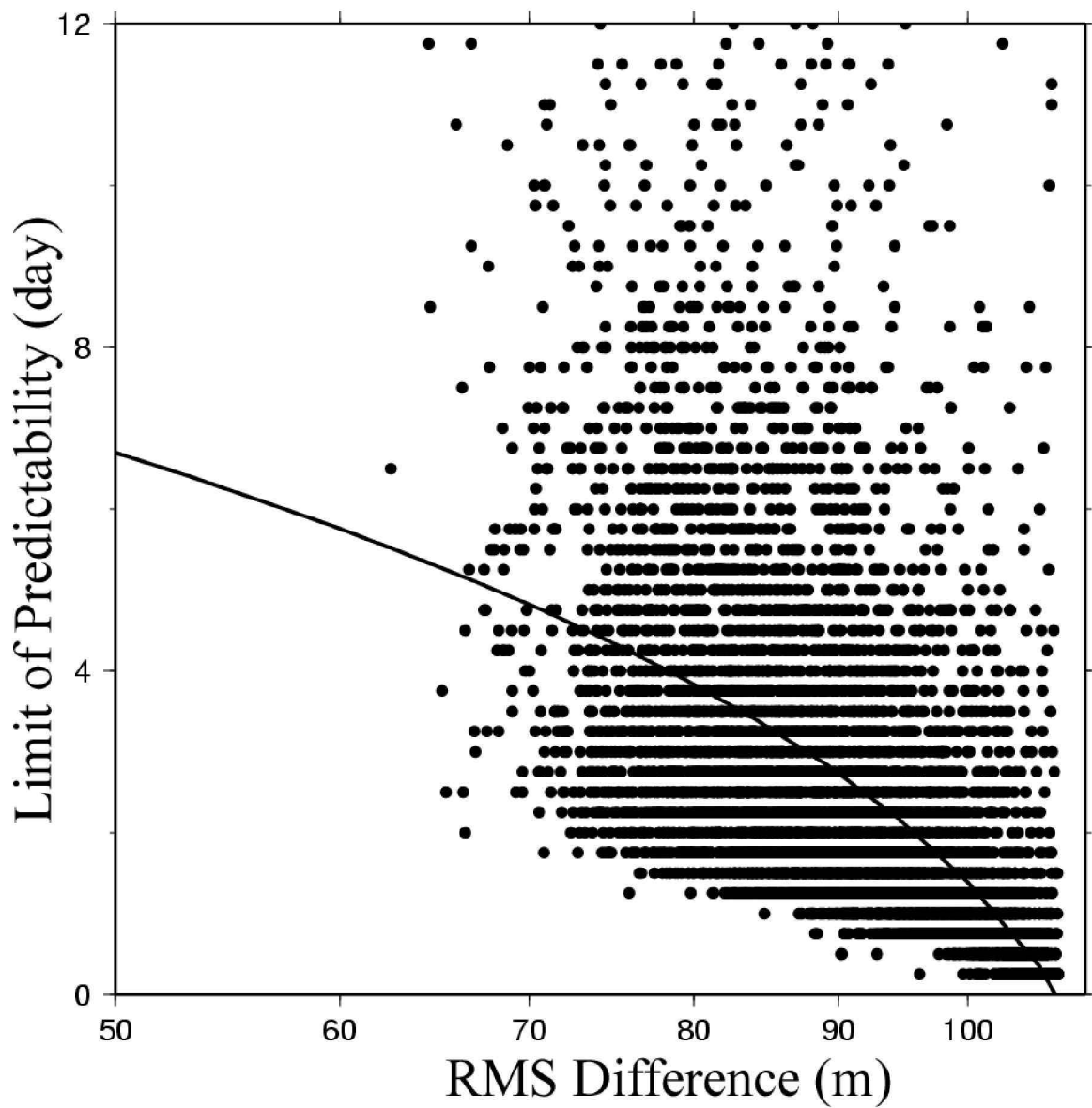
Figure 2.6: Scatter diagram of E_0 against P. The solid curve is the best fit of the regression using Eq. (2.5).

2.2.2 Role of Boundary and basic flow pattern for Atmospheric Predictability

Generally, the seasonal forecast skill is higher during El Niño winter than normal winter (Chen and van den Dool 1997; Barsugli et al. 1999; Shukla et al. 2000). In the El Niño condition, the high SST region, which normally locates in the western tropical Pacific, shifts to the central tropical Pacific. Then, the circulation pattern over the tropic is changed by the strong external forcing due to the El Niño. Certainly, the strong external forcings as El Niño and La Niña significantly impact upon the planetary scale circulation over the extratropics (e.g., Lau and Nath 1994), and derive the major atmospheric inherent mode, such as Pacific-North American (PNA) pattern. Additionally, the North Atlantic Oscillation (NAO) is as inherent as the major atmospheric PNA pattern. Since the synoptic scale cyclone activity over the extratropics directly attributes to the initial error growth for the operational forecasting, it is expected that the external forcings and particular atmospheric flow pattern indirectly impact on the initial error growth. In this section, this study will show the atmospheric predictability by the difference of the boundary conditions, such as El Niño and La Niña, and the atmospheric flow pattern such as PNA and NAO.

Case of El Niño and La Niña

Similar to Section 2.2.1 of the atmospheric predictability, the analog pairs are searched by the partitioned datasets into El Niño, La Niña, and neutral years based on an SST index, defined as DJF mean of averaged SST over the Niño-3.4 region (5.0°N-5.0°S, 170°-120°W). The SST index is then ranked, and the winters (DJF) with highest 15, lowest 15, middle 15 ranks are classified as El Niño, La Niña, and neutral years, respectively. Table

2.2 shows the Northern Hemisphere winters classified as El Niño, La Niña, and neutral years.

First, the RMS difference for all combinations of all weather maps are calculated in each classified years. Figure 2.7 shows normalized frequency distributions of the RMS difference during El Niño year, La Niña year, neutral year, and the average that is all combination for 53 winters irrespective of El Niño or La Niña. The frequency distributions in El Niño year is shifted to smaller RMS difference than the other distributions. It is indicated that the atmospheric variability in El Niño year is smaller than the other years.

Next, the limit of the predictability P for the all independent analog pairs are calculated to estimate the atmospheric predictability in each classified year. The climatological noise range adopts the 106.8 m RMS difference that is same as Section 2.2.1. The scatter-diagram for the initial difference E_0 and P is fitted by the quadratic error growth model of Eq. (2.5). Then, the coefficient of the first term in Eq. (2.5) indicates the difference growth rate of the analog pair. Figure 2.8 shows the difference growth rates (e-folding time) for averages for El Niño year, La Niña year, and neutral year. The horizontal bars indicate the standard error for each condition. The e-folding time in the case of El Niño year is 2.84 days that is equivalent to the all combination case. The cases of La Niña and neutral year indicate faster difference growing speed than the average case, and their e-folding times are 2.72 and 2.77 days, respectively.

Case of PNA Pattern

Similar to Section 2.2.1 of the atmospheric predictability, the analog pairs are searched by the partitioned datasets into positive PNA (PNA+), negative PNA (PNA-), and neutral

years based on an PNA index, defined by Wallace and Gutzler (1981) as:

$$PNA = \frac{1}{4}[Z(20°N, 160°W) - Z(45°N, 165°W) + Z(55°N, 115°W) - Z(30°N, 85°W)],$$
(2.7)

where Z are standardized 500 hPa geopotential height values. The PNA index is then ranked, and winters (DJF) with highest 15, lowest 15, middle 15 ranks are classified as PNA+, PNA-, and neutral years, respectively. Table 2.3 shows Northern Hemisphere winters classified as PNA+, PNA-, and neutral years.

Similar to El Niño and La Niña cases, the RMS for all combinations of all weather maps are calculated in each classified year. Figure 2.9 shows the normalized frequency distributions of the RMS difference during PNA+ year, PNA- year, neutral year, and the average. The frequency distributions in PNA+ year is apparently shifted to smaller RMS difference than the other distributions, while PNA- case is slightly shifted to the large RMS difference than the other distributions.

Next, the limit of the predictability P for the all independent analog pairs are calculated to estimate the atmospheric predictability in each classified year. Figure 2.10 shows the difference growth rate (e-folding time) for the average, PNA+ year, PNA- year, and neutral year. The horizontal bars indicate the standard error for each condition. The e-folding time in the case of PNA+, PNA-, and neutral year are 3.17, 2.69, and 2.84 day, respectively. The difference growth rate is clearly separated by the each condition, and PNA+ year indicates the slowest difference growing speed, while PNA- year is the fastest. The neutral year is equivalent to the average case.

Case of NAO Pattern

Similar to Section 2.2.1 of the atmospheric predictability, the analog pairs are searched by the partitioned datasets into NAO+, NAO-, and neutral years based on an NAO index, defined as the difference of normalized sea level pressures (SLP) between Ponta Delgada in Azores islands (37.8°N, 25.7°W) and Stykkisholmur/Reykjavik (65.1°N, 22.7°W) in Iceland by Hurrel (1995). The NAO index is then ranked, and winters with highest 15, lowest 15, middle 15 ranks are classified as positive NAO (NAO+), negative NAO (NAO-), and neutral years, respectively. Table 2.4 shows the Northern Hemisphere winters classified as NAO+, NAO-, and neutral years.

Similar to El Niño and La Niña cases, the RMS for all combinations of all weather maps are calculated in each classified year. Figure 2.11 shows normalized frequency distributions of the RMS difference during NAO+ year, NAO- year, neutral year, and the average. The frequency distributions during NAO+ year is slightly shifted to smaller RMS difference than the other distributions, while NAO- case is shifted to large RMS difference than the other distributions.

Next, the limit of the predictability P for the all independent analog pairs are calculated to estimate the atmospheric predictability in each classified years. Figure 2.12 shows the difference growth rate (e-folding time) for all combinations of NAO+ year, NAO- year, and neutral year. The horizontal bars indicate the standard error for each condition. The e-folding time in the case of NAO+, NAO-, and neutral year are 3.07, 2.99, and 2.87 day, respectively. The cases of NAO+ and NAO- indicate slower difference growing speed than the average case. The neutral year is equivalent to the average case.

Comparison of Difference Growth Rates

Table 2.5 lists the difference growth rates (e-folding time) for the various boundary conditions. With the consideration of the standard error, it is found that the atmospheric feature during PNA+ and NAO+ year apparently have slower difference growth than the average case. On the contrary, the atmospheric feature during La Niña and PNA- have faster difference growth than the average case.

Table 2.2: The list of the Northern Hemisphere winters (DJF) classified as El Niño, La Niña, and neutral years. The year in the table refers to January of the event listed.

SST anomalies over Niño 3.4 region					
El Niño		Neutral		La Niña	
1983	2.68	1991	0.39	1989	-1.83
1998	2.51	1954	0.26	1974	-1.77
1992	1.91	1993	0.24	2000	-1.65
1973	1.72	1953	0.14	1971	-1.59
1958	1.69	1982	0.11	1976	-1.53
1966	1.38	1994	0.09	1999	-1.53
1987	1.32	1990	0.07	1985	-1.19
1995	1.07	1979	0.02	1956	-1.04
1969	1.03	2002	-0.02	1955	-0.92
1964	0.82	1957	-0.15	1996	-0.84
1988	0.82	1960	-0.15	2001	-0.74
1970	0.81	1981	-0.17	1984	-0.69
1977	0.64	1961	-0.18	1965	-0.69
1978	0.59	1962	-0.29	1951	-0.68
1959	0.57	1967	-0.31	1968	-0.64

Table 2.3: The list of the Northern Hemisphere winters classified as PNA+, PNA-, and neutral years. The 15 years with the highest PNA indexes are selected as PNA positive (PNA+). Similarly, The 15 years with the lowest PNA indexes are selected as PNA negative (PNA-). The neutral year indicates the 15 years with the nearest climatology.

PNA Index					
Positive		Neutral		Negative	
1998	1.95	1984	0.48	1972	-2.27
1977	1.72	1996	0.44	1950	-1.86
1983	1.68	1973	0.23	1949	-1.66
1958	1.43	2000	0.11	1957	-1.25
1981	1.43	2002	0.07	1965	-1.24
1970	1.41	1954	0.01	1969	-1.15
1986	1.28	1967	-0.04	1971	-1.08
1978	1.24	1994	-0.05	1956	-1.06
1964	1.20	1951	-0.12	1979	-1.05
1987	1.13	1997	-0.12	1989	-1.00
1961	1.12	1959	-0.25	1982	-0.81
1995	1.09	1999	-0.26	1952	-0.80
1953	0.98	1968	-0.33	1985	-0.68
1963	0.87	1991	-0.43	1976	-0.65
2001	0.71	1955	-0.49	1974	-0.64

Table 2.4: Same as Table 2.3, but for NAO index.

NAO Index					
Positive		Neutral		Negative	
1989	2.59	1950	0.37	1969	-2.43
1993	1.99	1954	0.33	1979	-2.04
2000	1.93	1997	0.25	1966	-2.01
1992	1.83	1994	0.21	1977	-1.74
1983	1.50	1962	0.10	1960	-1.69
1949	1.46	1972	0.02	1963	-1.61
1995	1.41	1967	0.01	1996	-1.35
1990	1.39	1980	-0.12	1956	-1.28
1976	1.30	1959	-0.13	1970	-1.13
1973	1.25	1998	-0.17	1978	-1.10
1975	1.14	1988	-0.22	1955	-0.98
1999	1.14	1953	-0.23	1985	-0.97
1984	1.10	2003	-0.27	1986	-0.96
1981	1.07	1971	-0.43	1982	-0.83
1991	1.05	1987	-0.44	2001	-0.66

Table 2.5: List of the difference growth rates (e-folding time) for the various boundary conditions and atmospheric flow patterns.

		e-folding time (day)	standard error
Average		2.88	0.03
Tropical SST	El Niño	2.84	0.08
	La Niña	2.72	0.09
	Neutral	2.77	0.09
PNA	Positive	3.17	0.10
	Negative	2.69	0.07
	Neutral	2.84	0.09
NAO	Positive	3.07	0.09
	Negative	2.99	0.09
	Neutral	2.87	0.09

Frequency Distribution of RMS Difference
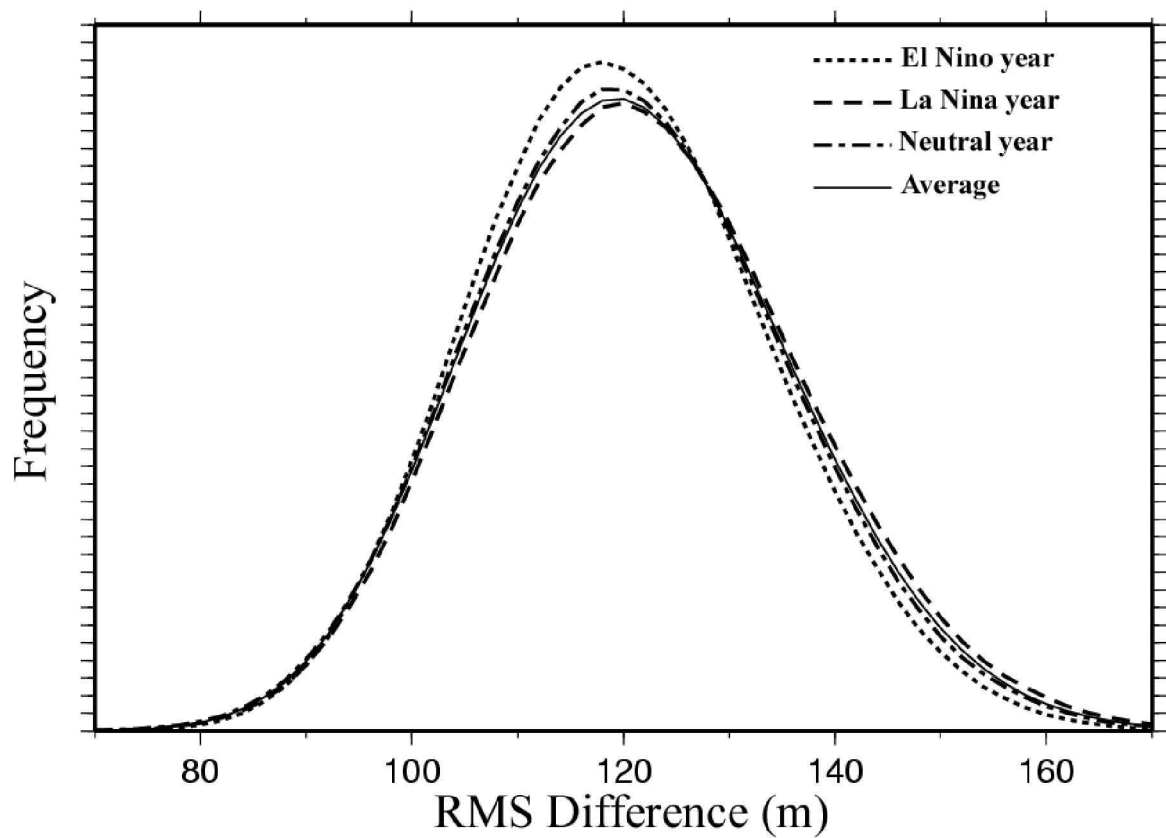
Figure 2.7: Normalized frequency distribution of the RMS difference during El Niño year (dotted line), La Niña year (broken line), neutral year (chain dashed line), and average (solid line).
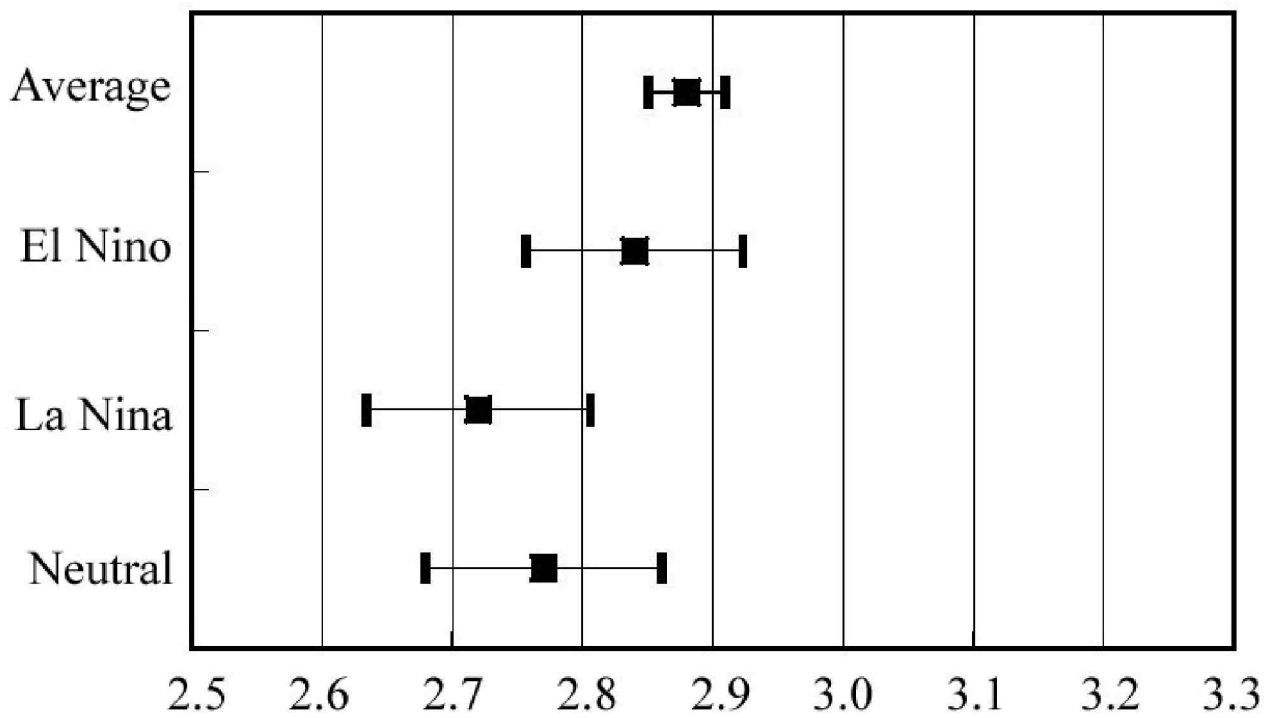
Figure 2.8: Difference growth rate (e-folding time) for average, El Niño year, La Niña year, and neutral year. The horizontal bars indicate the standard error for each condition.

Frequency Distribution of RMS Difference
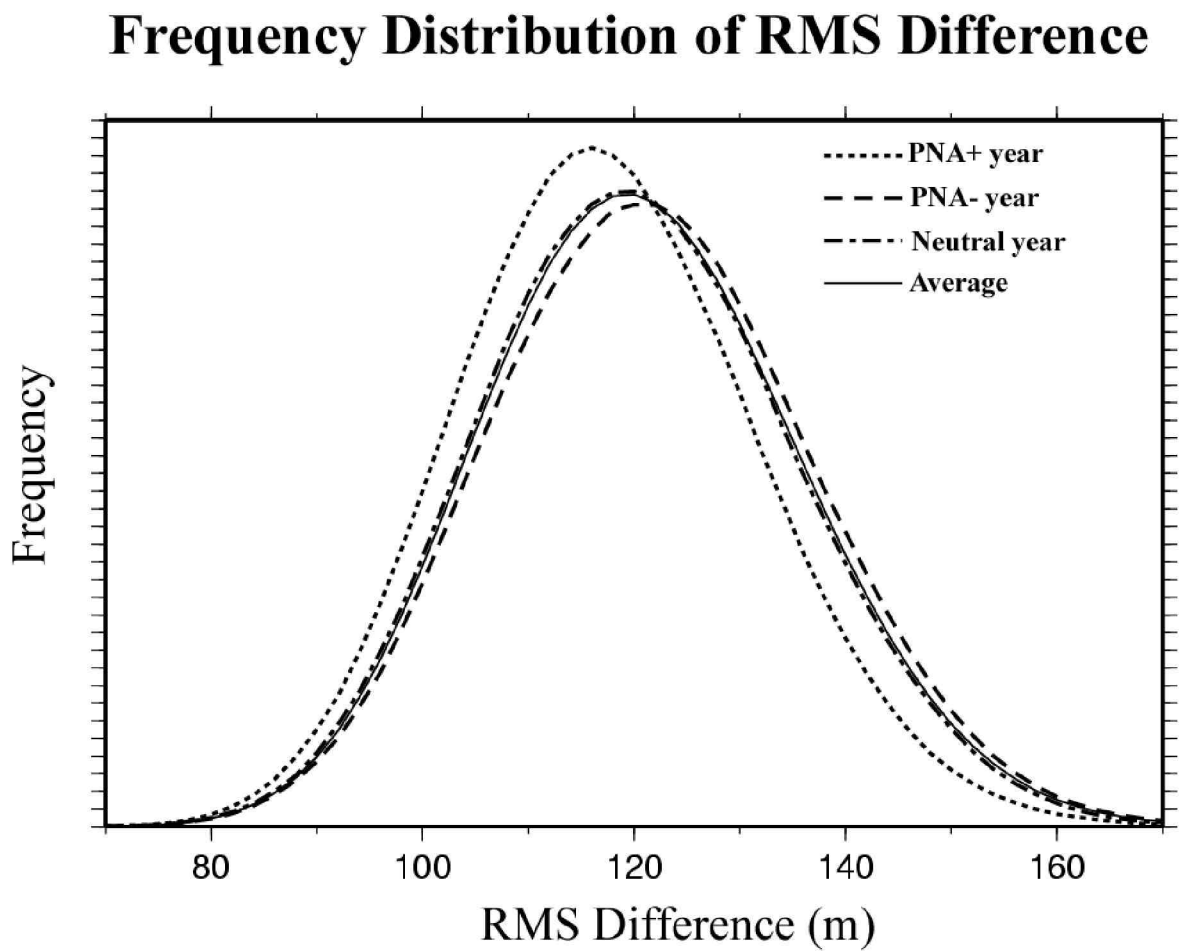
Figure 2.9: Same as Fig. 2.7, but for PNA pattern.
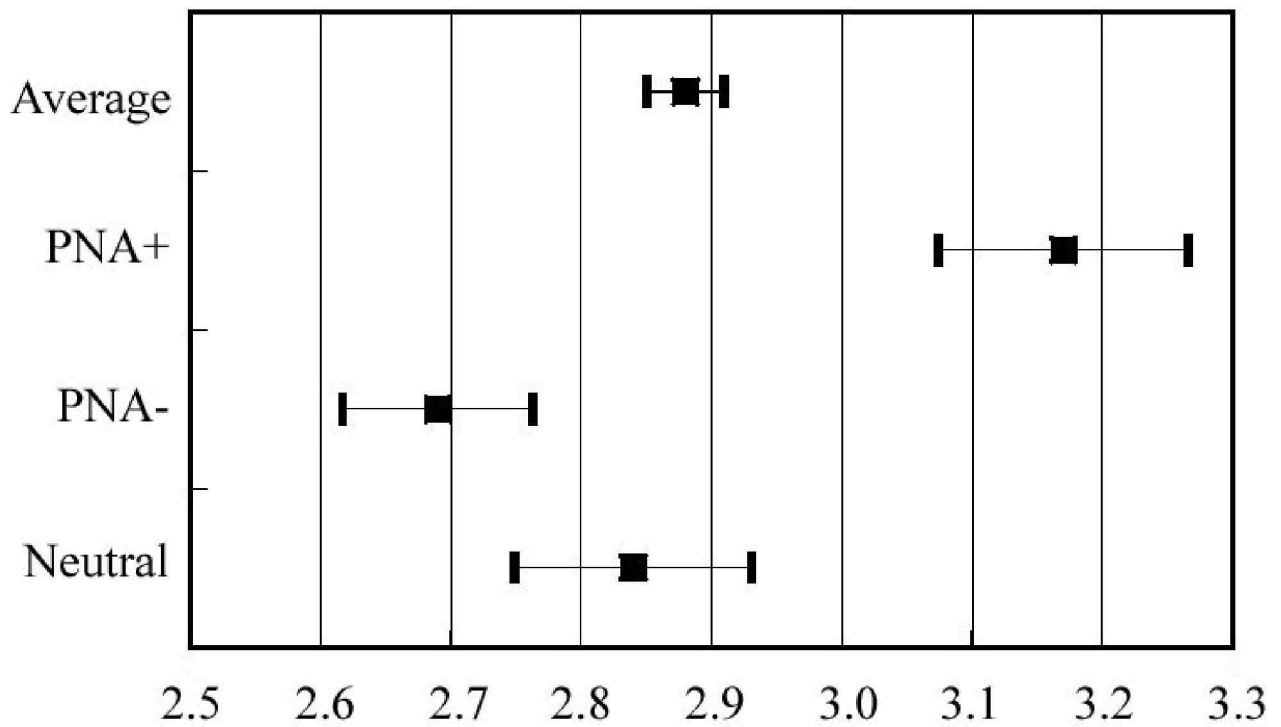
Figure 2.10: Same as Fig. 2.8, but for PNA.
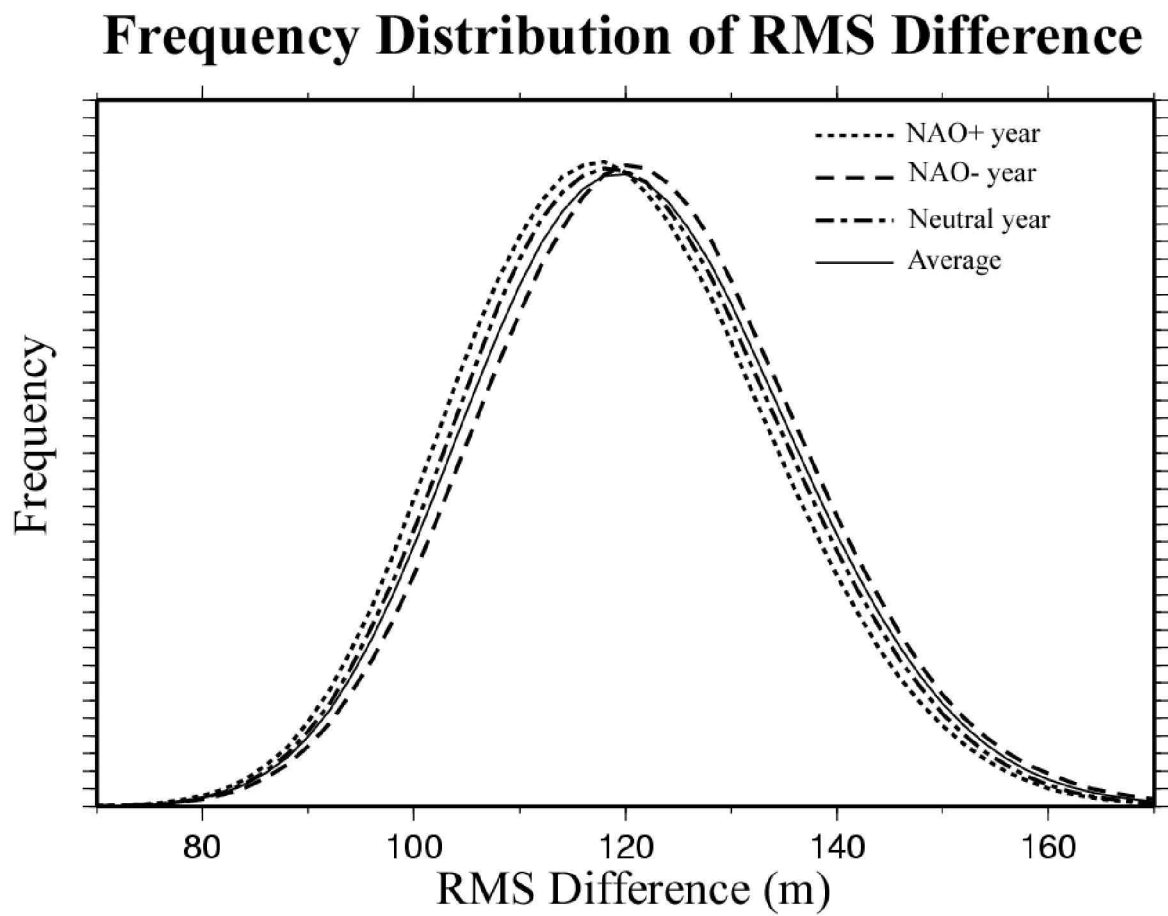
Figure 2.11: Same as Fig. 2.7, but for NAO.
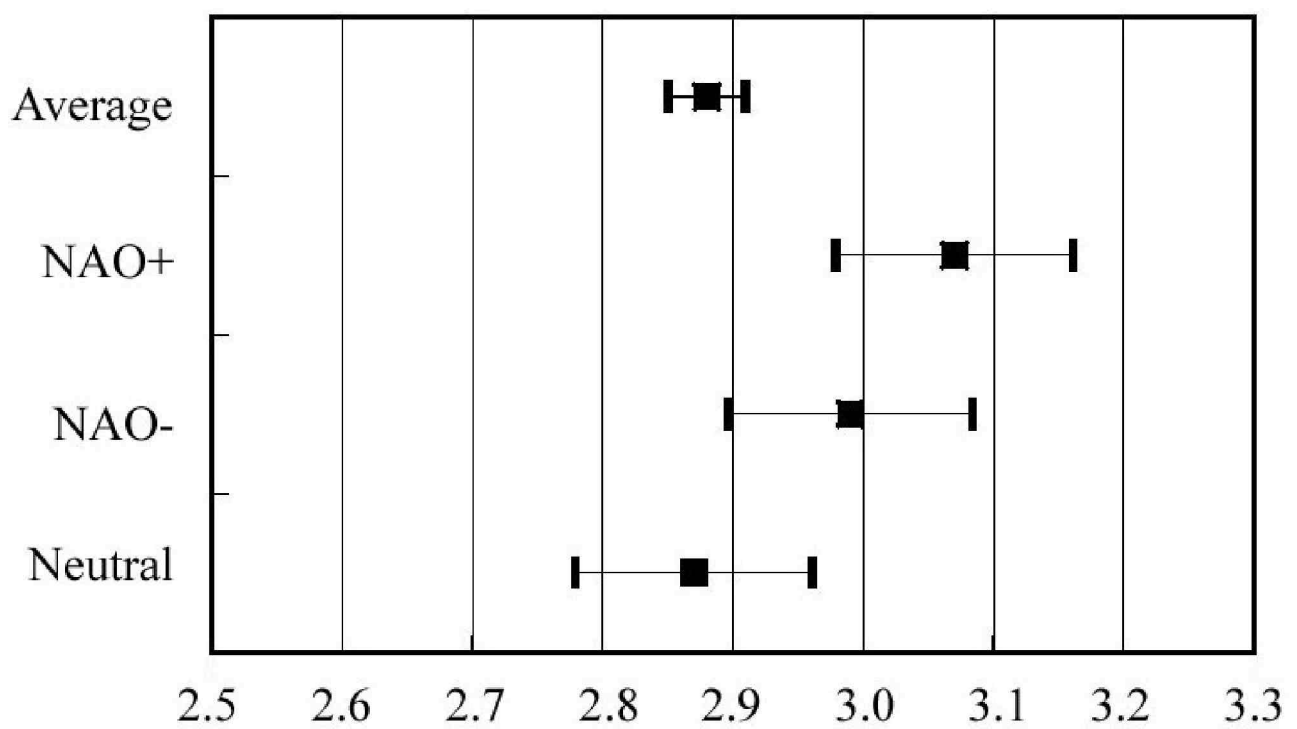
Figure 2.12: Same as Fig. 2.8, but for NAO.

2.2.3   Hindcast Experiments

In this section, the role of the boundary and basic flow pattern for the atmospheric predictability is verified by the hindcast dataset. The hindcast dataset contains the daily 15 days forecasts on 500 hPa for 23 winters from December 1979 to February 2002. Figure 2.13 shows scatter diagram of the DJF mean of the RMS error on 7 days hindcast and the SST, PNA, and NAO indices. The correlation coefficients associated with the SST, PNA, and NAO are -0.16, -0.50, and -0.30, respectively. The 95% significant level for the correlation is -0.41. The clear inverse correlation is shown in the cast of the PNA years. It is indicated that the PNA+ years tend to derive better forecast skill than PNA- years. On the other hand, the inverse correlations associated with the SST and the NAO indices are indistinctly shown in Fig. 2.13. These results are similar to the estimated predictability by the analog pairs.

Figure 2.14 shows the time series of the correlations between the RMS error of the hindcast and the SST, PNA, and NAO indices. The thin straight lines indicate 95% significant levels for the correlations. Until the 3-days hindcast, the RMS error for all hindcasts are independent of SST, PNA, and NAO indices. After the 3-days hindcast, the RMS error for the hindcast indicates clear inverse correlation with the PNA index in particular. The relation between the RMS error and the PNA index is reinforced as time proceeds.

Figure 2.15 illustrates the distribution of the mean RMS error for 7 days hindcast at 500 hPa geopotential height during the El Niño and the La Niña years. Then, the El Niño and the La Niña years are defined as the highest 7 years and the lowest 7 years of the SST index for 23 winters from December 1979 to February 2002. Although the hindcast errors over the high latitude (over 120 m) are larger than the low latitude (under 40 m)

during the both of the El Niño and the La Niña years, the anomalies of the hindcast errors during the El Niño years indicate that there are regions of the small error growth over the north Pacific to the north America (-15 m). During the La Niña years, there are regions of the large error growth over the north America (5 m). Therefore, the difference between the El Niño and the La Niña years are shown over the north Pacific to the north America.

Figure 2.16 illustrates the distribution of the mean RMS error for the 7-days hindcast at 500 hPa geopotential height in the case of the PNA+ and the PNA- years. Te PNA+ and the PNA- years are defined as the highest 7 years and the lowest 7 years of the PNA index. Similarly to the El Niño and the La Niña years, the anomalies of the hindcast errors during the PNA+ years indicate that there are regions of the small error growth over the north Pacific to the north America (-10 m). During the PNA- years, there are regions of the large error growth over the Arctic to the north America (15 m). Therefore, the difference between the PNA+ and the PNA- years are clearly shown over the north Pacific to the north America.

Figure 2.17 illustrates the distribution of the mean RMS error for the 7-days hindcast at 500 hPa geopotential height in the case of the NAO+ and NAO-. The NAO+ and the NAO- are defined as the highest 7 years and the lowest 7 years of the NAO index. Dissimilarly to the El Niño and the PNA years, the anomaly of the hindcast errors indicate that during NAO+ years there are regions of the small error growth over the rim of the Arctic (-10 m) and large error growth over the Europe (10 m). During NAO- years, there are regions of small error growth over the Europe and large error growth over the Arctic (10 m). Therefore, the difference between the NAO+ and the NAO- years are clearly shown over the Europe and the Arctic.

Finally, the RMS error growth of the hindcast is compared with the growth of the theoretical RMS difference by the quadratic error growth model in the real atmosphere. The growth of the theoretical RMS difference is calculated by Eq. (2.4) with the difference growth rate in the real atmosphere, $-1/\alpha = 2.88$ days, and the initial difference, $E_0 = 7$ (m), which indicates the average analysis error by the recent operational prediction centers. Figure 2.18 shows time series of mean growth of RMS error for the 23 years sample of the hindcast and the theoretical RMS difference by quadratic error growth model in the real atmosphere. The error of the hindcast rapidly grows by contrast to the theoretical RMS difference in a short forecast time, because the numerical prediction system is imperfect to predict the real atmosphere. From this result, we can expect that the modification of the numerical prediction system may derive the improvement of the forecast skill. As one of the modifications, a forecast assimilation technique is proposed in next Chapter.
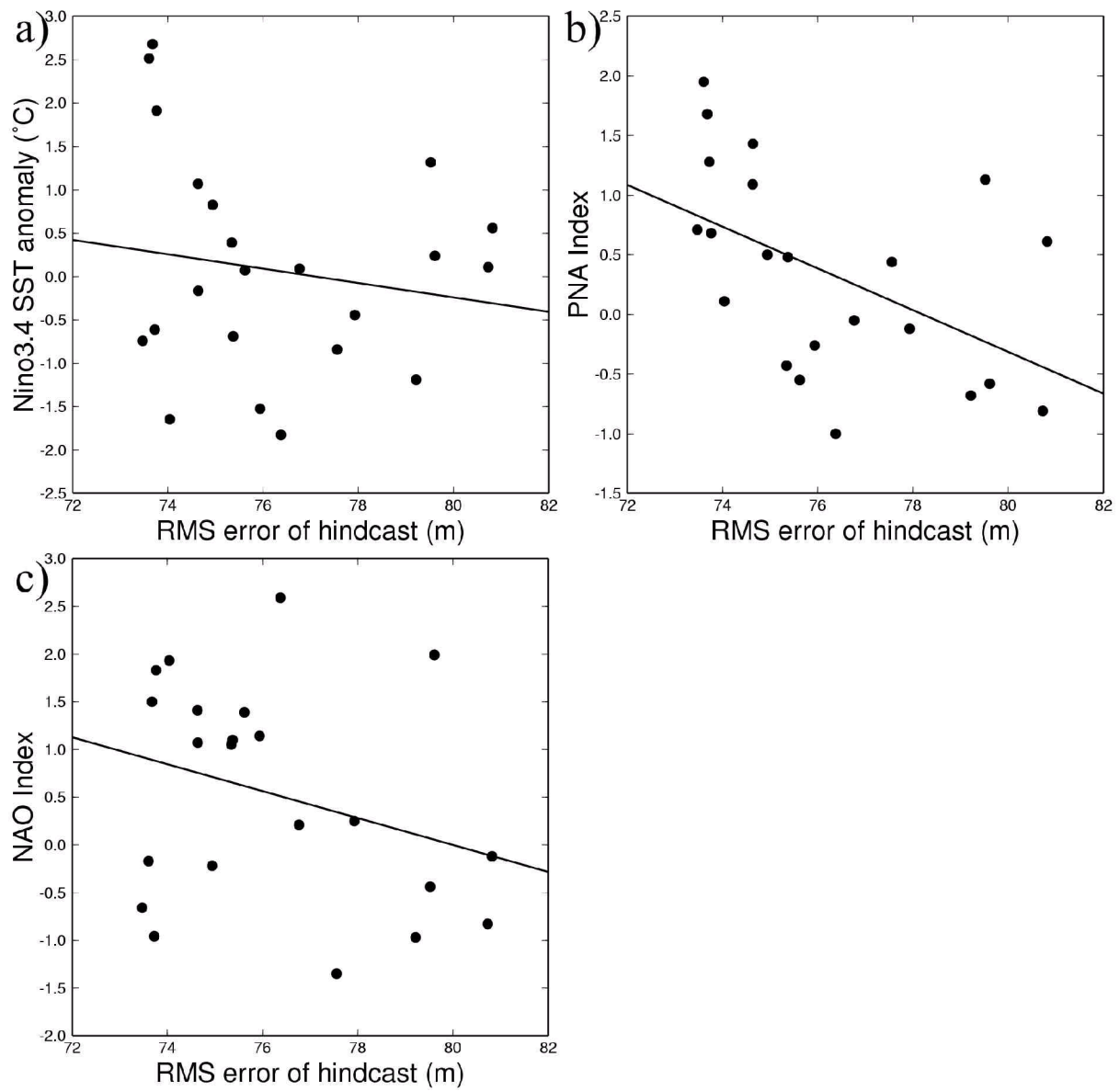
Figure 2.13: Scatter diagram of the winter (DJF) mean of the RMS error on 7-days hindcast against a) SST anomaly over Niño region, b) PNA index, and c) NAO index. The solid lines are the best fit of the linear regression.
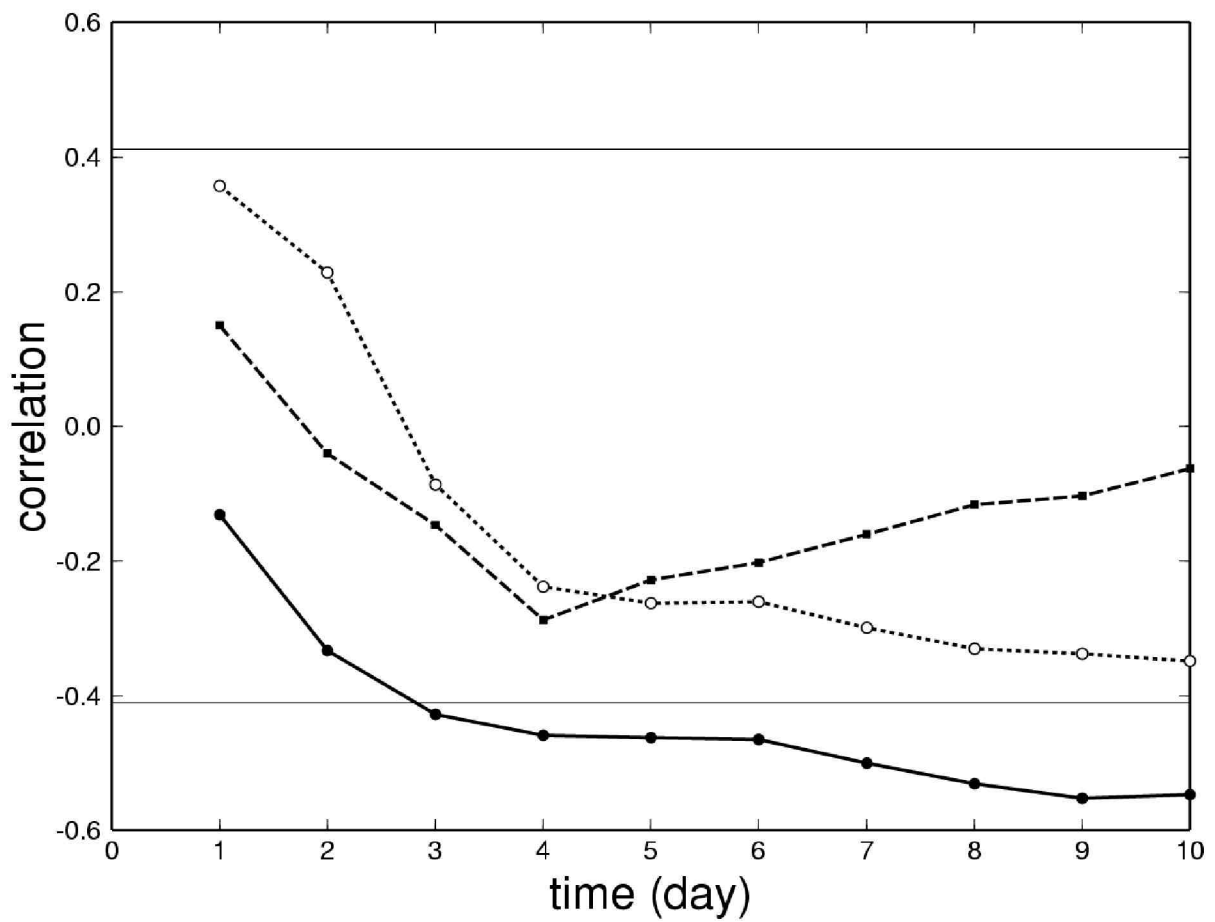
Figure 2.14: Time series of the correlation between the RMS error and each indexes for the Niño 3.4 SST anomaly (dashed line), the PNA index (solid line), and the NAO index (dotted line). The thin straight lines indicate 95% significant levels for the correlations.
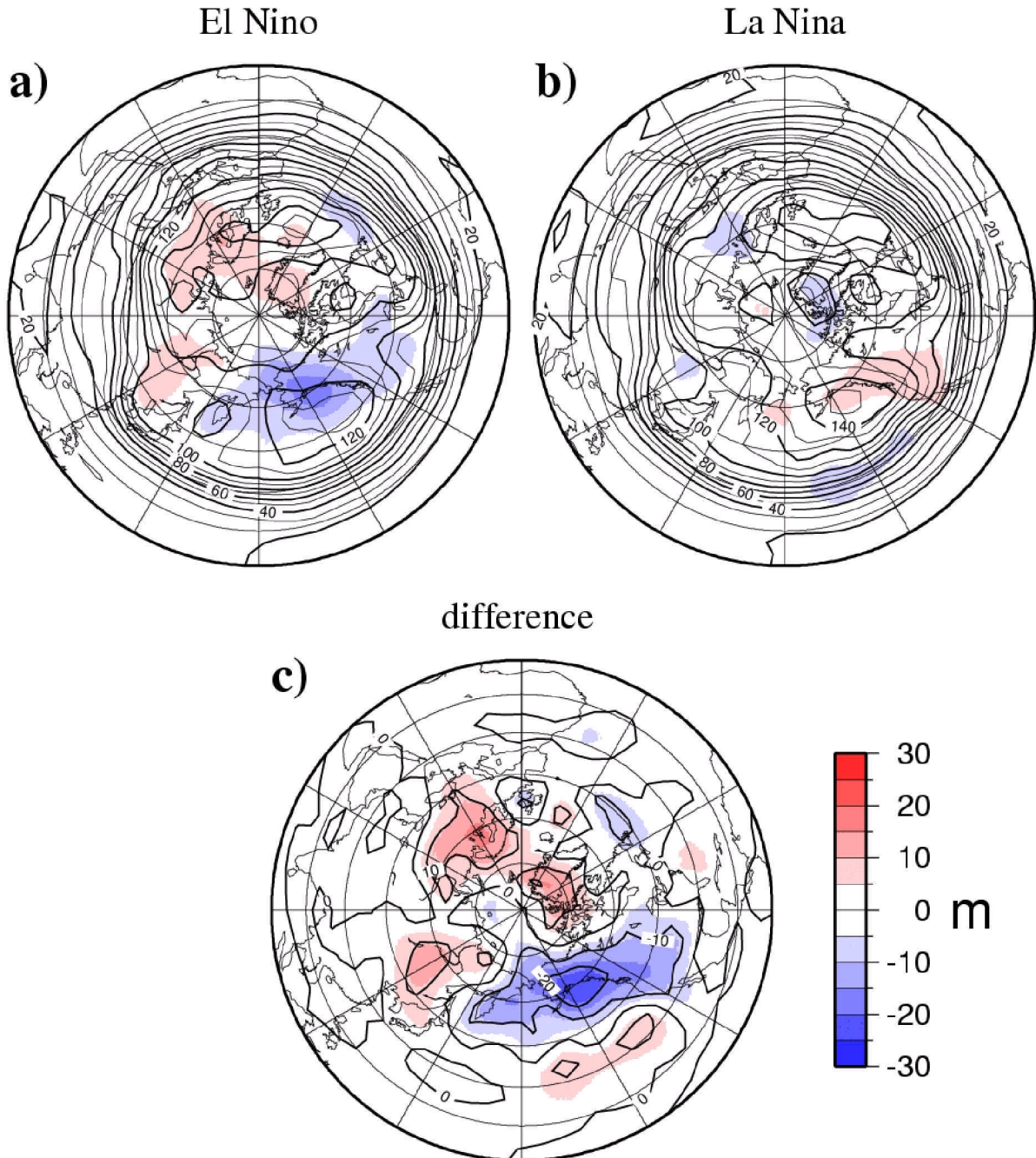
Figure 2.15: Distribution of the mean RMS error for the 7-days hindcast at 500 hPa geopotential height in the case of a) El Niño years and b) La Niña years. The contour interval is 10 m. The colored regions shows anomaly of the RMS error growth. c) shows the difference a) - b).
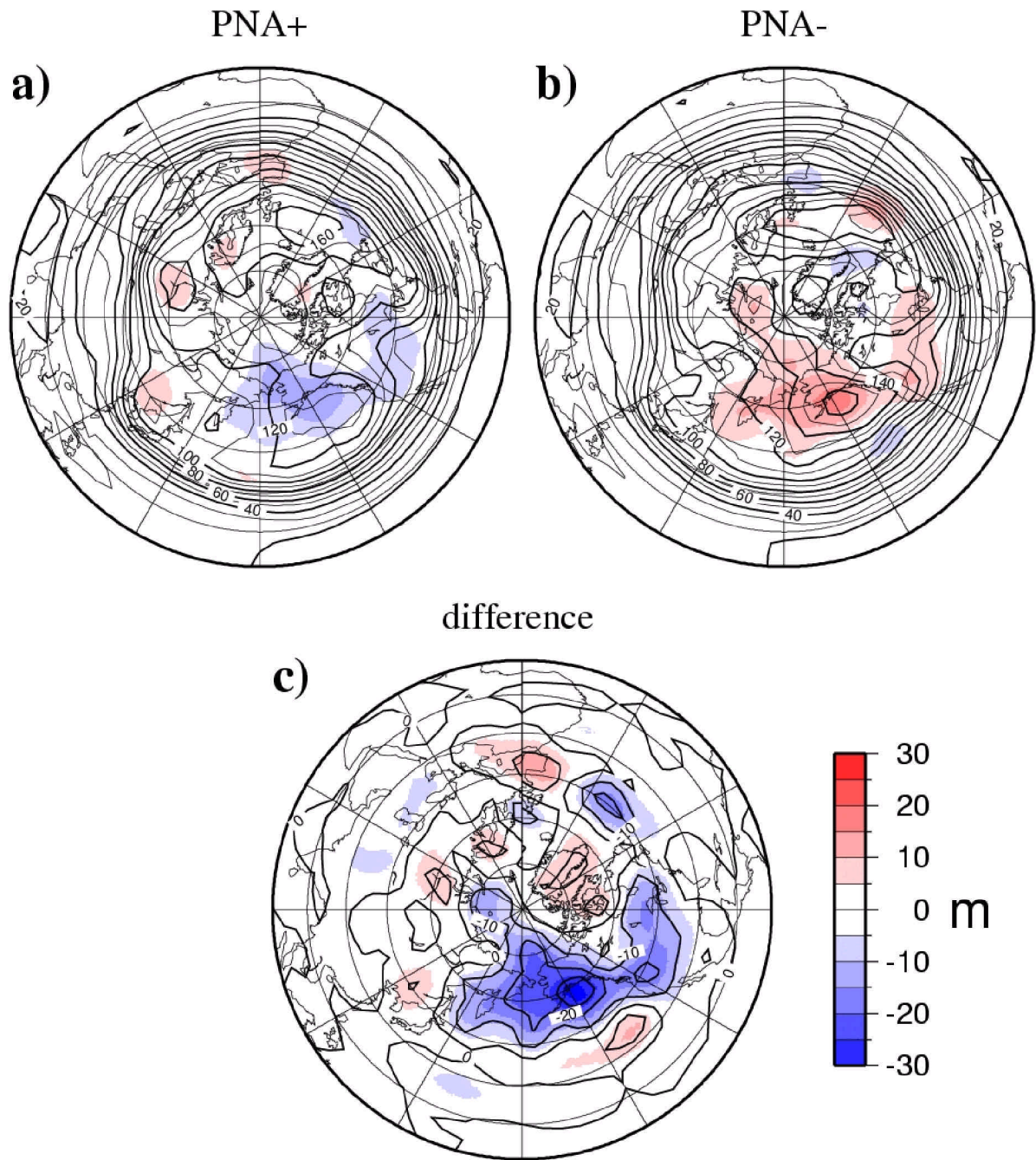
Figure 2.16: Same as Fig. 2.15, but for the PNA cases.
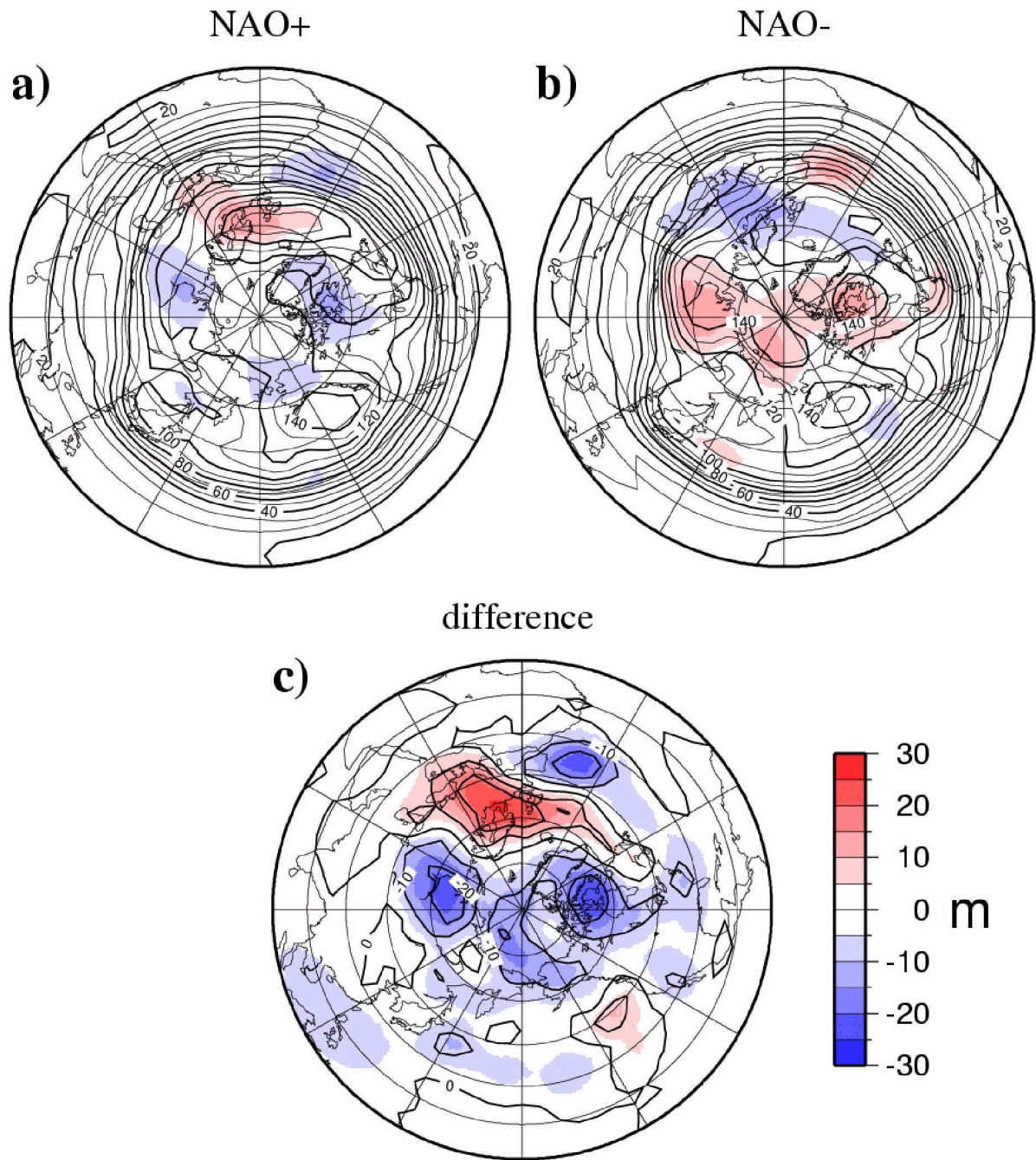
Figure 2.17: Same as Fig. 2.15, but for the NAO cases.
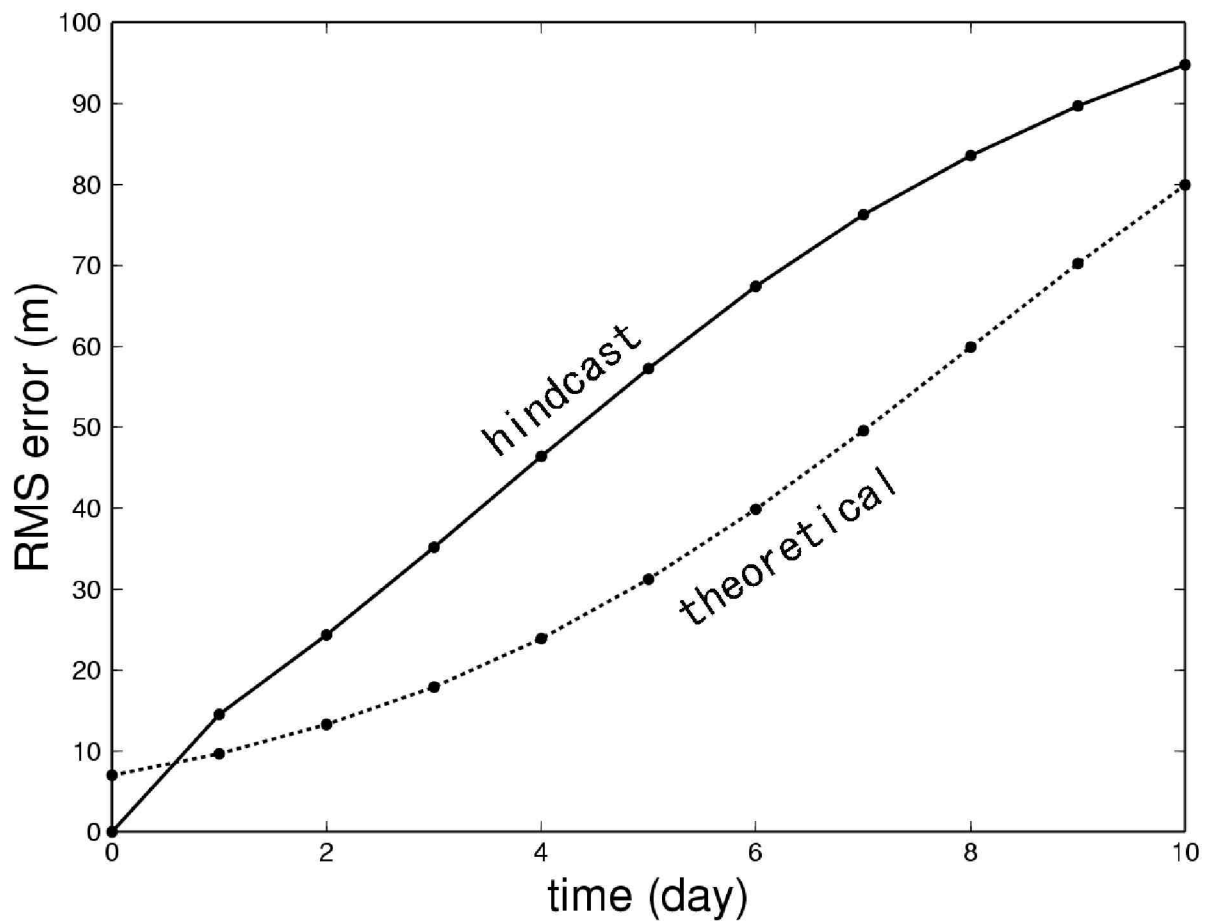
Figure 2.18: Time series of the mean growth of the RMS error for the 23 years sample of the hindcast (solid line) and the theoretical RMS difference by the quadratic error growth model for the real atmosphere (dotted line).

Chapter 3

Forecast Assimilation

3.1 Experimental design

In this section, we describe the experimental design of the forecast assimilation in detail. The forecast assimilation is a new technique for improving the weather forecast skill in the ensemble forecast system. In this study, the Lorenz model (Lorenz 1963) is used to examine the effect of the forecast assimilation. For the forecast assimilation, we use 3D-Var and the Kalman filter in this study.

3.1.1 Forecast Assimilation

In the ordinary ensemble forecast, the forecast error of the ensemble mean is generally smaller than the control forecast. Consider one ideal ensemble forecast where the initial states of the ensemble members are normally distributed around the truth. The ensemble mean is the best estimation of the truth because the mean coincides with the truth. The

distribution of the ensemble members would be stretched by an exponential error growth at the beginning of the forecast. Since the distribution is hyper cubic or elliptic, the ensemble mean is still the best forecast by the same reason. After that, the nonlinear effect becomes dominant in the nonlinear system. When the distribution is folded by the nonlinear effect, the ensemble mean is detached from the center of the distribution of the ensemble members. To avoid such the detachment, we introduce the forecast assimilation in which the true value contained in the ensemble members is accumulated into a single forecast using a data assimilation technique. Generally, the initial errors are superimposed on the control run, since the truth is unknown for the ensemble members. Nevertheless, comparing the forecast skill under the known truth may be the first step to show the usefulness of the assimilated forecast.

Figure 3.1 illustrates a schematic flowchart of the forecast assimilation technique. The bold arrows and boxes denote the stream of the forecast assimilation. First, a control forecast (denoted as CF) and some ensemble members are calculated from an initial state at t_0. Since we cannot know the true (denoted as Tr) initial state, the initial state of the control and ensemble members contain unavoidable error around the true state. As the time integration proceeds, the forecast error would develop against the initial error in spite of the perfect model setting. At t_i some time after the beginning, we start the forecast assimilation. Here, the ensemble members at t_i are regarded as of the observations corresponding to the ordinary data assimilation. We will refer to it as predicted observations. Then the predicted observations are assimilated into the background of the control forecast CF using the 3D-VAR and the Kalman filter, and analyzed value is obtained by the forecast assimilation. At the next time step t_{i+1}, the next predicted observation is assimilated into the analyzed background. The forecast assimilation is calculated every time step after the time t_i. This new type of the forecast is defined as an assimilated forecast (denoted as AF). Furthermore, the ensemble mean

(denoted as EM) at t_i can be utilized for the initial value of the next time integration for another forecast. The forecast is called a forecast from ensemble mean (denoted as FEM). In this experiment, we compare the forecast skill among control forecast CF, ensemble mean EM, forecast from the ensemble mean FEM, and the assimilated forecast AF at any time t_n. The forecast skill is defined by a root mean square (RMS) error between the truth (denoted as Tr) and the forecast. The RMS error is defined as,

$$\text{RMS} = \left(\frac{1}{N} \sum_{i=1}^{N} \left(F(i) - T(i) \right)^2 \right)^{1/2},$$
(3.1)

where $T(i)$ is the Tr and $F(i)$ is the forecast. Among these forecasts, the most superior forecast has the minimum RMS error.
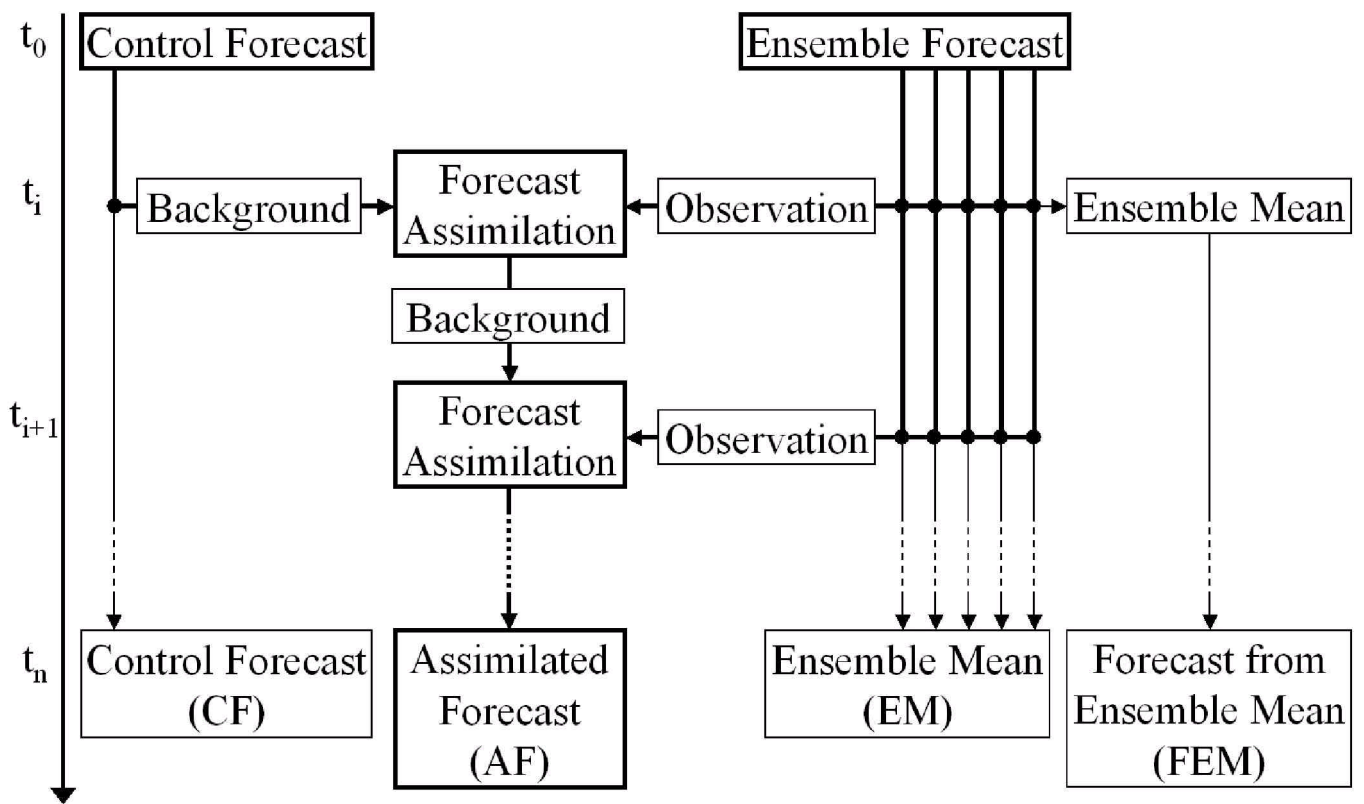
Figure 3.1: Schematic flowchart of the forecast assimilation. The bold arrows and boxes denote the stream of the forecast assimilation.

3.1.2 Lorenz model

In order to understand the features of the forecast assimilation, we consider the Lorenz model (Lorenz 1963), which has been studied by the comprehension of chaotic behavior and a nonlinear system (Sparrow 1982; Mukougawa et al. 1991). The Lorenz model consists of three differential equations,

$$
\begin{aligned}
\frac{dx}{dt} &= -\sigma(x - y), \\
\frac{dy}{dt} &= xz + \gamma x - y, \\
\frac{dz}{dt} &= xy - \beta z,
\end{aligned}
\tag{3.2}
$$

where σ, γ, and β are the model parameters. These equations were derived as a simplification of Saltzman's (1962) nonperiodic model for convection. The particular parameter values, $\sigma = 10$, $\gamma = 28$, $\beta = 8/3$, result in chaotic solution with unstable stationary solutions of $(\sqrt{\beta(1 + \gamma)}, \sqrt{\beta(1 + \gamma)}, 1 + \gamma)$, $(-\sqrt{\beta(1 + \gamma)}, -\sqrt{\beta(1 + \gamma)}, 1 + \gamma)$, and $(0, 0, 0)$.

Figure 3.2 illustrates trajectory of the Lorenz model in three dimensional perspective. The locations of three unstable stationary points are indicated by dots. The trajectory is not periodic, and two trajectories from the different initial states have never superimposed on each other. This complicated structures is known as a strange attractor. Therefore, since the chaotic behavior of the Lorenz model is more easily understood than the general circulation model, it has been used in many previous studies of ensemble prediction (Palmer 1993; Anderson 1997; Trevisan and Pancotti 1998), atmospheric predictability (Chu 1998) and data assimilation (Miller et al. 1994; Evensen 1997; Evensen and Fario 1997; Anderson and Anderson 1999).
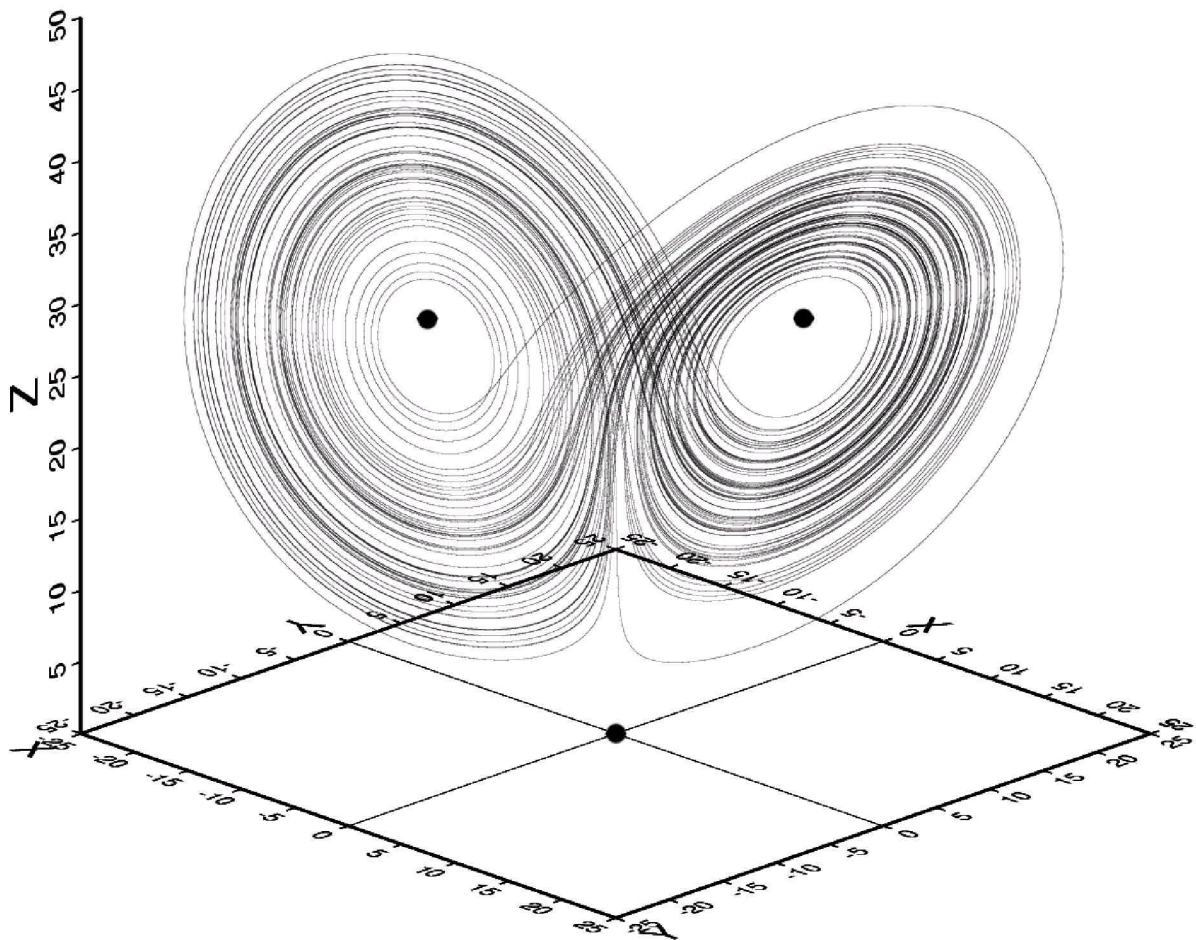
Figure 3.2: Trajectory of the Lorenz model in three dimensional perspective. The locations of three unstable stationary points are indicated by dots.

3.1.3   3D-Var

In the numerical weather prediction system, the data assimilation consists of estimating the initial conditions for the forecast using all available observations. During the 1980's and early 1990's, many operational weather forecasting centers utilize an optimal interpolation (OI) analysis for the routine data assimilation cycle (Lorenc 1981; Shaw et al. 1987). In the OI analysis, the observations are linearly interpolated into the forecasting result from a prior analysis (called background) with the observation error and background error for the weighting. However, several inherent weaknesses exist in the method. For instance, the OI analysis extracts information poorly from observations which are nonlinearly related to the model variables (Andersson et al. 1991).

A variational approach (Courtier 1997) circumvents some of the practical OI weaknesses, since it allows the analysis to use all the observations at every model grid point. After the late 1990's, many operational centers are using three dimensional variational data assimilation system called 3D-Var for the weather forecasting (Andersson et al. 1998; Courtier et al. 1998; Rabier et al 1998). The 3D-Var seeks an optimal balance between the observations scattered in the space and the background. Additionally, the 3D-Var allows the satellites data to interpolate to the analysis.

Recently, a four dimensional variational data assimilation system called 4D-Var is developed for the data assimilation. The 4D-Var seeks the optimal balance between the observations scattered in the time as well as in the space (Klinker et al. 2000; Mahfouf and Rabier 2000; Rabier et al. 2000). Although the quality of the analysis data produced by the 4D-Var is superior to the 3D-var, the analysis value by the 4D-Var equals the analysis value by the Kalman filter under the perfect model condition. The Kalman filter is explained in next Section 3.1.4 in detail. Therefore, the 3D-Var is adopted for the

forecast assimilation on behalf of the variational method.

A detail description of the 3D-Var is provided by Daley (1997) and Kalnay (2002), so only a brief description is presented in the following. The solution of the analysis is the model variables which most closely fits both the observations and forecast from a prior estimation, as measured by the following cost function J,

$$J(\mathbf{x}) = \frac{1}{2}\left\{(\mathbf{x} - \mathbf{x}_f)^T\mathbf{P}_f^{-1}(\mathbf{x} - \mathbf{x}_f) + (\mathbf{x}_o - H(\mathbf{x}))^T\mathbf{R}^{-1}(\mathbf{x}_o - H(\mathbf{x}))\right\}, \qquad (3.3)$$

where $\mathbf{x}$ is the resultant analysis vector, $\mathbf{x}_f$ is the background vector, $\mathbf{P}_f$ is the forecast error covariance matrix, $\mathbf{x}_o$ is the observation vector, H is observation operator that transfers from the dimension of the model state to the dimension of the observation state, $\mathbf{R}$ is the observation error covariance matrix, and the superscript T is the transpose of the matrix. The forecast error covariance matrix $\mathbf{P}_f$ is defined by a difference between $\mathbf{x}_f$ and true state $\mathbf{x}_t$ by

$$\mathbf{P}_f = \overline{(\mathbf{x}_f - \mathbf{x}_t)(\mathbf{x}_f - \mathbf{x}_t)^T}, \qquad (3.4)$$

where the overbar denotes an expectation value. Similarly the observation error covariance matrix $\mathbf{R}$ is defined by a difference between $\mathbf{x}_o$ and true state $\mathbf{x}_t$ by

$$\mathbf{R} = \overline{(\mathbf{x}_o - H(\mathbf{x}_t))(\mathbf{x}_o - H(\mathbf{x}_t))^T}. \qquad (3.5)$$

The cost function J is a quadratic function of the analysis increments $\mathbf{x}$. The gradient of J with respect to $\mathbf{x}$ is

$$\nabla J(\mathbf{x}) = \mathbf{P}_f^{-1}(\mathbf{x} - \mathbf{x}_f) + \mathbf{H}^T\mathbf{R}^{-1}\mathbf{H}(\mathbf{x} - \mathbf{x}_f) + \mathbf{H}^T\mathbf{R}^{-1}(\mathbf{x}_o - H(\mathbf{x}_f)), \qquad (3.6)$$

where $\mathbf{H}$ is the linearized H around the background value as

$$\mathbf{x}_o - H(\mathbf{x}) = H[\mathbf{x}_f + (\mathbf{x} - \mathbf{x}_f)] \qquad (3.7)$$

$$= \{\mathbf{x}_o - H(\mathbf{x}_f)\} - \mathbf{H}(\mathbf{x} - \mathbf{x}_f). \qquad (3.8)$$

When $\nabla J(\mathbf{x}) = 0$, then $J(\mathbf{x})$ is a minimum and $\mathbf{x}$ is the analysis $\mathbf{x}_a$.

For the forecast assimilation, the observations are the results of the ensemble forecast. Then the observations are the same variables in the model, so H is equal to an identity matrix $\mathbf{I}$. Therefore, Eq. (3.3) is rewritten as

$$J(\mathbf{x}) = \frac{1}{2} \left\{ (\mathbf{x} - \mathbf{x}_f)^T \mathbf{P}_f^{-1} (\mathbf{x} - \mathbf{x}_f) + (\mathbf{x}_o - \mathbf{x})^T \mathbf{R}^{-1} (\mathbf{x}_o - \mathbf{x}) \right\} \qquad (3.9)$$

The analysis $\mathbf{x}_a$ is obtained by the minimization of the cost function $J(\mathbf{x})$. The solution is obtained through minimization algorithms for $J(\mathbf{x})$ using iterative methods for minimization search as the conjugate gradient or quasi-Newton methods. The minimization technique is not shown here, so the detail description is referred to Press et al. (1992).

3.1.4 Kalman Filter

In order to examine the features of the forecast assimilation, we use Kalman filter with which many laboratories conduct experiments of the data assimilation for the weather forecasting (Bouttier and Courtier 1999; Anderson 2001; Hamill et al. 2001). On the other hand, the Kalman filter includes an explicit description of the evolution of the forecast error covariance in a data assimilation cycle, so the Kalman filter is superior to the variational analysis for the data assimilation. Therefore, we expect high performance of the forecast assimilation using the Kalman filter. Especially, the Kalman filter in the nonlinear system is called the extended Kalman filter, which we utilize for the forecast assimilation experiments in this study.

A detailed description of the extended Kalman filter is provided by Daley (1991) or Bouttier and Courtier (1999), so only a brief description is presented here. For the

extended Kalman filter, a nonlinear forecast model is required. Then a vector of a forecast $\mathbf{x}_f$ at time $i + 1$ is predicted using the nonlinear forecast model M and a vector of an analysis $\mathbf{x}_a$ at time i:

$$\mathbf{x}_f(i + 1) = M(\mathbf{x}_a(i)). \tag{3.10}$$

At the same time, we have some vectors which correspond to the observations $\mathbf{x}_o$ that have the same dimension as $\mathbf{x}_f$ and $\mathbf{x}_a$. In the forecast assimilation, $\mathbf{x}_o$ are calculated as the ensemble forecast by the same forecast model M rather than the true observation. Next, new analysis $\mathbf{x}_a$ is then obtained using the forecast $\mathbf{x}_f$ and the observation $\mathbf{x}_o$ by means of the following equation:

$$\mathbf{x}_a(i) = \mathbf{x}_f(i) + \mathbf{K}(i)[\mathbf{x}_o(i) - H(i)\mathbf{x}_f(i)], \tag{3.11}$$

where i is observation time, H is an observation operator, and $\mathbf{K}$ is the Kalman gain matrix given by

$$\mathbf{K}(i) = \mathbf{P}_f(i)\mathbf{H}^T(i)[\mathbf{H}(i)\mathbf{P}_f(i)\mathbf{H}^T(i) + \mathbf{R}(i)]^{-1}. \tag{3.12}$$

Here, $\mathbf{P}_f$ is a forecast error covariance matrix, $\mathbf{R}$ is an observation error covariance matrix, and $\mathbf{H}$ is a tangent linear matrix of the observational operator H in the vicinity of $\mathbf{x}_f$. In this experiment, the observations are the same variables in the model, so H and $\mathbf{H}$ are equal to an identity matrix $\mathbf{I}$. Therefore, Eq. (3.11) and Eq. (3.12) are rewritten as

$$\mathbf{x}_a(i) = \mathbf{x}_f(i) + \mathbf{K}(i)[\mathbf{x}_o(i) - \mathbf{x}_f(i)], \tag{3.13}$$

$$\mathbf{K}(i) = \mathbf{P}(i)_f[\mathbf{P}(i)_f + \mathbf{R}(i)]^{-1}. \tag{3.14}$$

The observation error covariance matrix $\mathbf{R}$ may be defined by a difference between $\mathbf{x}_o$ and true state $\mathbf{x}_t$ by

$$\mathbf{R} = \overline{(\mathbf{x}_o - \mathbf{x}_t)(\mathbf{x}_o - \mathbf{x}_t)^T}, \tag{3.15}$$

where the overbar denotes an expectation value. The $\mathbf{P}_f$ is predicted for the next time step using the model, and given by the next two equations,

$$\mathbf{P}_a(i) = [\mathbf{I} - \mathbf{K}(i)]\mathbf{P}_f(i), \tag{3.16}$$

$$\mathbf{P}_f(i+1) \;=\; \mathbf{M}(i)\mathbf{P}_a(i)\mathbf{M}^T(i) + \mathbf{Q}(i), \tag{3.17}$$

where $\mathbf{P}_a$ is an analysis error covariance matrix, and Eq. (3.17) indicates the forecast of $\mathbf{P}_f$ using the tangent linear model matrix $\mathbf{M}$ of the nonlinear forecast model M with a model error covariance matrix $\mathbf{Q}$.

Eqs. (3.10) and (3.17) are the prediction portion of the extended Kalman filter, and Eqs. (3.13), (3.14) and (3.16) are the analysis portion. Figure 3.3 indicates an organization of computations for the extended Kalman filter. First, the forecast $\mathbf{x}_f$ is integrated by Eq. (3.10) from the previous analysis $\mathbf{x}_a$. And the forecast error covariance matrix $\mathbf{P}_f$ is integrated by Eq. (3.17) using $\mathbf{P}_a$, $\mathbf{M}$, and $\mathbf{Q}$. Next, the Kalman gain $\mathbf{K}$ is derived by Eq. (3.14). Then the observation $\mathbf{x}_o$ is assimilated into the forecast $\mathbf{x}_f$ by Eq. (3.13) to obtain the analysis $\mathbf{x}_a$. And $\mathbf{P}_a$ is derived by Eq. (3.16). For the next step of the assimilation, $\mathbf{x}_f$ and $\mathbf{P}_f$ are integrated by Eqs (3.10) and (3.17) using $\mathbf{x}_a$ and $\mathbf{P}_a$. Therefore, the extended Kalman filter is routinely calculated.

For the forecast assimilation, if the forecast error covariance matrix $\mathbf{P}_f(t_i)$, the observation error covariance matrix $\mathbf{R}(t_i)$, the model error covariance matrix $\mathbf{Q}(t_i)$, and the observation $\mathbf{x}_o(t_i)$ are determined at first step of the forecast assimilation in Fig. 3.1, the analysis $\mathbf{x}_a$ can be routinely calculated for every time step of the forecast model. Now, $\mathbf{x}_o(t_i)$ is randomly chosen among the ensemble members. $\mathbf{P}_f(t_i)$ is assumed as $\mathbf{P}_f(t_i) = \mathbf{R}(t_i)$, because the distance between the control forecast and the truth equals the average distance between each ensemble member and the truth. Furthermore, we assume a perfect model for M, so $\mathbf{Q} = 0$. Unfortunately, it is impossible to obtain $\mathbf{R}(t_i)$ in Eq. (3.15) because the future of the true value is unknown for us. Therefore, we consider that $\mathbf{R}(t_i)$ is obtained from an ensemble Kalman filter technique (Evensen 1994; Burgers et al. 1998), which uses an ensemble forecast to estimate $\mathbf{R}(t_i)$. In the ensemble Kalman filter, the ensemble covariance matrix $\mathbf{R}_e(i)$ is used with the ensemble mean $\overline{\mathbf{x}_e}$ for the

substitute of $\mathbf{x}_t$

$$\mathbf{R}(i) \simeq \mathbf{R}_e(i) = \overline{(\mathbf{x}_o(i) - \overline{\mathbf{x}_e(i)})(\mathbf{x}_o(i) - \overline{\mathbf{x}_e(i)})^T}. \tag{3.18}$$

In the data assimilation, since we cannot know the truth, $\mathbf{R}$ is calculated by previous $\mathbf{x}_o$ and the analysis value instead of $\mathbf{x}_t$. Similarly, since $\overline{\mathbf{x}_e}$ is a better estimation of the truth than the control forecast or ensemble members in the future state, the $\mathbf{R}_e(i)$ is considered as the $\mathbf{R}(i)$. Therefore, the assimilated forecast is continuously calculated by the forecast assimilation system using the ensemble members.

The extended Kalman filter is superior to the variation method. Even if a system starts with poor initial guess of the state of the atmosphere, the Kalman filter may go through an initial transient, after which it should provide the best linear unbiased estimate of the state of the atmosphere and its error covariance (Kalnay 2002). However if the system is very unstable, and the observations are not frequent enough, it is possible for the linearization to become inaccurate, and the extended Kalman filter may drift away from the true solution (Miller et al. 1994).

Here, we check the quality of the extended Kalman filter using the Lorenz model. The truth is calculated from initial value $(x, y, z) = (1.508870, -1.531271, 25.46091)$. The observations are sequentially constructed from the truth adding Gaussian distribution noise with variance equals to 4.0 every 0.01 time step. First, the initial state of analysis is guessed, which is $(-20.0, -1.5, 25.4)$. Figure 3.4 shows the results of the Kalman filter for the Lorenz model from $t = 0$ to $t = 1.0$ (denoted as 0.0T to 1.0T). At the beginning of the data assimilation (0.0T), the analysis has large error that exceeds 10.0 root mean square (RMS) error. After the 5 step of the data assimilation (0.05T), the trajectory of the analysis is close to the truth, and the RMS error of analysis is reduced under 1.0. After that, the analysis becomes sufficiently closer to the truth than the observations. Figure 3.5 shows same as Fig. 3.4, but the time is extended to 10.0T. At times of 1.2T,

3.7T, 6.5T, 7.3T, the RMS error of analysis become fluctuative because of the unstable stage of the Lorenz model. The fluctuative RMS error coincides with the large norm of the Kalman gain in Fig. 3.6. When the norm of the Kalman gain is large, the status of the trajectory is unstable, and the mixing ratio of the observation into the background is increasing. Nevertheless, the analysis produced by the Kalman filter does not drift away from the truth. Since the assimilated time step is 0.001 for the forecast assimilation, the Kalman filter performs desirably.
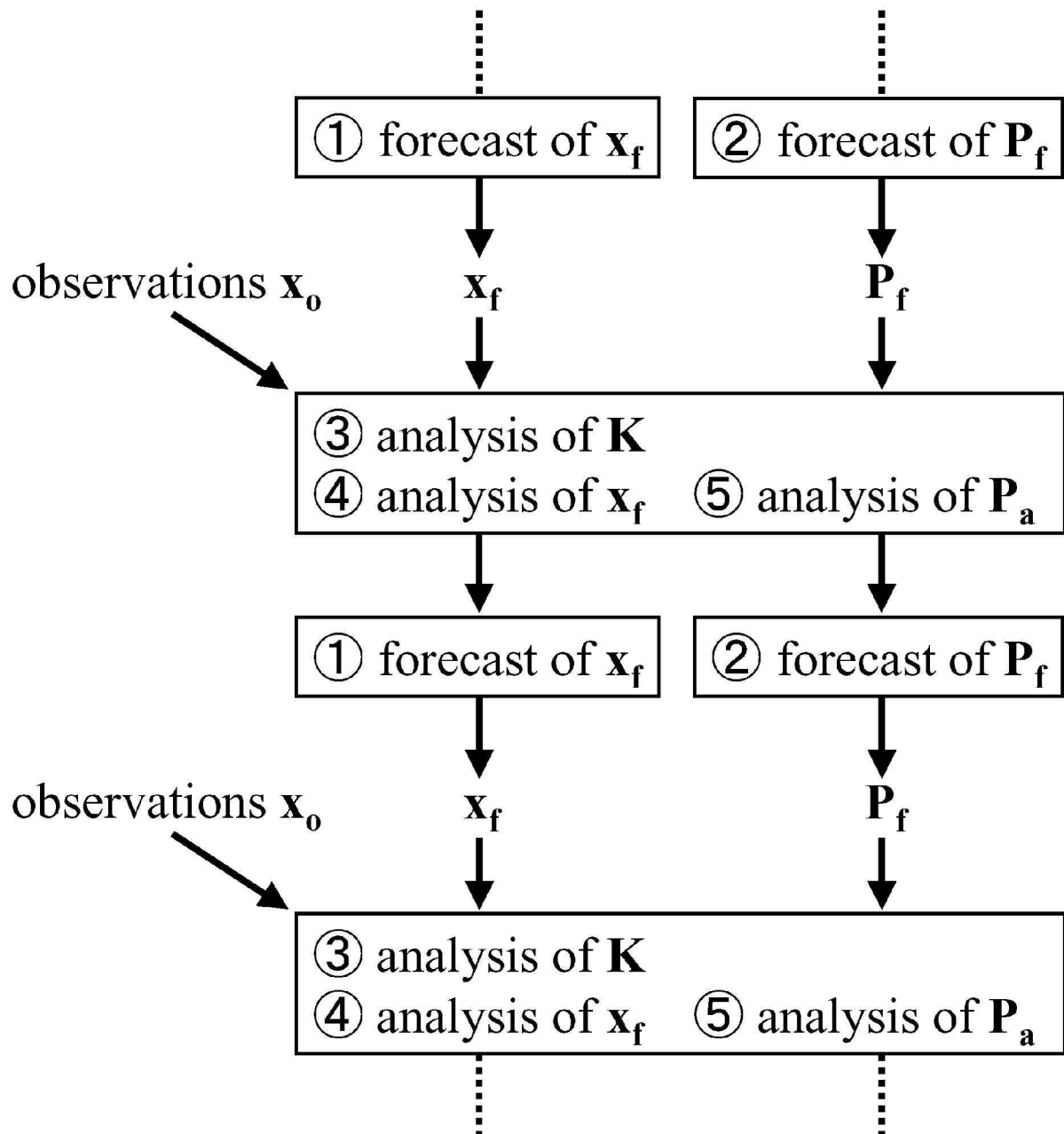
Figure 3.3: A organization of computations in an extended Kalman filter.
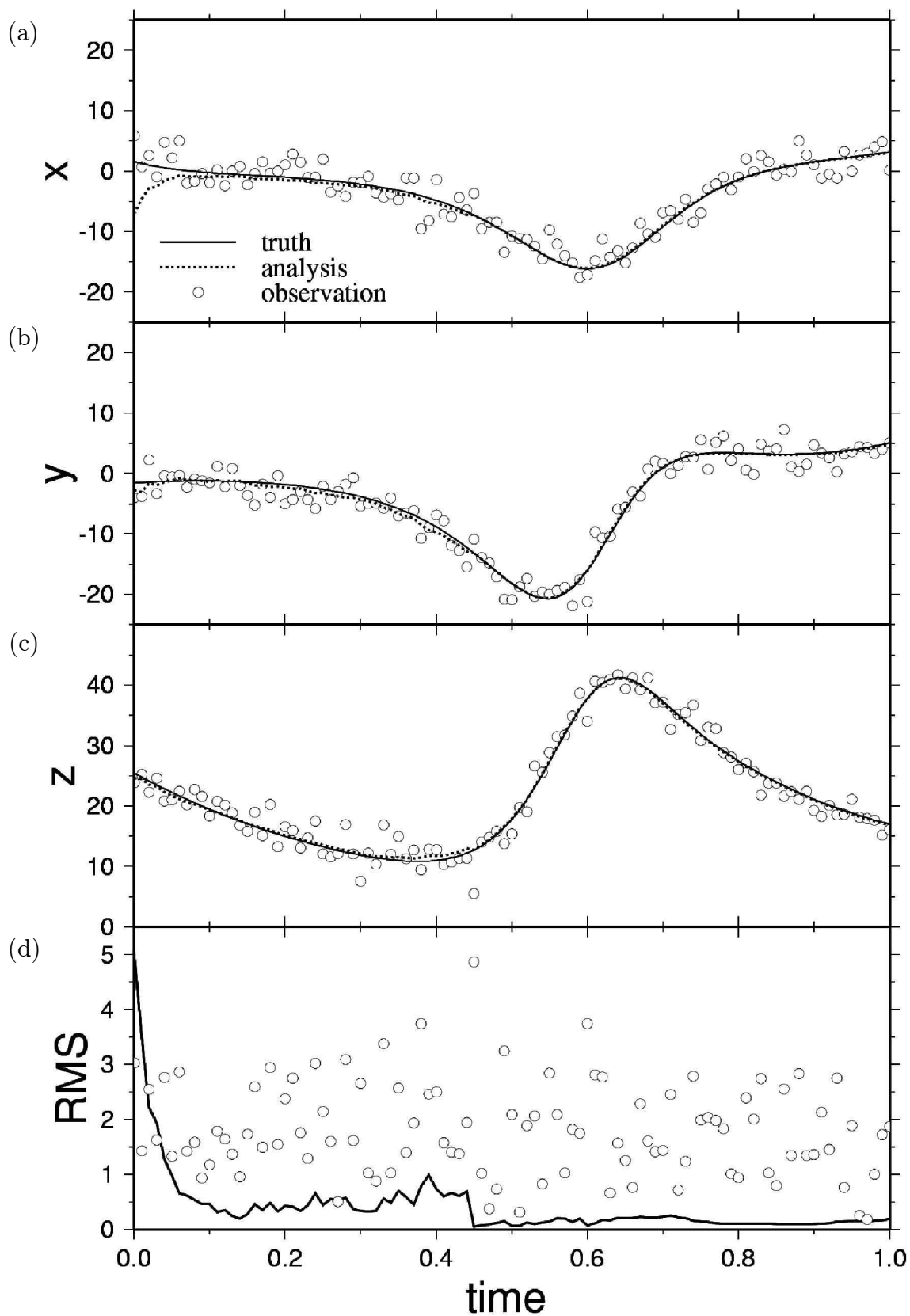
Figure 3.4: Results of the data assimilation using the Kalman filter for the Lorenz model from 0.0T to 1.0T. (a) time variation of value of x variable. The truth is given by the solid line, the analysis is given by dotted line, and the observations are given by circle. (b) y variable. (c) z variable. (d) RMS error for the analysis and the observations.
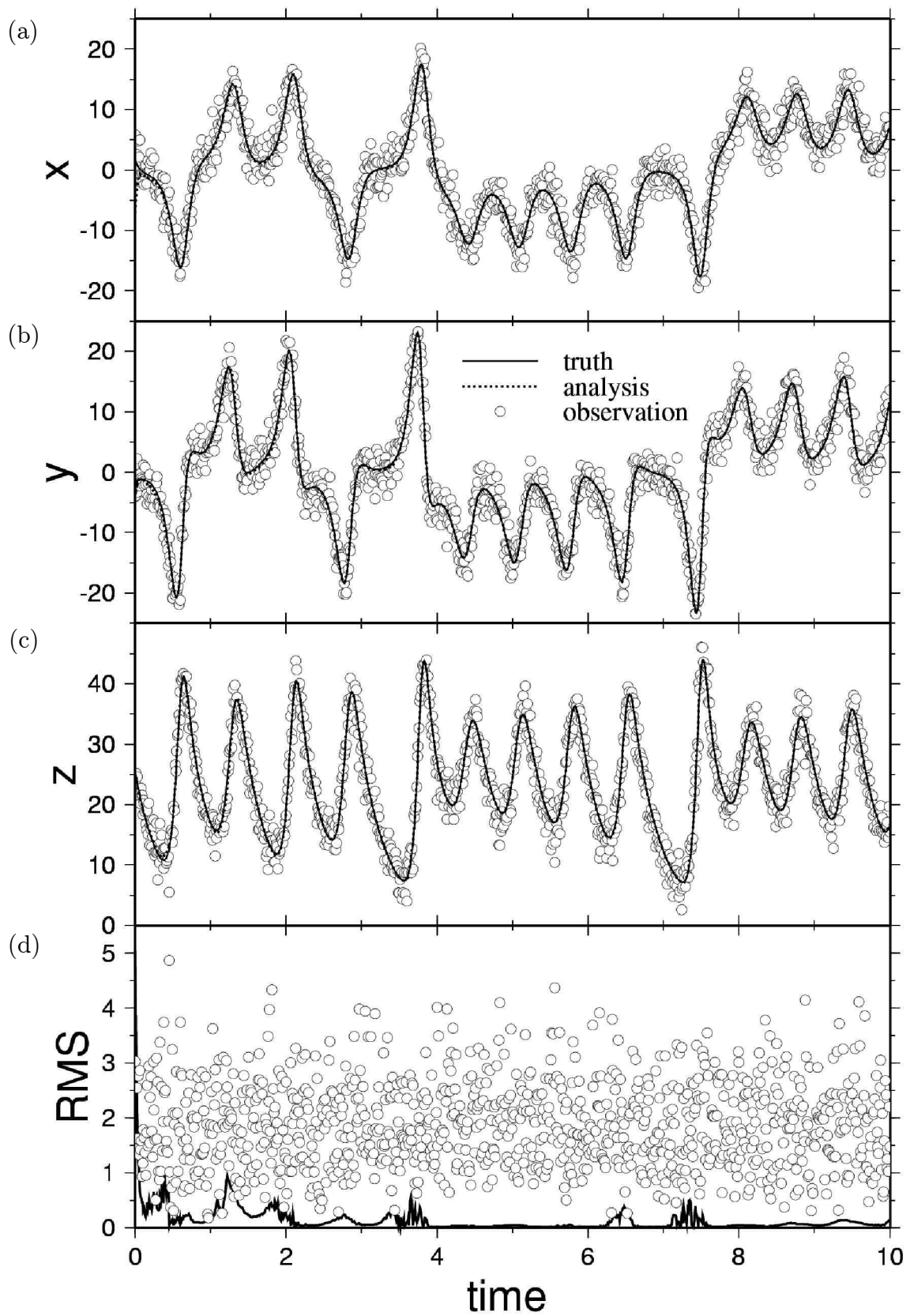
Figure 3.5: Same as Fig. 3.4, but from 0.0T to 10.0T.
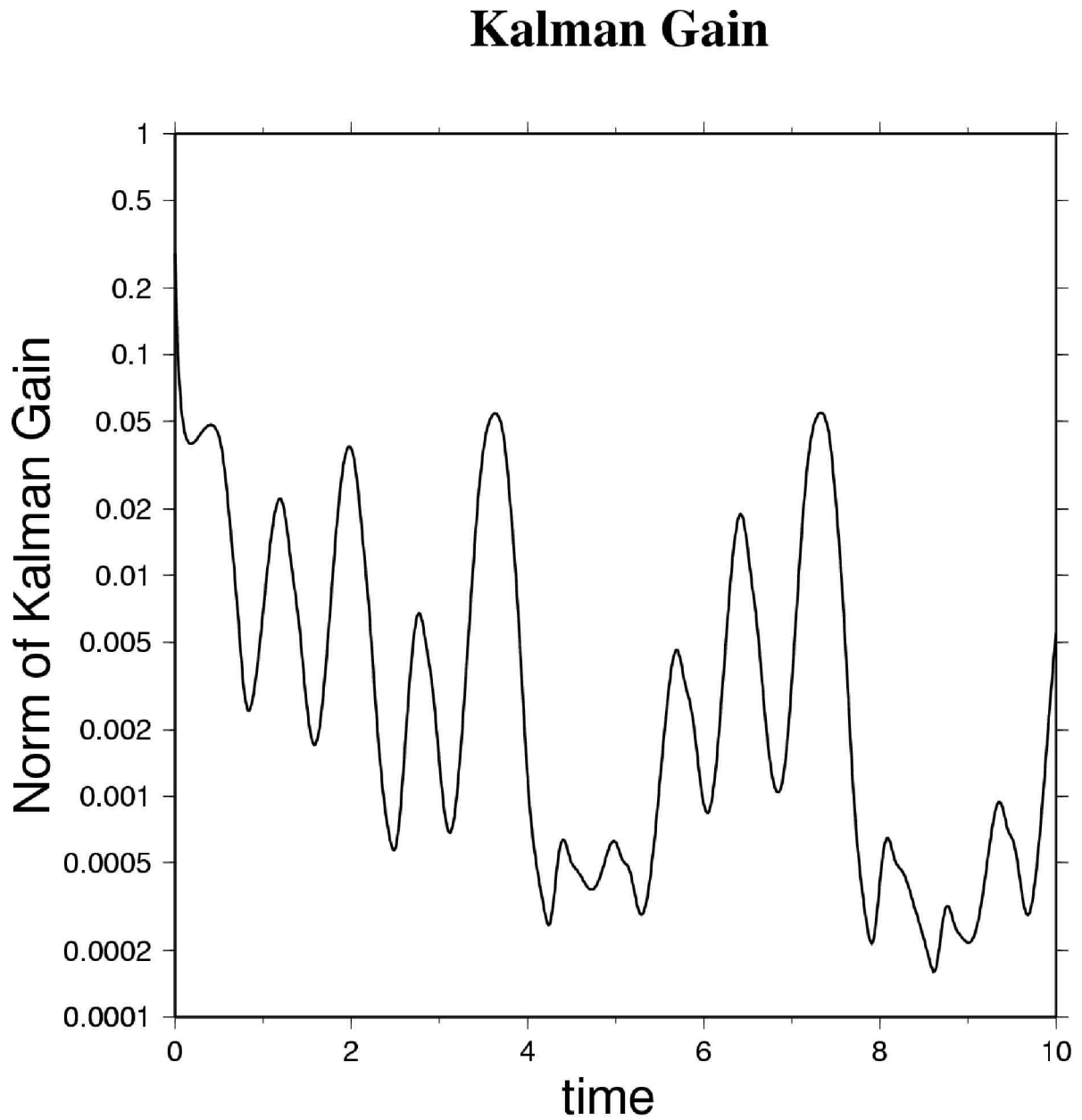
Kalman Gain

Figure 3.6: Norm of Kalman gain matrix. The range of time is same as Fig. 3.5

3.2 Results

3.2.1 Forecast Assimilation using 3D-Var

First, a control forecast $\mathbf{x}_f$ and n members of the ensemble forecasts $\mathbf{x}_i$ are integrated from the truth Tr adding Gaussian noise with zero mean and some variance in the nonlinear dynamical system. Then the ensemble mean indicates the best forecast without adapting the forecast assimilation. The distribution of the ensemble members (denoted as EMem) is stretched by a linear regime of the error growth at the beginning of the forecast. After that, the nonlinear effect becomes dominant to distort the distribution. The forecast assimilation is then started when the errors of the ensemble forecasts have grown to a certain threshold.

For the forecast assimilation, the EMem $\mathbf{x}_i$ is regarded as the predicted observation $\mathbf{x}_o$. Then the observation error covariance matrix $\mathbf{R}$ is obtained by Eq. (3.5) using the EMem $\mathbf{x}_i$ and Tr $\mathbf{x}_t$ as

$$\mathbf{R} = \overline{(\mathbf{x}_i - \mathbf{x}_t)(\mathbf{x}_i - \mathbf{x}_t)^T}. \tag{3.19}$$

Similarly, the forecast error covariance matrix $\mathbf{P}_f$ is obtained by Eq. (3.4) using the control forecast $\mathbf{x}_f$ as

$$\mathbf{P}_f = \overline{(\mathbf{x}_f - \mathbf{x}_t)(\mathbf{x}_f - \mathbf{x}_t)^T}. \tag{3.20}$$

Since the mean and variance of the error for the individual EMem from the Tr theoretically equals to an error for the control forecast $\mathbf{x}_f$, the relation between $\mathbf{R}$ and $\mathbf{P}_f$ is considered as

$$\mathbf{R} = \mathbf{P}_f. \tag{3.21}$$

If all EMem are available to the forecast assimilation at the same time, the cost

function J from Eq. (3.9) is given by

$$J(\mathbf{x}) = \frac{1}{2} \left\{ (\mathbf{x} - \mathbf{x}_f)^T \mathbf{P}_f^{-1} (\mathbf{x} - \mathbf{x}_f) + \sum_{i=1}^{n} (\mathbf{x} - \mathbf{x}_i)^T \mathbf{P}_f^{-1} (\mathbf{x} - \mathbf{x}_i) \right\}. \qquad (3.22)$$

The gradient of J is obtained by differentiating Eq. (3.22) with respect to $\mathbf{x}$,

$$\nabla J(\mathbf{x}) = \mathbf{P}_f^{-1} (\mathbf{x} - \mathbf{x}_f) + \sum_{i=1}^{n} \mathbf{P}_f^{-1} (\mathbf{x} - \mathbf{x}_i). \qquad (3.23)$$

At the minimum of J, the gradient cost function of Eq. (3.23) is given by

$$\nabla J(\mathbf{x}) = 0. \qquad (3.24)$$

Since $\mathbf{x}_f$ is considered as a zero-th EMem ($\mathbf{x}_f = \mathbf{x}_0$), so Eq. (3.23) is rewritten by

$$\sum_{i=0}^{n} \mathbf{P}_f^{-1} (\mathbf{x} - \mathbf{x}_i) = 0. \qquad (3.25)$$

Therefore, we obtain the best analysis $\mathbf{x}_a$ as

$$\mathbf{x}_a = \frac{\sum_{i=0}^{n} \mathbf{x}_i}{n+1}. \qquad (3.26)$$

This equation indicates the ensemble mean. Therefore, the consequence of the forecast assimilation using the 3D-Var results in the ensemble mean of the EMem.

3.2.2 Forecast Assimilation using Kalman Filter

First, a truth (Tr) is integrated using the Lorenz model with an initial state given by $(x_0,\ y_0,\ z_0) = (1.508870,\ -1.531271,\ 25.46091)$ for time $t = 0.0$ to $t = 50000.0$ with 0.001 time step. The Tr is divided into 5000 sectors for every $\Delta t = 10.0$ (denoted as 0.0T to 10.0T). The examination of the forecast assimilation is carried out for the every sector. A control forecast (CF) and 200 members of the ensemble forecast are integrated from the start point of each sector of the Tr adding Gaussian noise with zero mean and

variance equals to 0.0025. First, the observation error covariance matrix $\mathbf{R}$ at Eq. (3.18) is calculated from the 100 members of the ensemble forecast. The remaining 100 members are utilized for the forecast assimilation. Figure 3.7 shows the initial distribution of the Tr, CF, 100 members of ensemble forecast, and the ensemble mean (EM) on x-y plane at 0.0T for an example of a sector. The average root mean square (RMS) error of the CF and the each ensemble member EMem against the Tr is 0.05. Nevertheless, the RMS error of the EM nearly equals to zero because the distribution of the ensemble members (EMem) is Gaussian around the Tr. As a time proceeds, the EMem diverge by the linear and nonlinear effects of the Lorenz model, so the RMS error of the EMem exponentially increases, and the unimodal distribution evolves into a bimodal distribution.

As the first example, we describe one result of the forecast assimilation on a sector with a good forecast skill. The forecast assimilation is started at 3.5T with 0.001 time step, and a predicted observation is randomly chosen from the 100 EMem. Figure 3.8 illustrates forecast distributions of the Tr, CF, EMem, and EM on x-y plane at 3.5T. The distribution of the EMem describes an arc, and the Tr and CF lie on the arc. The EM, however, is located apart from the arc.

The first step of the forecast assimilation is that the randomly chosen EMem is assimilated into the CF in Fig. 3.1. Figure 3.9 shows trajectories and RMS error of the Tr, CF, EM, forecast from the ensemble mean (FEM), and assimilated forecast (AF) on the early stage (to 3.68T) of the sector examined. The predicted observation is scattered below the Tr on x and y planes. At the beginning, trajectory of the AF in Fig 3.1 (a) – (c) is fluctuated due to searching the Tr for the effect of the forecast assimilation with model integration. The other forecasts (CF, FEM, and EM) become relaxed trajectories for the effect of the only model integration. Even though the RMS error of the AF also fluctuates, it decreases to the error level that is lower than the EM. Then the RMS error of the

AF becomes stable at 3.56T in spite of large spread of the predicted observation. Figure 3.10 illustrates the early evolution of the forecast distributions of the Tr, CF, EMem, EM, FEM, and AF on x-y plane. Although the AF approaches to the Tr at 3.525T, it is located farther than the EM from the Tr at 3.550T. After 3.575T, the AF is located in the neighborhood of the EM, but slightly closer to the Tr. The location of the FEM is almost overlaid on the EM in this forecasting range.

Continuously, the forecast assimilation is calculated. Figure 3.11 shows continuous results of Fig. 3.9. After time 4.0T, the distribution of the predicted observations spreads widely around the Tr, and the CF is apart continuously from the Tr. Then, the fluctuation of the AF is increasing for the spread predicted observations from Eq. (3.13) and reinforcement of the nonlinearity in the model states from Eqs. (3.10) and (3.17). Figure 3.12 plots the time variation of the norm of the Kalman gain matrix. The range of the forecast time is same as in Fig 3.11. When the norm of the Kalman gain is large, the status of the trajectory is unstable from Eq. (3.17), and mixing ratio of the predicted observation into the background is increasing from Eq. (3.14). Although in Fig. 3.11 the AF accumulates the observations with large error, the trajectory of the AF is close to the Tr, and the RMS error becomes one or two order smaller than the other forecasts. Figure 3.13 illustrates continuation of Fig. 3.10. A unimodal distribution of the EMem at 3.6T in Fig. 3.10 is stretched at 4.0T and changes to bimodal at 4.5T. Then, the EM is seen at the center of the two distributions. Therefore, the RMS error of the EM is larger than the AF at 4.5T even if the EM is located in the neighborhood of the Tr and the AF at 4.0T. On the other hand, the AF that has obtained some positional information about the Tr from some predicted observations lays on the Tr at 4.5T.

The forecast assimilation experiment is repeated for 5000 sectors to increase the statistical confidence. The 5000 sectors have each different initial states. Figure 3.14 shows

the distribution of the initial states of the 5000 sectors on the Lorenz model. To compare with Fig. 3.2, the distribution of the initial states almost covers the trajectory of the Lorenz model. Therefore, it is indicated that the averaged results of the 5000 repeated forecasts become independent of the initial states.

Figure 3.15 illustrates averaged RMS error for 5000 samples of the CF, EM, FEM, and AF. In this case, it is indicated that the averaged RMS error of each EMem is comparable to the error level of the CF. The RMS error of all forecasts except for the AF are exponentially growing at the early stage. Specially the error of the FEM rapidly grows. After the 5.0T, the error growth speeds are slow down, and the errors gradually saturates by the nonlinear effect. In this situation, all forecast assimilations in every sector are started at 3.5T. The RMS error of the AF, which has the same error as the CF at the starting time of assimilation, decreases below the EM in a short time. After 3.8T, the RMS error of the AF is exponentially increasing as in the CF or EM. At 6.0T, the RMS error of the AF exceeds the EM and the FEM. When the RMS error of the CF or EMem approach to the saturated level, the predicted observation used by the forecast assimilation has little positional information of the true state. Therefore, the error of the AF close to the saturated level grows more rapidly than the normal forecast. Then the EM approaches to the climatology.

The effect of the forecast assimilation depends on the distribution of the EMem. Immediately after the start of the ensemble forecast, the distribution is similar to Gaussian for the linear regime of the error growth. If the forecast assimilation starts earlier than 3.5T, it is expected that the AF collects better positional information about the Tr because the EMem are close to the normal distribution that is favorable to the Kalman filter. Likewise, the state of the EM and the initial state of the FEM are significantly close to the Tr for hyper elliptic distribution. Therefore, it is necessary to compare the

forecast skill of the AF with the CF, the FEM, and the EM in various starting times of the forecast assimilation.

Figure 3.16 illustrates the ratio of RMS error of the AF against the CF. The abscissa indicates the forecast time and the ordinate indicates the starting time of the forecast assimilation. The area where the AF is more skillful than the CF is shaded (the ratio is smaller than 1). In this result, the error level of the CF as time proceeds is comparable to RMS error of the CF in Fig. 3.15. Similarly, the average error of each EMem is comparable to RMS error of the CF in Fig. 3.15. Until 6.0T forecast time, the forecast skill of the AF is superior to the CF regardless of the starting time of the forecast assimilation. After the 6.0T starting time of the forecast assimilation, the skill of AF is inferior to the CF because the error of the predicted observation for the forecast assimilation is saturated. Figure 3.17 illustrates the ratio of RMS error of the AF against the FEM. Until 2.0T starting time of the forecast assimilation, the forecast skill of the AF is inferior to the FEM regardless of the forecast time, because the EM is close to the Tr for hyper elliptic distribution of the EMem. After 2.0T starting time of the forecast assimilation, the skill of the AF is superior to the forecast from the ensemble forecast. Since the EM is detached from the center of the distribution of the EMem for the nonlinear effect, the EM for the initial state is unstable to predict the Tr. On the other hand, the AF is considered that the error growth for the nonlinear effect along the time evolution.

Figure 3.18 illustrates the ratio of RMS error of the AF against the EM. From 2.5T to 6.0T forecast time, the forecast skill of the AF is superior to the EM irrespective of the starting time of the forecast assimilation. The distribution of the EMem is slightly folded by the nonlinear effect, so the EM is detached from the center of the distribution of the EMem. The AF is, however, inferior before 2.5T, since the EM is located near the Tr by the assumption of the error distribution centered around the Tr. In addition, it

is inferior after 6.0T, since the EMem have little positional information of Tr because of saturated forecast error of the EMem. Nevertheless, the AF has a good performance at the intermediate where the nonlinear growth dominates but is not saturated.
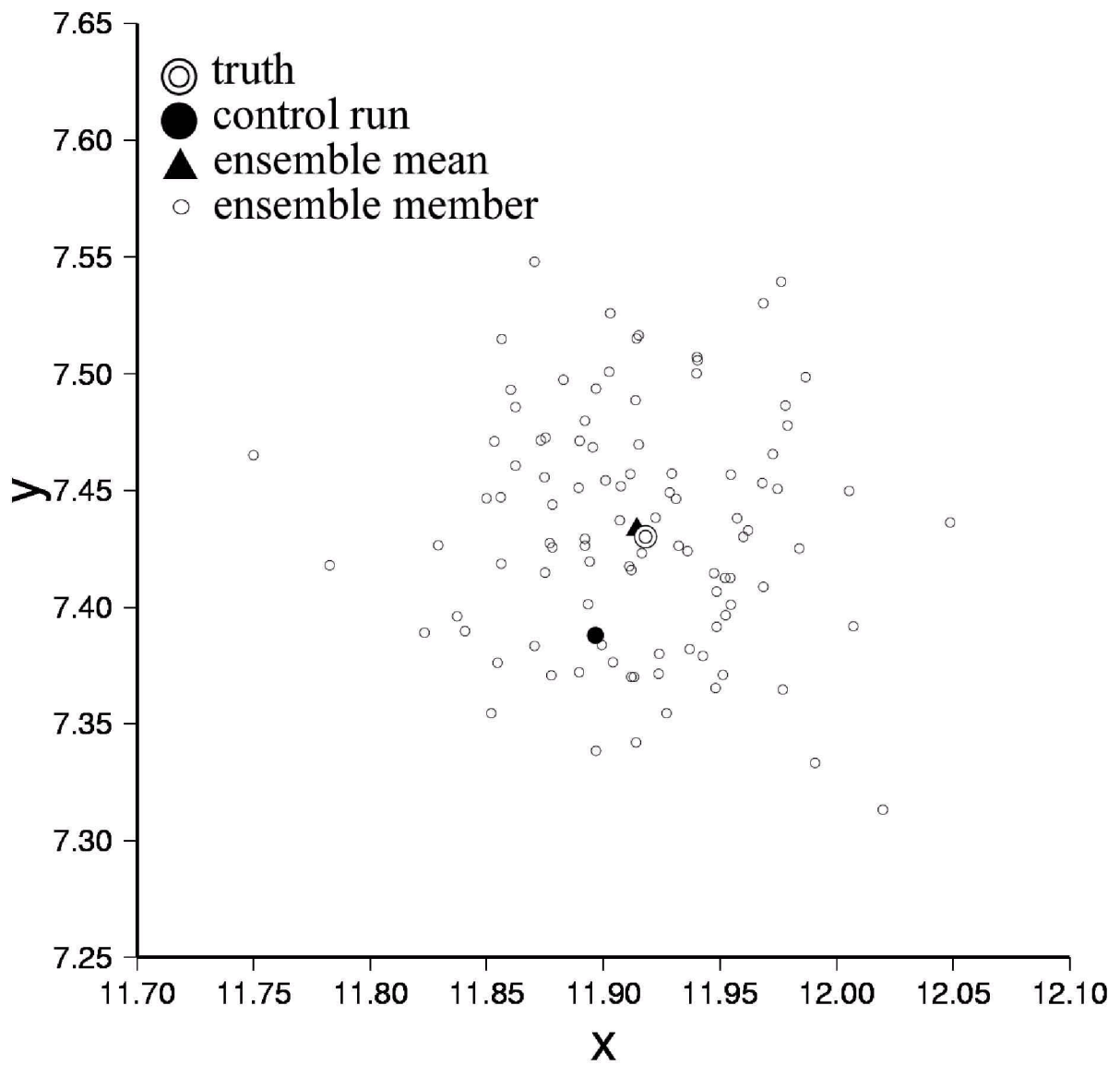
Figure 3.7: Initial distribution of the true run, control forecast CF, ensemble members, and the ensemble mean EM on x-y plane at 0.0T. The ensemble members are normally distributed around the truth.
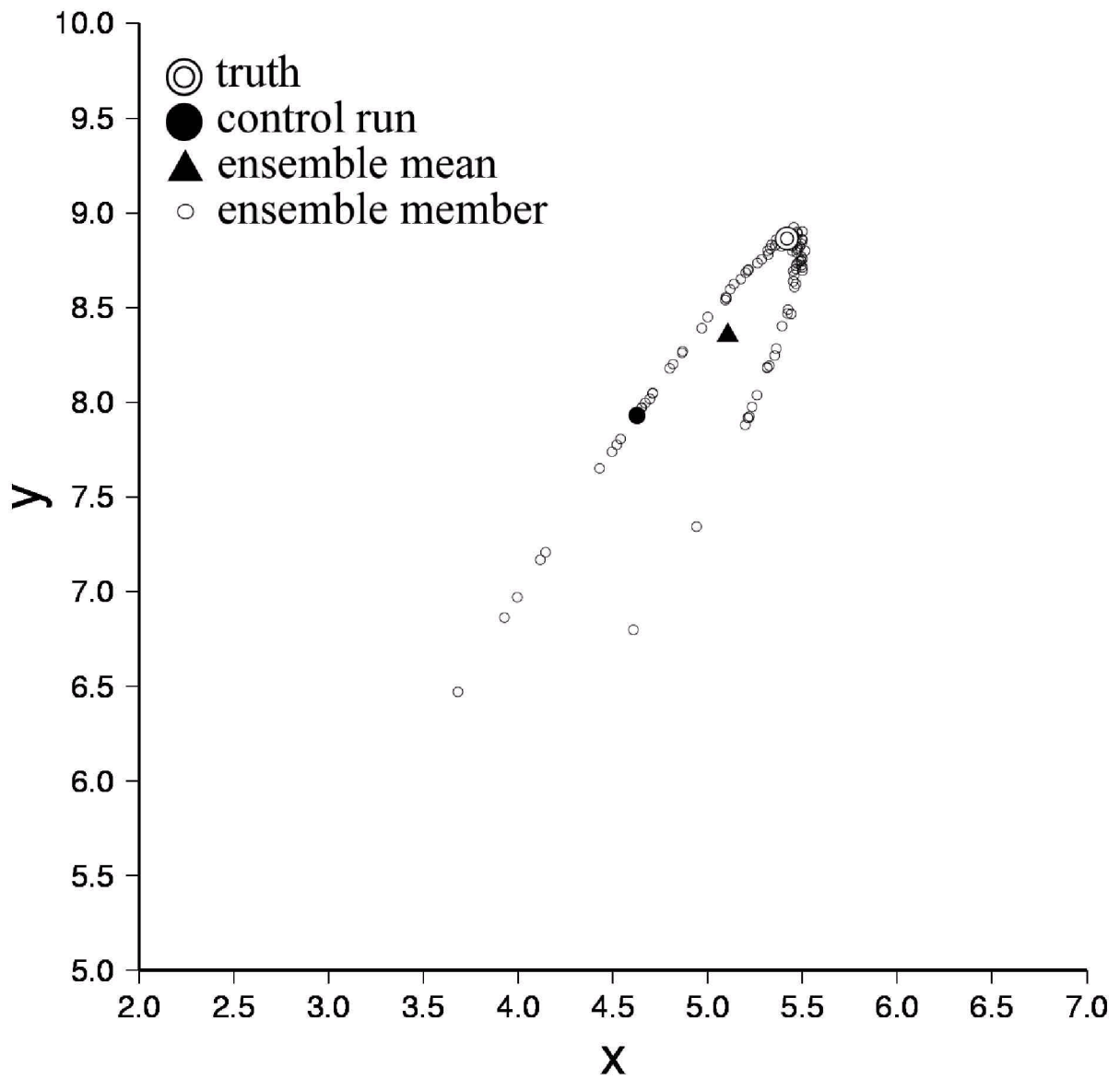
Figure 3.8: Same as Fig 3.7, but for the starting point of the forecast assimilation at 3.5T. The distribution of the forecast describes an arc.
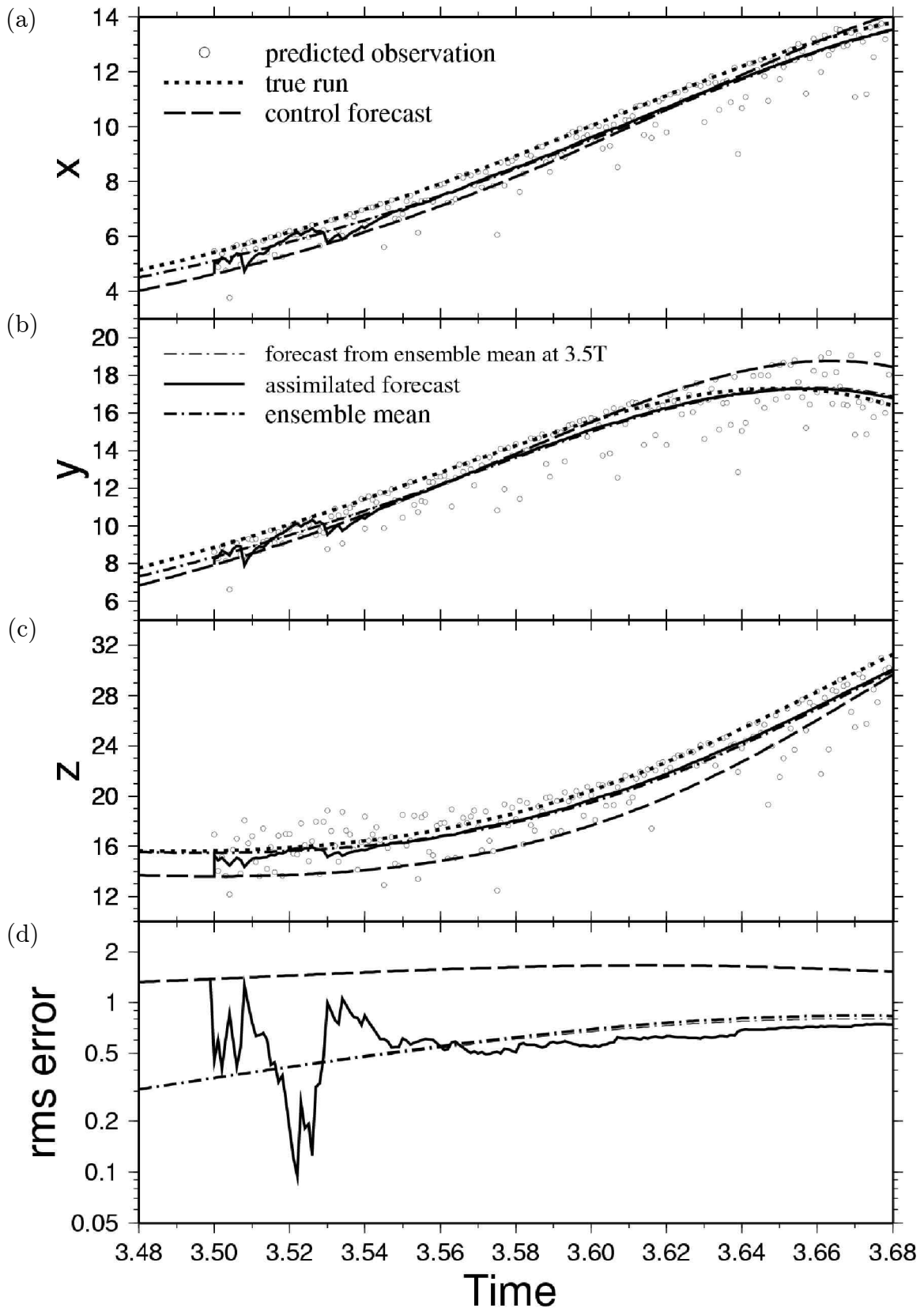
Figure 3.9: Forecasting result of the truth, control forecast CF, ensemble mean EM, forecast from ensemble mean FEM, predicted observation, and assimilated forecast AF from 3.48T to 3.68T. The forecast assimilation is started at 3.5T. (a) time variation of value of x variable. (b) y variable. (c) z variable. (d) RMS error for CF, EM, FEM, and AF.
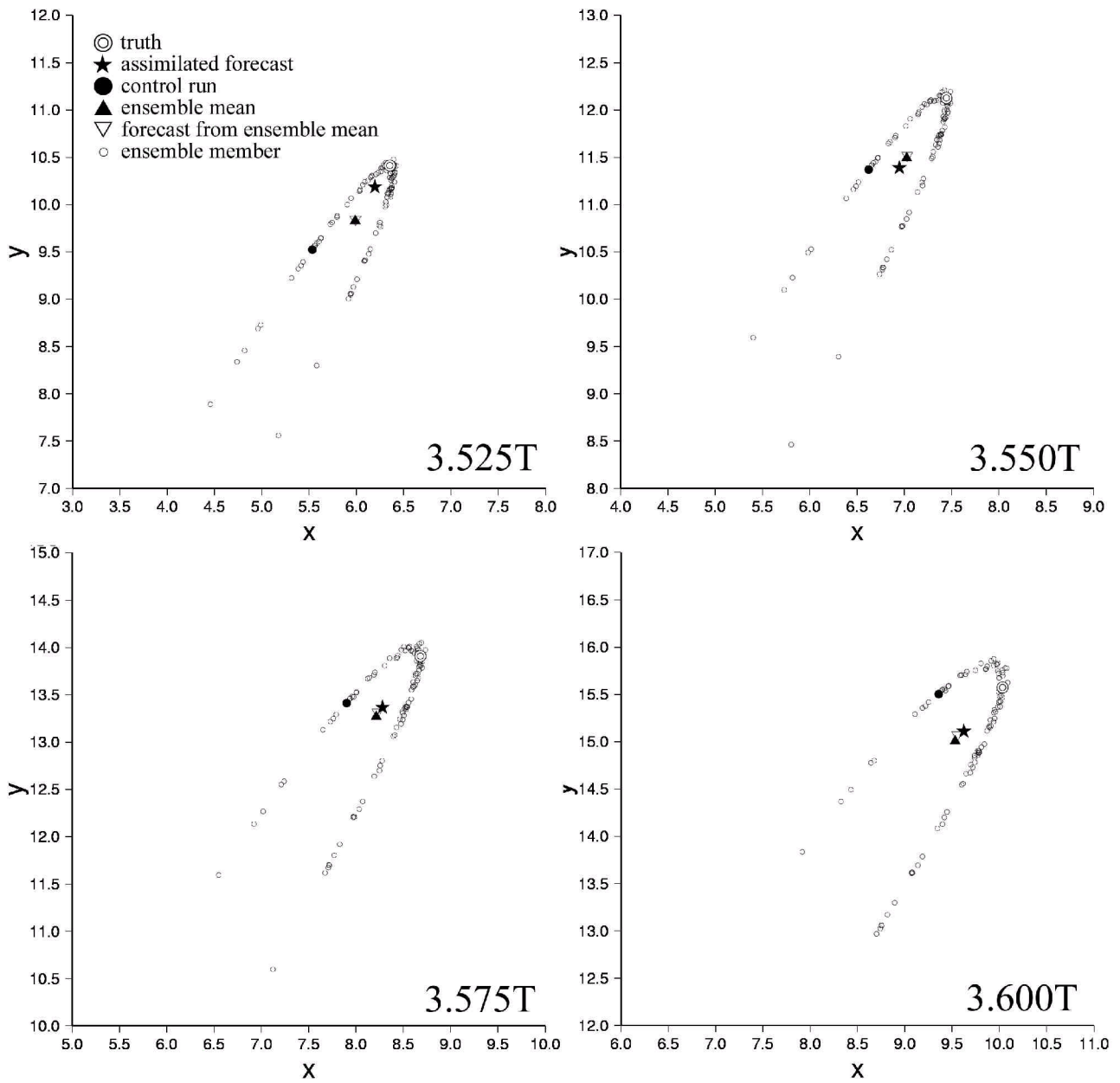
Figure 3.10: Evolution of the forecast distributions of the true run, control forecast, ensemble members, the ensemble mean, forecast from ensemble mean, and assimilated forecast on x-y plane.
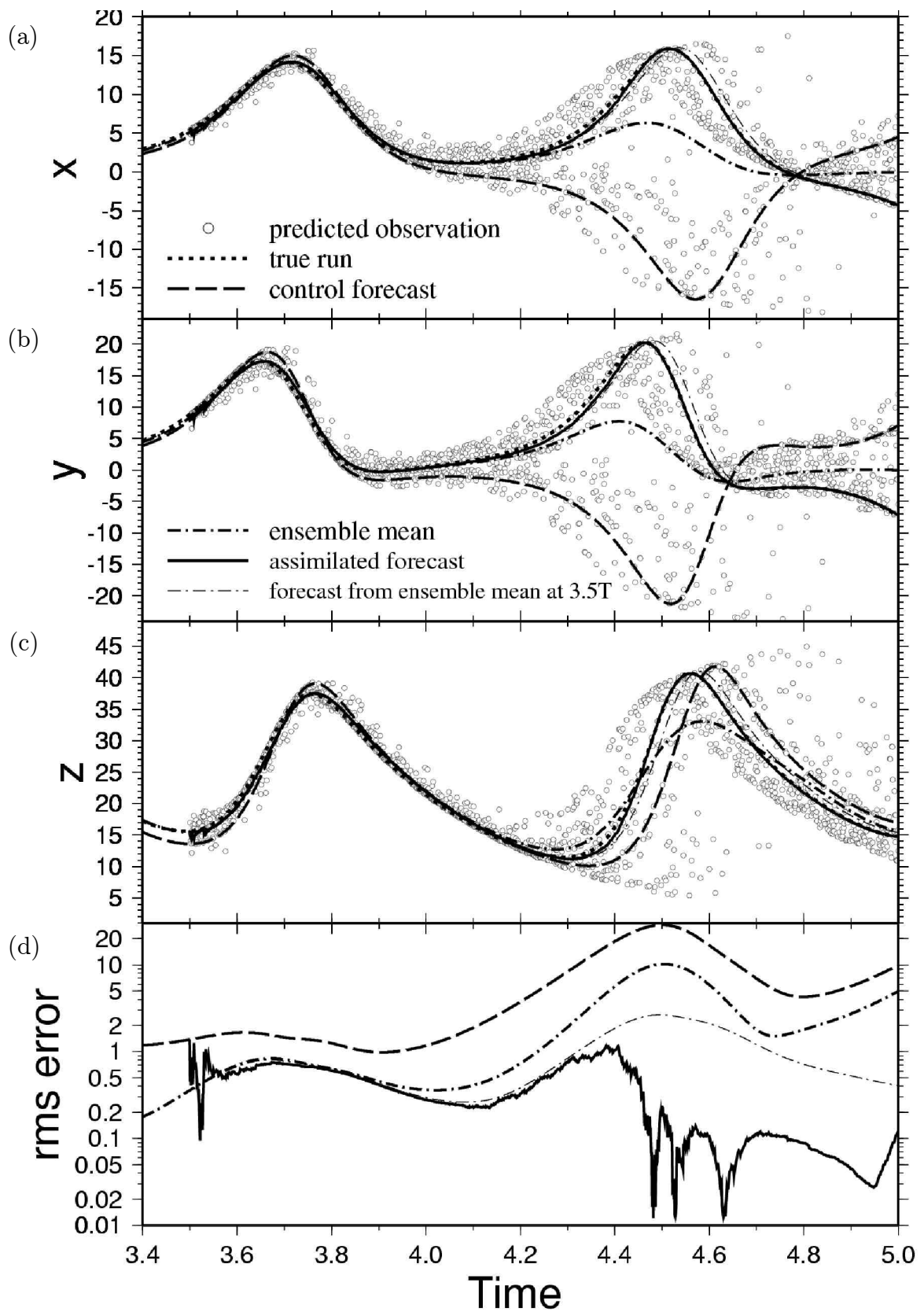
Figure 3.11: Same as Fig. 3.9, but from 3.4T to 5.0T.
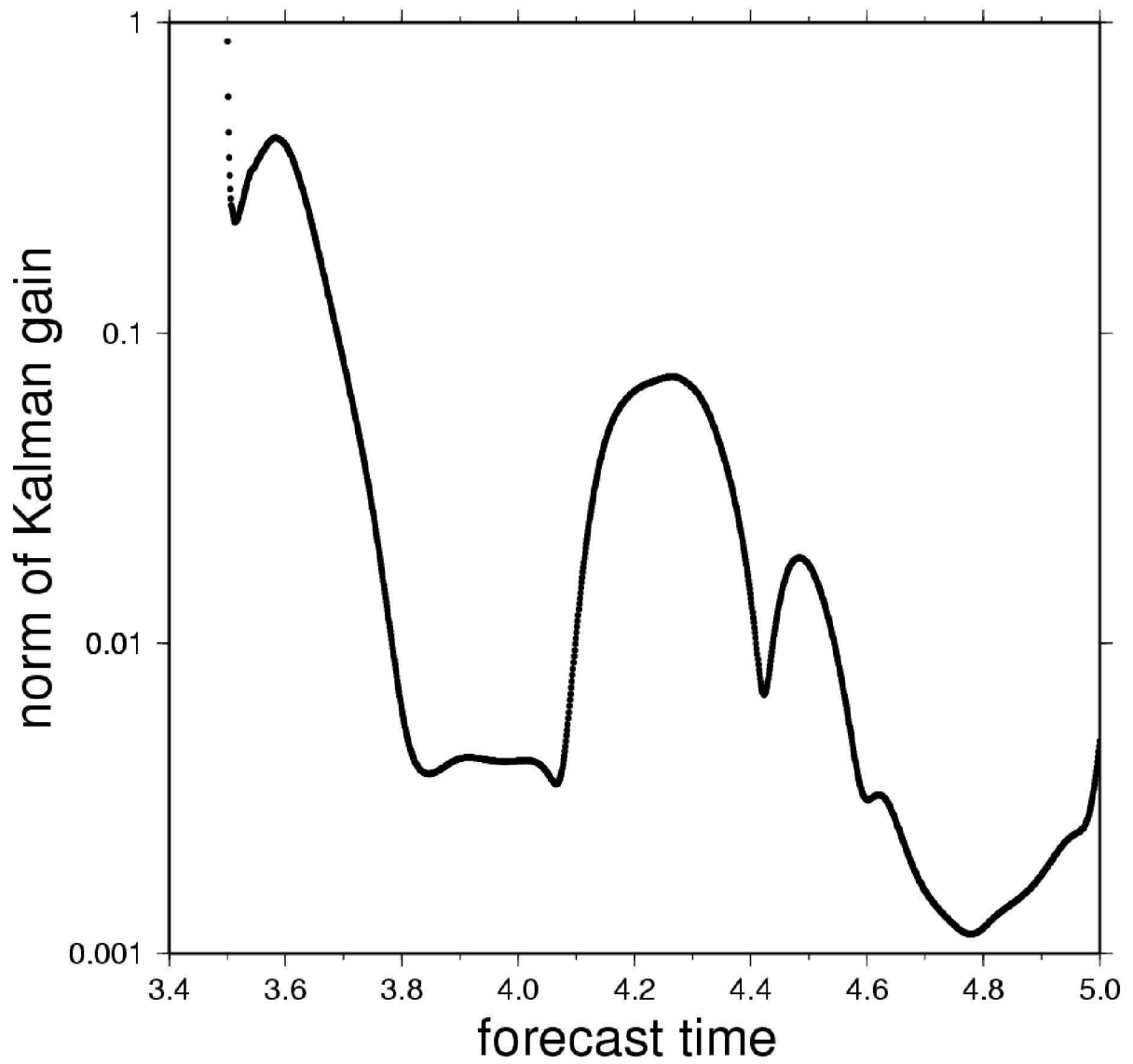
Figure 3.12: Norm of Kalman gain matrix. The range of the forecast time is same as Fig 3.11
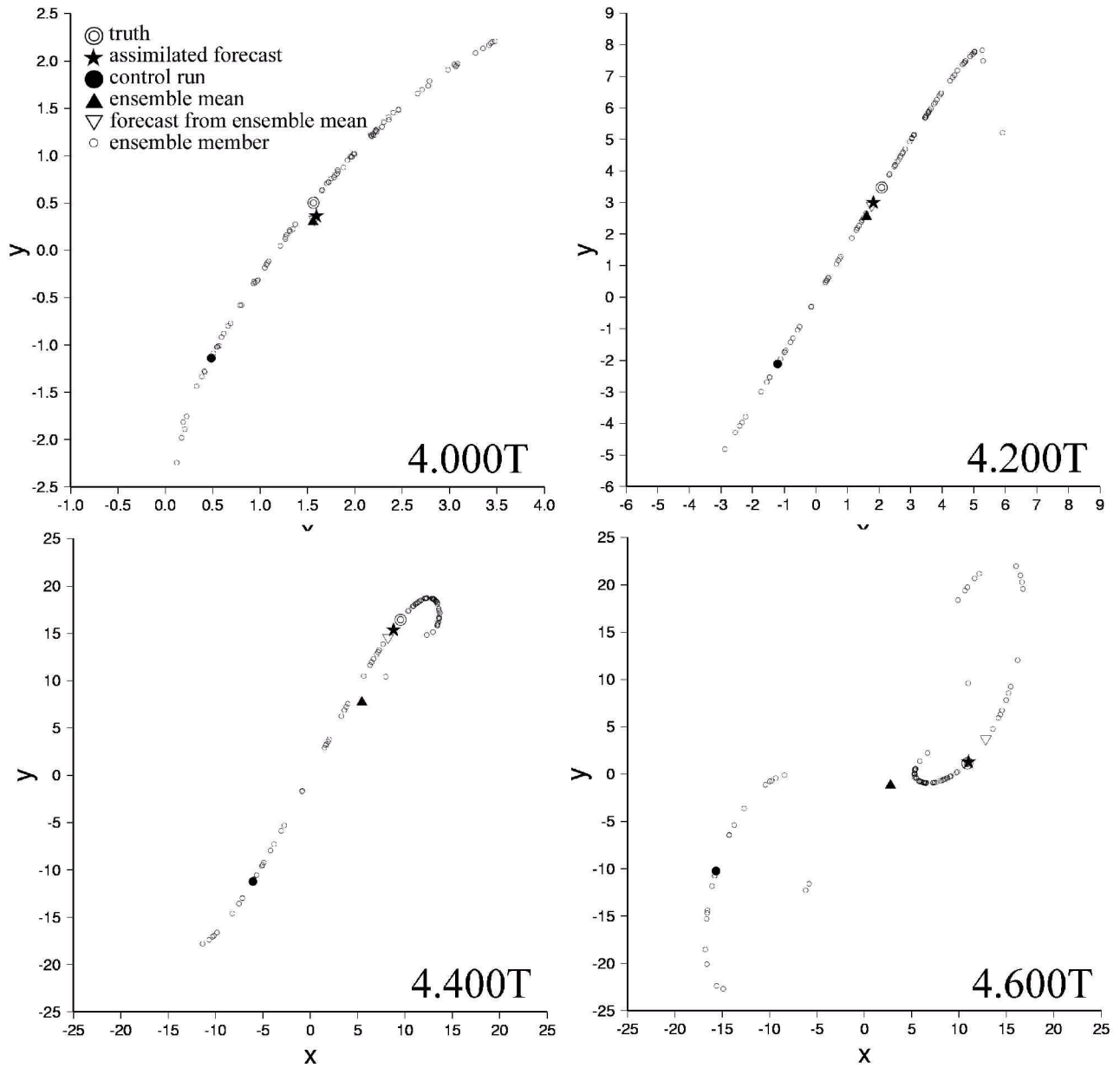
Figure 3.13: Evolution of the forecast distributions of the true run, control forecast, ensemble members, the ensemble mean, and assimilated forecast on x-y plane.
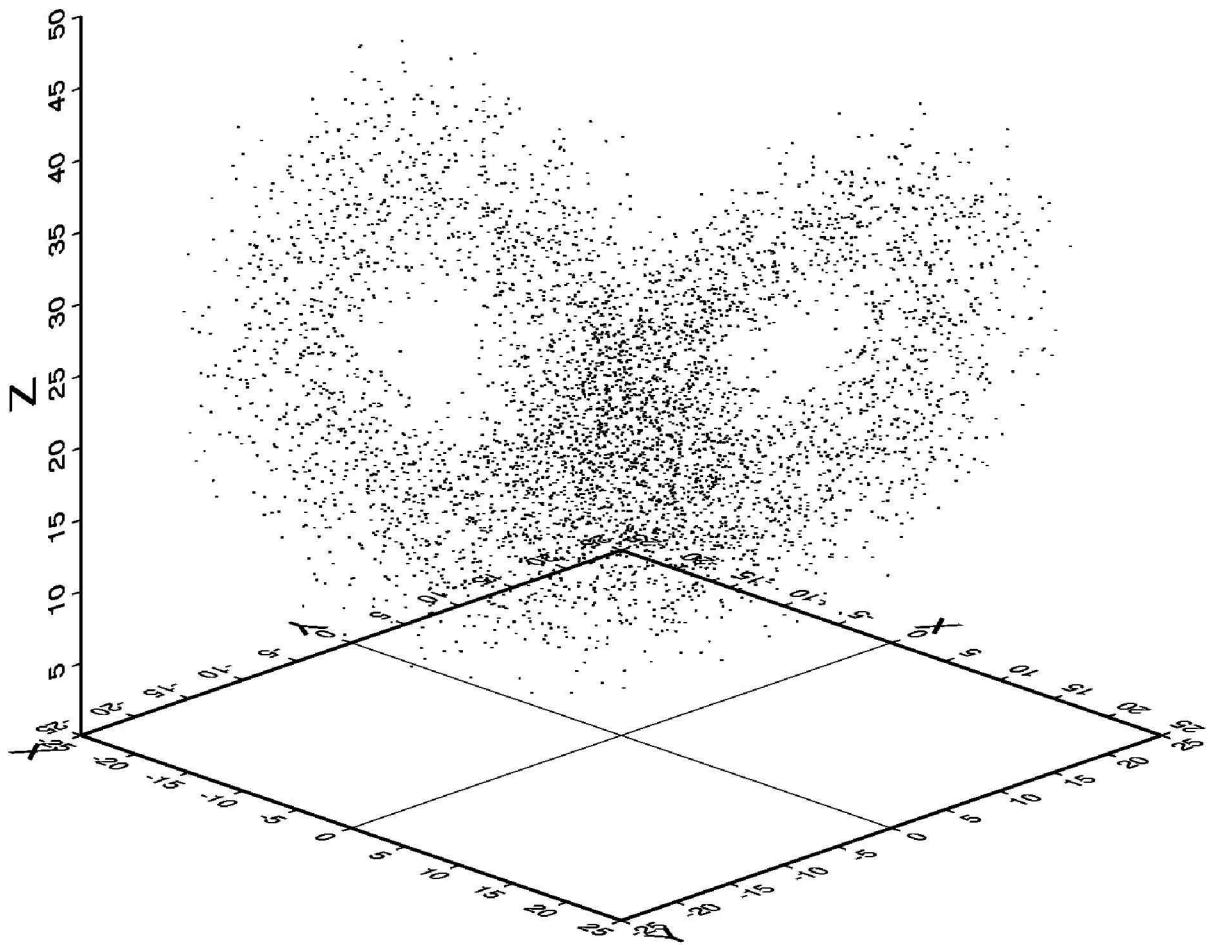
Figure 3.14: Distribution of the initial states of the 5000 sectors on the Lorenz model.

RMS error (Lorenz model)
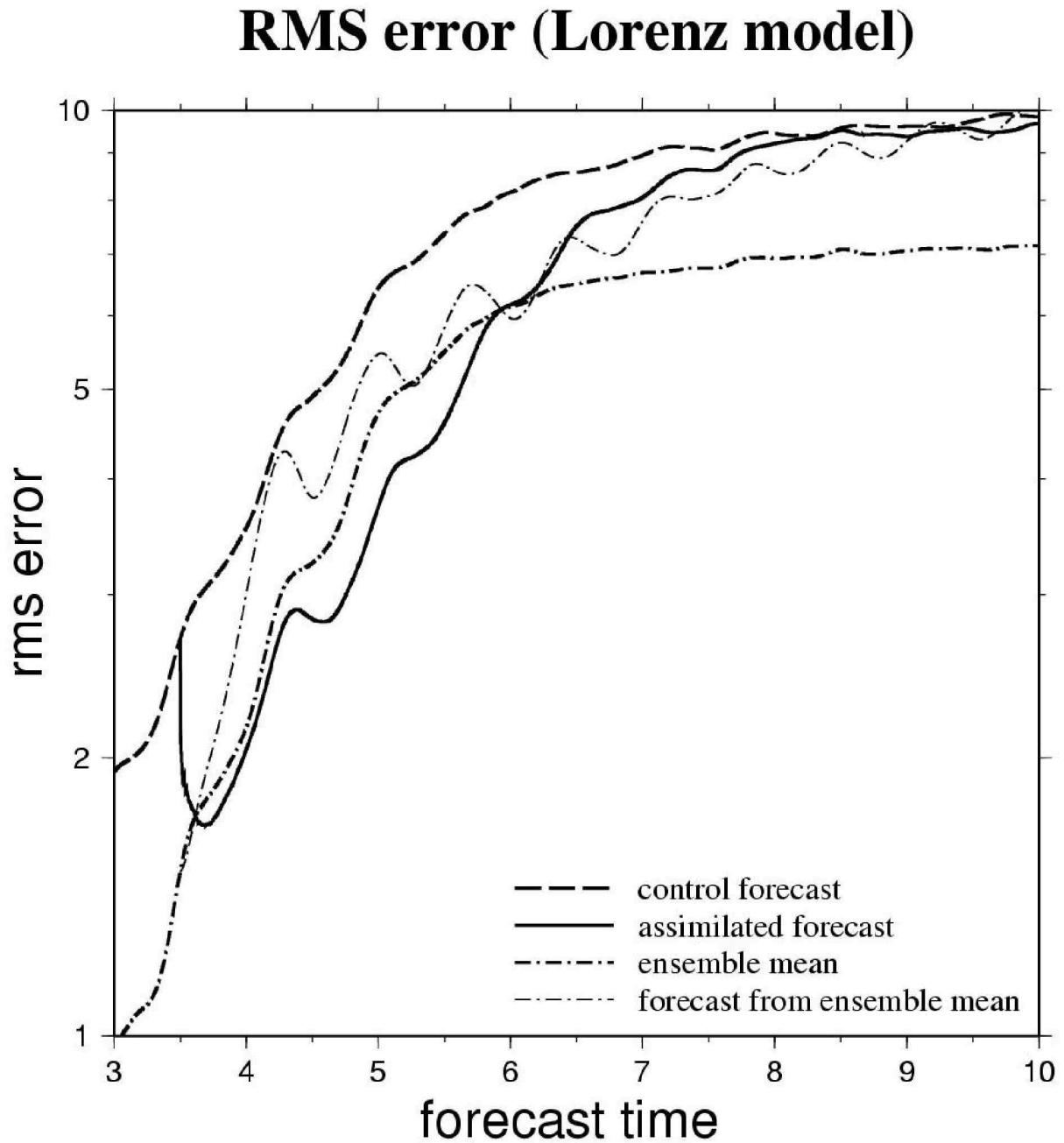
Figure 3.15: Averaged RMS error for the 5000 samples of the control forecast, ensemble mean, forecast from ensemble mean, and assimilated forecast. The forecast assimilation is started at time 3.5T.
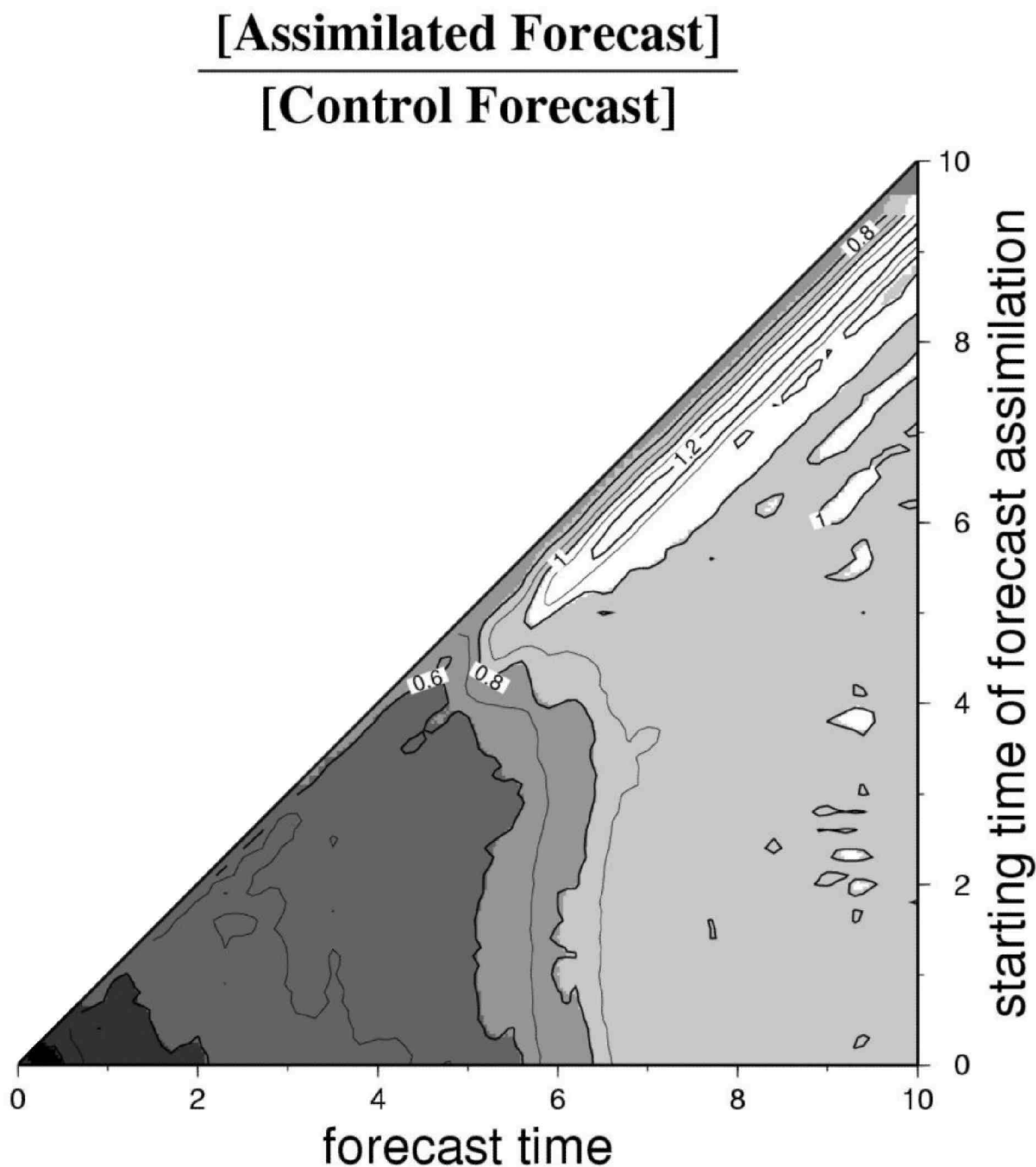
Figure 3.16: Ratio of RMS error of the assimilated forecast to the control forecast. The abscissa indicates the forecast time and the ordinate indicates the starting time of the forecast assimilation. The part of that the assimilated forecast is more skillful than the control forecast is shaded (the ratio is smaller than 1).
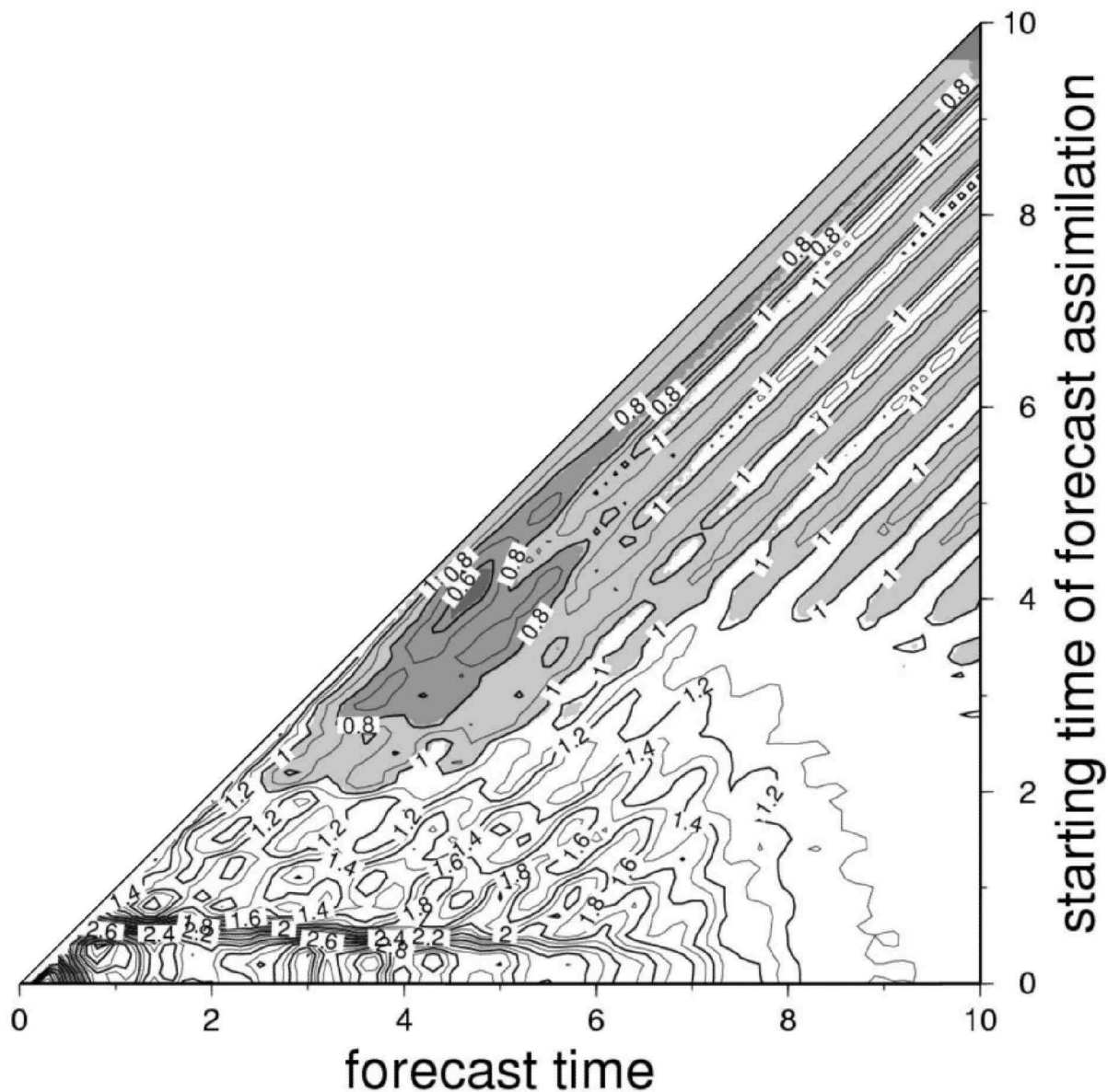
Figure 3.17: Similar to 3.16, but the ratio of RMS error of the assimilated forecast to the forecast from the ensemble mean.
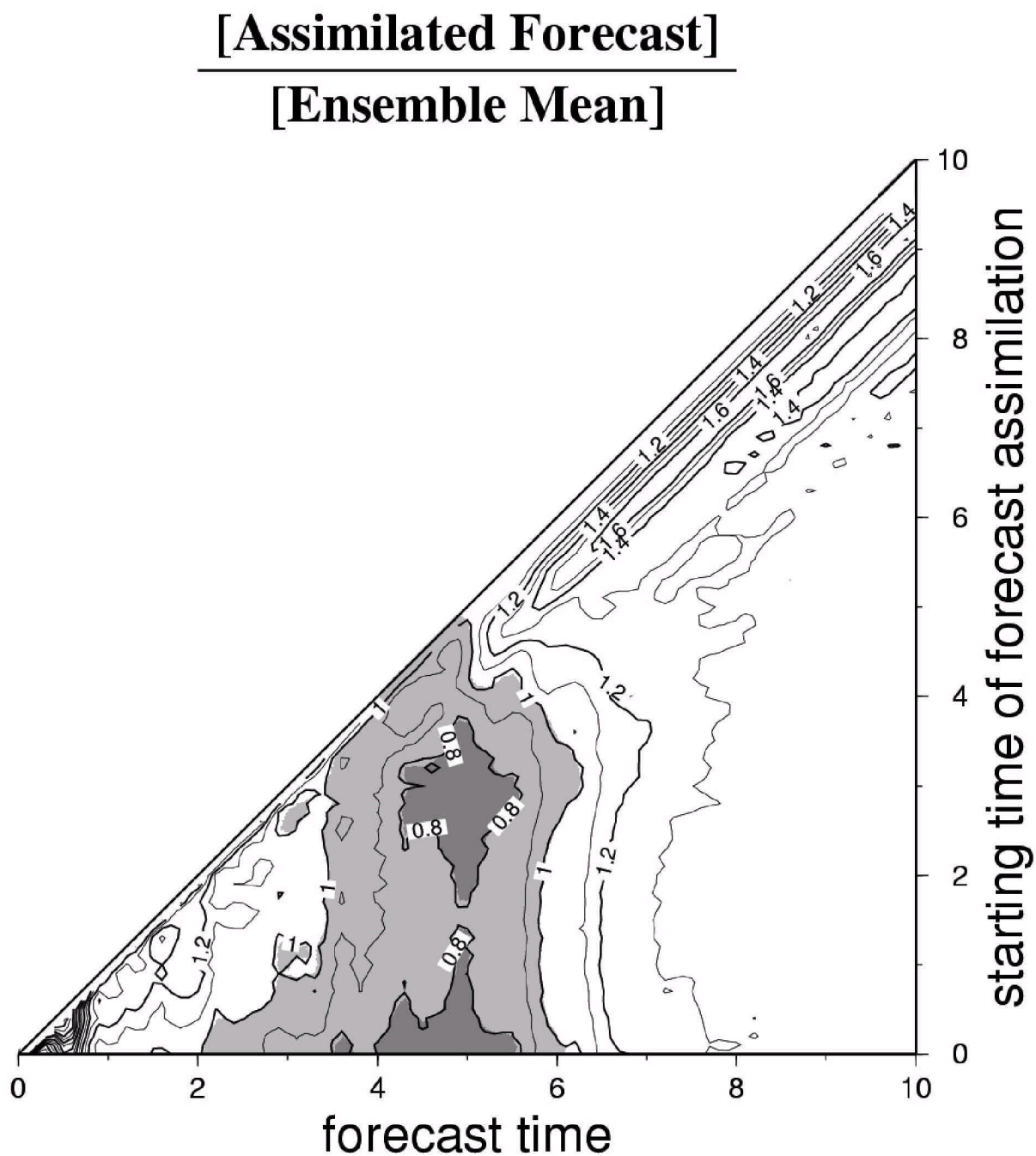
Figure 3.18: Similar to 3.16, but the ratio of RMS error of the assimilated forecast to the ensemble mean.

Chapter 4

Discussion

4.1   Atmospheric Predictability

Here, we discuss estimating the atmospheric predictability using the behavior of the difference of the analog pair. In the historical data, the RMS difference of the most analog pair is about half of the average RMS which represents the climatological mean range of the fluctuation (see Table 2.1). Then, the initial RMS difference of the analog pair represents as $E_0 = 1/2E_\infty$. Substituting $1/2E_\infty$ for E_0 in Eq. (2.3), we obtain,

$$\frac{dE}{dt} = \alpha\Big(\frac{E_\infty}{2}\Big) - \frac{\alpha}{E_\infty}\Big(\frac{E_\infty}{2}\Big)^2 = \frac{\alpha}{2}E_\infty - \frac{\alpha}{4}E_\infty. \tag{4.1}$$

This result indicates that the nonlinear effect contributes to the difference growth of the analog pair. Therefore, the components of the difference growth shown in Fig. 2.3 contain the nonlinear error growth effect as well as the linear effect. On the other hand, the local instability of the atmospheric global circulation is characterized by its singular vector (Buizza and Palmer 1995). The structure of the singular vector indicates the direction and amplitude of the initial perturbation by the tangent linear model. Figure 4.1 shows the vorticity maximum of the distribution of the first singular vectors for winter

case. Buizza and Palmer (1995) showed that the vorticity maxima of the singular vector are located in three areas in the Northern Hemisphere: the east Asian/west Pacific, the northern American/west Atlantic, and the northern subtropical African. The east Asian/west pacific and the northern American/west Atlantic regions are well known as areas of midlatitude cyclogenesis. The small perturbations generated at the west Pacific or Atlantic are propagated to downstream while they are developed with the cyclogenesis. Compared with Fig. 2.3, the vorticity maxima of the singular vectors are located just upstream of the difference growing areas of the analog pairs except the northern subtropical African region. The results suggested that the difference growing areas correspond to the arrival areas of the propagated perturbations by the cyclogenesis. Therefore, the difference growth rate in Eq. (2.6) principally results from the the cyclogenesis in the midlatitude.

The atmospheric predictability is often affected by the boundary conditions, such as El Niño and La Niña, and the atmospheric basic flow patterns, such as PNA and NAO. The atmospheric feature during PNA+ and NAO+ years apparently has slower difference growth than the average (see Table 2.5). On the other hand, La Niña and PNA- have faster difference growth than the average. In the case of hindcast experiment, the RMS error for the hindcast becomes clear inverse correlation with PNA index. The reason for the different growth rates by the different atmospheric conditions is considered by characteristics of the atmospheric inherent pattern as follows. During PNA- year, the atmospheric flow pattern tends to generate a blocking over the North Pacific (Renwick and Wallace 1996). The blocking denotes a breakdown in the prevailing tropospheric westerly flow at midlatitude, often associated with a split in the zonal jet and with persistent ridging at high latitudes (Rex 1950; Lejenäs and Økland 1983). The forecasting of the blocking is one of the main problems for the medium-range forecast due to its nonlinearity (Pelly and Hoskins 2003). So, the forecast skill is reduced in the vicinity of

the blocking. Therefore, the forecast error during the PNA- years tend to increase over the North Pacific region, which is shown in Fig. 2.16. Contrary to the PNA- years, the atmospheric flow pattern during the PNA+ year tends to generate non-blocking over the North Pacific. Additionally, the atmospheric variability during PNA+ years is smaller than other conditions in Fig. 2.9. Then the atmosphere tends to derive analogous flow pattern. Therefore, the difference growth rate during PNA+ years is smaller than other years. On the other hand, during El Niño (La Niña) years, the PNA+ (PNA-) pattern tends to occur relatively frequently (Horel and Wallace 1981). In the hindcast experiments, the map of the RMS error distribution is also similar to the PNA+ (PNA-). This result suggests that the influences of the El Niño or La Niña are secondary for the initial difference growth.

The hindcast verifies the role of the boundary and the basic flow pattern for the atmospheric predictability. Since the hindcast is retrospective forecast by the operational numerical forecast model, it is necessary to notice that the error growth element of the hindcast includes not only the atmospheric instability and nonlinearity but also the imperfectivity of the model and inevitable initial error. It is considered that the imperfectivity of the model contributes to the initial error growth in Fig. 2.18 until 2 or 3 days. Then the hindcast error significantly grows faster than the theoretical error growth. Additionally, the boundary effect and the basic flow pattern for the error growth disappears until 3 days hindcast in Fig. 2.14. After the 3 days, the inverse correlation between the RMS error and the PNA index is clearly seen. Then, the result suggests that the boundary condition and the basic flow pattern have inflenced the initial error growth.
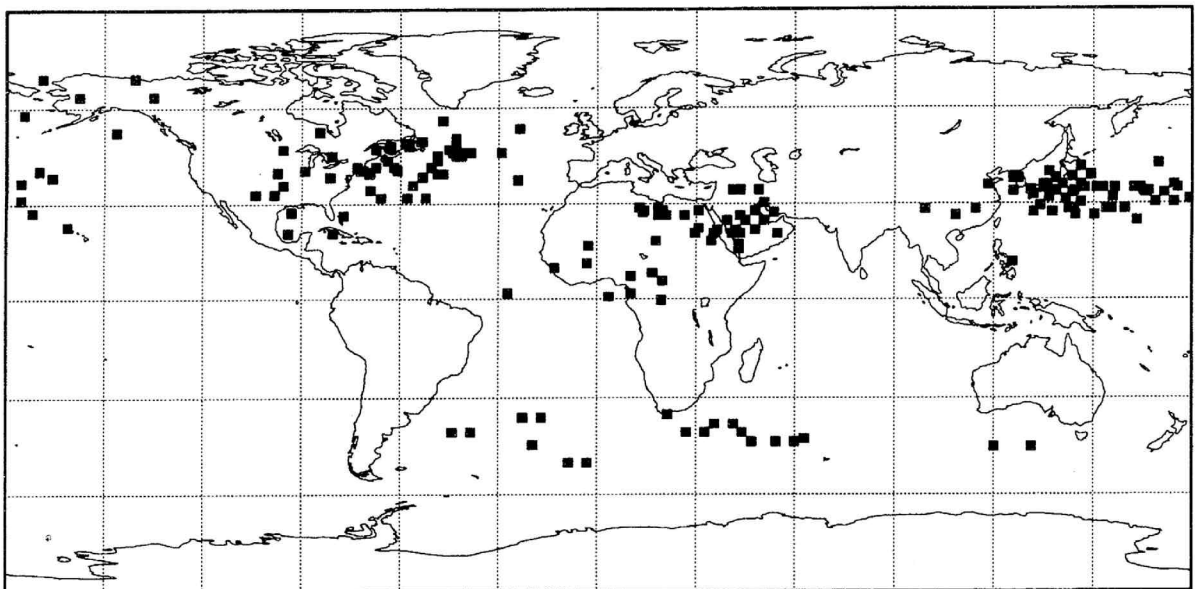
Figure 4.1: The distribution of the first singular vectors for winter case. The position of each singular vector is determined by its vorticity maximum. (From Buizza and Palmer 1995)

4.2 Forecast Assimilation

The consequence of the forecast assimilation using the 3D-Var results in the ensemble mean of the ensemble members. The reason is considered by characteristics of the 3D-Var. The assimilated values by the 3D-Var most closely fit both the predicted observations and forecast, as measured by the cost function in Eq. (3.3). At the first step of the forecast assimilation, the mean and variance of the error for the individual ensemble members from the truth theoretically equals to an error of the control forecast. Therefore, the observation and forecast error covariance matrix are the same matrix form in this situation. This means that the forecast assimilation derives the ensemble mean as the solution by 3D-Var. It is indicated that the forecast assimilation requires the time evolution of the forecast error with the dynamical process as well as the ensemble forecasts to improve the forecast skill.

The reasons for the superior performance of the assimilated forecast may be explained by the following characteristics of the Kalman filer. (1): Immediately after the starting point of the forecast assimilation, the assimilated forecast searches the true value contained in the ensemble members because $\mathbf{P}(t_i) = \mathbf{R}(t_i)$ has been assumed at the beginning. In this range the Kalman filter can quickly reduce the error of the assimilated forecast. (2): Then, in the direction of the error growth of the linearized Lorenz model, the Kalman filter can quickly reduce the error because $\mathbf{P}(i)$ contains information about the unstable direction by its history. (3): Conversely, near the saturation of the error as seen in Fig. 3.18 at time larger than 6.0T, the Kalman filter rather increases the error by assimilating ensemble members without information about the truth.

Based on the above remarks, let us assume that the distribution of the ensemble mem-

bers has been separated in two groups by the dynamical instability. Then the ensemble mean chooses just the center of the two separated groups regardless of the stability of the separated trajectories. In contrast, the trajectory of the assimilated forecast randomly chooses one of the two groups because the predicted observation is randomly selected. After the branch point, we assume that there are two results of the assimilated forecast: one becomes stable trajectory, and the other becomes unstable trajectory. In the former (latter) case, the assimilated forecast absorbs relatively less (much) positional information of the predicted observations that are included in the two groups. Repeating the forecast assimilations, the trajectory of the assimilated forecast in the former (latter) case becomes smooth (fluctuative), and it is difficult (easy) to shift to the unstable (stable) trajectory. Therefore, the assimilated forecast tends to move from the unstable to the stable trajectory. Since the stable trajectory is one of the most suitable solutions in the ensemble forecast, the forecast skill becomes superior to the ensemble mean in the nonlinear regime.

One point to notice in our examination is that the Gaussian distribution of the perturbations has been assumed around the true initial state for the ensemble members. Therefore, the mean of the ensemble members knows the true value at the beginning. After the nonlinear effect of the forecast error is dominated, the forecast assimilation would searches for the truth better than the ensemble mean. If the analysis errors and model errors are cancelled as expected in the multi-analysis multi-model, the forecast assimilation would be one of the viable approaches to the medium or extended range forecast.

Nevertheless, it is necessary to notice that the forecast assimilation has several problems to adopt the operational forecast system directly. The forecast assimilation for this experiment is applied to the Lorenz model that has only 3 degree of freedom dynamics compared with 100 ensemble members for the predicted observation. On the other hand, the operational numerical model has $10^6 \sim 10^7$ order of the degree of freedom compared

with $10 \sim 100$ ensemble members. The number of the ensemble members is extremely less than the model's degree of freedom. Therefore, there is a possibility that the forecast assimilation can not perform a good forecast skill for the operational forecast. Moreover, the Kalman filter requires to calculate the inverse matrix of the linearized model which has $10^6 \sim 10^7$ order size. The calculation steps of n-th order of the matrix inverse requires n^3 times by Gaussian elimination. It is extremely difficult to calculate the inverse matrix in spite of using the latest supercomputer. Therefore, the forecast model for the forecast assimilation is replaced by the use of simplifying assumptions such as a lower order model. However, the forecast assimilation applied to the large numerical model would be reserved for a future works.

Chapter 5

Conclusions

In the first part of this study, the difference growth rate for the atmosphere was examined based on analog weather maps in the NCEP/NCAR reanalysis for 54 years. Although a total of 185,547,600 pairs of the weather maps are searched, there are no good analog pairs to investigate the difference growth rate for a sufficiently small initial difference E_0 of the analog pairs. However, the behavior of the difference of the analog pair is approximated by a quadratic error growth model which allows an exponential difference growth rate. The behavior of the small difference is explained by a quadratic error growth model. To fit the quadratic error growth model to the scattergram between the limit of predictability P and E_0, it is estimated that P extends 2.88 days when E_0 is reduced to $1/e$ for sufficiently small E_0. The difference growth rate is principally resulted from the cyclogenesis in the midlatitude because the difference growing regions for the analog pairs are located at the north Pacific and the north Atlantic.

The difference growth rate is variable by the boundary condition, such as El Niño and La Niño, and atmospheric basic flow pattern, such as PNA and NAO. In the case of PNA+ and NAO- (e-folding time of 3.17 and 3.07 days, respectively), the difference of the

analog pairs grows slower than the average. Conversely, in the case of La Niña and PNA-(e-folding time of 2.69 and 2.72 days, respectively), the difference grows faster than the average. Comparisons of the error growth during the El Niño/La Niña, PNA+/PNA-, and NAO+/NAO- were made by the hindcast. Little difference of the difference growth could be seen in the cast of El Niño/La Niño and NAO+/NAO-. Conversely, the difference grows faster during the PNA- years than the PNA+ year. However, since the atmospheric flow pattern during the El Niño (La Niña) years tend to produce the PNA+ (PNA-) pattern, the influences of the El Niño or La Niña were secondary for the initial difference growth.

In the next part of this study, a new type of ensemble forecast assimilation technique was developed in order to improve the forecast skill in the nonlinear dynamical system. The forecast assimilation is an analysis technique in which true value contained in each ensemble forecast is accumulated into a single assimilated forecast such as a data assimilation. For the experiments, we used a Lorenz model, and a Kalman filter was applied for the forecast assimilation.

The experiments were started by calculating 101 members of the ensemble forecast in which the initial error with Gaussian distribution was superimposed around the true run, and one of the members was arbitrarily selected as a control forecast. The experiments of the forecast assimilation were repeated 5000 times for different sectors of the solution trajectory to obtain the statistical significance of the results. The distribution of the ensemble members was stretched by a linear instability of the error growth at the beginning of the forecast. After that, the nonlinear effect became dominant to distort the distribution. The forecast assimilation was then started when the errors of the ensemble forecasts have grown to a various threshold of the forecast time.

It was demonstrated that the forecast skill of the assimilated forecast is always superior

to the control forecast. In the range of the small RMS error of the ensemble forecasts, the skill of the assimilated forecast is inferior to the ordinary ensemble mean. Since the distribution of the ensemble forecasts is similar to the hyper ellipsoid until the nonlinear effect becomes dominant, the center of the distribution is always close to the truth. After the distribution was folded by the nonlinear effect, the ensemble mean is detached from the distribution of the ensemble members. From 3.0T to 6.0T of the forecast time in Fig. 3.18, the skill of the assimilated forecast was superior to the ensemble mean. After 6.0T forecast time, the skill of the assimilated forecast is poorer than the ensemble mean, since the ensemble members have little positional information of the truth for saturated forecast errors of the ensemble members. Nevertheless, the assimilated forecast has a good performance at the intermediate range where the nonlinear growth dominates but is not saturated.

Acknowledgments

References

Alhamed, A., and S. Lakshmivarahan, 2002: Cluster analysis of multimodel ensemble data from SAMEX. *Mon. Wea. Rev.*, **130**, 226–256.

Anderson, J. L., 1997: The impact of dynamical constraints on the selection of initial conditions for ensemble predictions: low-order perfect model results. *Mon. Wea. Rev.*, **125**, 2969–2983.

Anderson, J. L., 2001: An ensemble adjustment Kalman filter for data assimilation. *Mon. Wea. Rev.*, **129**, 2884–2903.

Anderson, J. L., and S. L. Anderson, 1999: A Monte Carlo implementation of the non-linear filtering problem to produce ensemble assimilation and forecasts. *Mon. Wea. Rev.*, **127**, 2741–2758.

Andersson, E., J. Haseler, P. Undén, P. Courtier, G. Kelly, D. Vasiljević, C. Branković, C. Cardinali, C. Gaffard, A. Hollingsworth, C. Jakob, P. Janssen, E. Klinker, A. Lanzinger, M. Miller, F. Rabier, A. Simmons, B. Strauss, J. N. Thépaut, and P. Viterbo 1998: The ECMWF implementation of three-dimensional variational assimilation (3D-Var). III: Experimental results. *Q. J. R. Meteorol. Soc.*, **124**, 1831–1860.

Andersson, E., A. Hollingsworth, G. Kelly, P. Lönnberg, J. Pailleux, and Z. Zhang, 1991: Global observing system experiments on operational statistical retrievals of satellite

sounding data. *Mon. Wea. Rev.*, **119**, 1851–1864.

Barsugli, J. J., J. s. Whitaker, A. F. Loughe, P. D. Sardeshmukh, and Z. Toth, 1999: The effect of the 1997/98 El Niño on individual large-scale weather events. *Bull. Amer. Meteor. Soc.*, **80**, 1399–1411.

Bouttier, F., and P. Courtier, 1999: Data assimilation concepts and methods. *ECMWF Meteorological Training Course Letter Series.*

Buizza, R., 1997: Potential forecast skill of ensemble prediction and spread and skill distributions of the ECMWF ensemble prediction system. *Mon. Wea. Rev.*, **125**, 99–119.

Buizza, R., J. Barkmeijer, T. N. Palmer, and D. S. Richardson, 2000: Current status and future developments of the ECMWF ensemble prediction system. *Meteorol. Appl.*, **7**, 163–175.

Buizza, R., and T. N. Palmer, 1995: The singular-vector structure of the atmospheric global circulation. *J. Atmos. Sci.*, **52**, 1434–1456.

Burgers, G., P. J. van Leeuwen, and G. Evensen, 1998: Analysis scheme in the ensemble assimilation and forecasts. *Mon. Wea. Rev.*, **126**, 1719–1724.

Chen, W. Y., 1989: Estimate of dynamical predictability from NMC DERF experiments. *Mon. Wea. Rev.*, **117**, 1227–1236.

Chen, W. Y., and H. M. Van den Dool, 1997: Atmospheric predictability of seasonal, annual, and decadal climate means and the role of the ENSO cycle: a model study. *J. Climate*, **10**, 1236–1254.

Chu, P. C., 1999: Two kinds of predictability in the Lorenz system. *J. Atmos. Sci.*, **56**, 1427–1432.

Courtier, P., 1997: Variational methods. *J. Meteor. Soc. Japan*, **75**, 211–218.

Courtier, P., E. Andersson, W. Heckley, J. Pailleux, D. Vasiljević, M. Hamrud, A. Hollingsworth, F. Rabier, and M. Fisher, 1998: The ECMWF implementation of three-dimensional variational assimilation (3D-Var). I: Formulation. *Q. J. R. Meteorol. Soc.*, **124**, 1783–1807.

Dalcher, A. and E. Kalnay, 1987: Error growth and predictability in operational ECMWF-forecasts. *Tellus*, **39**, 474–491.

Daley, R., 1991: *Atmospheric data analysis.* Cambridge University Press, 457 pp.

Daley, R., 1997: Atmospheric data assimilation. *J. Meteor. Soc. Japan*, **75**, 319–329.

Doblas-Rayes, F. J., M. Déqué, and J.-P. Piedelievre, 2000: Multi-model spread and probabilistic seasonal forecasts in PROVOST. *Q. J. R. Meteorol. Soc.*, **126**, 2069–2087.

Errico, R. M., R. Langland, and D. P. Baumhefner, 2002: The workshop in atmospheric predictability. *Bull. Amer. Meteor. Soc.*, **83**, 1341–1343.

Evensen, G., 1994: Sequential data assimilation with a nonlinear quasigeostrophic model using Monte Carlo methods to forecast error statistics. *J. Geophys. Res.*, **99** (C5), 10143–10167.

Evensen, G., 1997: Advanced data assimilation for strongly nonlinear dynamics. *Mon. Wea. Rev.*, **125**, 1342–1354.

Evensen, G. and N. Fario, 1997: Solving for the generalized inverse of the Lorenz model. *J. Meteor. Soc. Japan*, **75**, 229–243.

Fritsch, J. M., J. Hilliker, J. Ross. and R. L. Vislocky, 2000: Model consensus. *Wea. Forecasting*, **15**, 571–582.

Gekaro, R., R. Buizza, T. N. Palmer, and E. Klinker, 1997: Sensitivity analysis of the forecast errors and the construction of optimal perturbation using singular vectors. *J. Atmos. Sci.*, **55**, 1012–1037.

Gutzler, D. S. and J. Shukla, 1984: Analogs in the wintertime 500 mb height field. *J. Atmos. Sci.*, **41**, 177–189.

Hamill, T. M., C. Snyder, and R. E. Morss, 2000: A comparison of probabilistic forecasts from bred, singular-vector, and perturbed observation ensembles. *Mon. Wea. Rev.*, **128**, 1835–1851.

Hamill, T. M., J. S. Whitaker, and C. Snyder, 2001: Distance-dependent filtering of background error covariance estimates in an ensemble Kalman filter. *Mon. Wea. Rev.*, **129**, 2776–2790.

Hamill, T. M., J. S. Whitaker, and X. Wei, 2003: Ensemble re-forecasting: improving medium-range forecast skill using retrospective forecasts. *Mon. Wea. Rev.*. (submitted)

Harrison, M. S. J., T. N. Palmer, D. S. Richardson, and R. Buizza, 1999: Analysis and model dependencies in medium-range ensembles: two transplant case-studies. *Q. J. R. Meteorol. Soc.*, **125**, 2487–2515.

Horel, J. D., and J. M. Wallace, 1981: Planetary-scale atmospheric phenomena associated with the southern oscillation. *Mon. Wea. Rev.*, **109**, 813–829.

Hoskins, B. J., and K. I. Hodges, 2002: New perspectives on the Northern Hemisphere winter storm tracks. *J. Atmos. Sci.*, **59**, 1041–1061.

Houtekamer, P. L., and J. Derome, 1995: Methods for ensemble prediction. *Mon. Wea. Rev.*, **123**, 2181–2196.

Hurrell, J. W., 1995: Decadal trends in the north atlantic oscillation: regional temperatures and precipitation. *Science*, **269**, 676–679.

Kalman, R., and R. Bucy, 1961: New results in linear prediction and filtering theory *Trans. AMSE, J. Basic Eng.*, **83D**, 95-108.

Kalnay, E., 2002: *Atmospheric modeling data assimilation and predictability.* Cambridge University Press, 341 pp.

Kalnay, E., M. Kanamitsu, R. Kistler, W. Collins, D. Deaven, L. Gandin, M. Iredell, S. Saha, G. White, J. Woollen, Y. Zhu, M. Chelliah, W. Ebisuzaki, W. Higgins, J. Janowiak, K. C. Mo, C. Ropelewski, J. Wang, A. Leetmaa, R. Reynolds, R. Jenne, and D. Joseph, 1996: The NCEP/NCAR 40-year reanalysis project. *Bull. Amer. Meteor. Soc.*, **77**, 437–471.

Kalnay, E., S. J. Lord, and R. D. McPherson, 1998: Maturity of operational numerical weather prediction: medium range. *Bull. Amer. Meteor. Soc.*, **79**, 2753–2769.

Kharin, V. V., and F. W. Zwiers, 2002: Climate prediction with multimodel ensembles. *J. Climate*, **15**, 793–799.

Kistler, R., E. Kalnay, W. Collins, S. Saha, G. White, J. Woollen, M. Chelliah, W. Ebisuzaki, M. Kanamitsu, V. Kousky, H. Van den Dool, R. Jenne, and M. Fiorino, 2001: The NCEP/NCAR 50-year reanalysis: monthly means CD-ROM and documentation. *Bull. Amer. Meteor. Soc.*, **82**, 247–268.

Klinker, E., F. Rabier, G. Kelly, and J. f. Mahfouf, 2000: The ECMWF operational implementation of four-dimensional variational assimilation. III: Experimental results and diagnostics with operational configuration. *Q. J. R. Meteorol. Soc.*, **126**, 1191–1215.

Krishnamurti, T. N., C. M. Kishtawal, T. E. LaRow, D. R. Bachiochi, Z. Zhanf, C. E. Willifor, S. Gadgil, and S. Surendran, 1999: Improved weather and seasonal climate forecasts from multimodel superensemble. *Science*, **285**, 1548–1550.

Krishnamurti, T. N., C. M. Kishtawal, Z. Zhanf, T. LaRow, D. Bachiochi, and E. Williford, 2000: Multimodel ensemble forecasts for weather and seasonal climate. *J. Climate*, **13**, 4196–4216.

Lau, N.-C., and M. J. Nath, 1994: A modeling study of the relative roles of tropical and extratropical SST anomalies in the variability of the global atmosphere-ocean system. *J. Climate*, **7**, 1184–1207.

Lejenäs, H. and H. Økland, 1983: Characteristics of Northern Hemisphere blocking as determined from a long time series of observational data. *Tellus*, **35**, 350–362.

Lin, H., and J. Derome, 1996: Changes in predictability associated with the PNA pattern. *Tellus*, **48A**, 553–571.

Lorenc, A. C., 1981: A global three-dimensional multivariate statistical interpolation scheme. *Mon. Wea. Rev.*, **109**, 701–721.

Lorenz, E. N., 1963: Deterministic nonperiodic flow. *J. Atmos. Sci.*, **20**, 130–141.

Lorenz, E. N., 1969a: Three approaches to atmospheric predictability. *Bull. Amer. Meteor. Soc.*, **50**, 345–349.

Lorenz, E. N., 1969b: Atmospheric predictability as revealed by naturally occurring analogues. *J. Atmos. Sci.*, **26**, 636–646.

Lorenz, E. N., 1982: Atmospheric predictability experiments with a large numerical model. *Tellus*, **34**, 505–513.

Mahfouf, j. f., and F. Rabier, 2000: The ECMWF operational implementation of four-dimensional variational assimilation. I: Experimental results with improved physics. *Q. J. R. Meteorol. Soc.*, **126**, 1171–1190.

Miller, R. N., M. Ghil, and F. Gauthiez, 1994: Advanced data assimilation in strongly nonlinear dynamical systems. *J. Atmos. Sci.*, **51**, 1037–1056.

Molteni, F., R. Buizza, T. N. Palmar and T. Petroliagis, 1996: The ECMWF ensemble prediction system: methodology and validation. *Q. J. R. Meteorol. Soc.*, **122**, 73–119.

Mukougawa, H., M. Kimoto, and S. Yoden, 1991: A relationship between local error growth and quasi-stationary states: case study in the Lorenz system. *J. Atmos. Sci.*, **48**, 1231–1237.

Murphy, J. M., 1988: The impact of ensemble forecast on predictability. *Q. J. R. Meteorol. Soc.*, **114**, 463–493.

Mylne, K. R., R. E. Evans, and R. T. Clork, 2002: Multi-model multi-analysis ensembles in quasi-operational medium-range forecasting. *Q. J. R. Meteorol. Soc.*, **128**, 361–384.

Nohara, D. and H. L. Tanaka, 2001: Logarithmic relation between the initial error and predictability for the barotropic component of the atmosphere. *J. Meteor. Soc. Japan*, **79**, 161–171.

Nohara, D. and H. L. Tanaka, 2004: Development of prediction model using ensemble forecast assimilation in nonlinear dynamical system. *J. Meteor. Soc. Japan* (in press)

Palmer, T. N., 1993: Extended range atmospheric prediction and the Lorenz model. *Bull. Amer. Meteor. Soc.*, **74** 49–66.

Palmer, T. N., Č. Branković, and D. S. Richardson, 2000: A probability and decision-model analysis of PROVOST seasonal multi-model ensemble integration. *Q. J. R. Meteorol. Soc.*, **126**, 2012–2033.

Parrish, D. F., and J. C. Derber, 1992: The National Meteorological Center's spectral statistical interpolation analysis system. *Mon. Wea. Rev.*, **120**, 1747–1763.

Pelly, J. L., and B. J. Hoskins, 2003: How well does the ECMWF ensemble prediction system predict blocking?. *Q. J. R. Meteorol. Soc.*, **129**, 1683–1702.

Press, W. E., S. A. Teukolsky, W. T. Vetterling, and B. P. Flannery, 1992: *Numerical recipes in fortran 77: second edition.* Cambridge University Press, 963 pp.

Rabier, F., H. Järvinen, E. Klinker, J. F. Mahfouf, and A. Simmons, 2000: The ECMWF operational implementation of four-dimensional variational assimilation. I: Experimental results with simplified physics. *Q. J. R. Meteorol. Soc.*, **126**, 1143–1170.

Rabier, F., A. McNally, E. Andersson, P. Courtier, P. Undén, J. Eyre, A. Hollingsworth, and F. Bouttier, 1998: The ECMWF implementation of three-dimensional variational assimilation (3D-Var). II: Structure. *Q. J. R. Meteorol. Soc.*, **124**, 1809–1829.

Renwick, J. A., and J. M. Wallace, Relationships between north Pacific wintertime blocking, El Niño, and PNA pattern. *Mon. Wea. Rev.*, **124**, 2071–2076.

Rex, D. P., 1950: Blocking action in the middle troposphere and its effect upon regional climate. Part II: The climatology of blocking actions. *Tellus*, **2**, 275–301.

Reynolds, R. W., and T. M. Smith, 1994: Improved global sea surface temperature analyses using optimum interpolation. *J. Climate*, **7**, 929–948.

Saltzman, B., 1962: Finite amplitude free convection as an initial value problem. *J. Atmos. Sci.*, **19**, 329–341.

Savijarvi, H., 1995: Error growth in a large numerical forecast system. *Mon. Wea. Rev.*, **123**, 212–221.

Schubert, S. D. and M. Suarez, 1989: Dynamical predictability in a simple general circulation model: average error growth. *J. Atmos. Sci.*, **46**, 353–370.

Shaw, D. B., P. Lönnberg, A. Hollingsworth and P. Undén, 1987: The 1984/1985 revisions of the ECMWF assimilation system. *Q. J. R. Meteorol. Soc.*, **122**, 533–566.

Sheng, J., 2002: GCM experiments on changes in atmospheric predictability associated with the PNA pattern and tropical SST anomalies. *Tellus*, **54A**, 317–329.

Shukla, J., J. Anderson, D. Baumhefner, C. Brankovic, Y. Chang, E. Kalnay, L. Marx, T. Palmer, D. Paolino, J. Ploshay, S. Schubert, D. Straus, M. Suarez, and J. Tribbia, 2000: Dynamical seasonal prediction. *Bull. Amer. Meteor. Soc.*, **81**, 2593–2606.

Simmons, A. J., R. Mureau and T. Petroliagis, 1995: Error growth and estimates of predictability from the ECMWF forecasting system. *Q. J. R. Meteorol. Soc.*, **121**, 1739–1771.

Sparrow, C., 1982: *The Lorenz Equations: Bifurcations, Chaos, and Strange Attractors.* Springer-Verlag, 269 pp.

Stroe, R, and J. F. Royer, 1993: Comparison of different error growth formulas and predictability estimation in numerical extended-range forecasts. *Ann Geophysicae*, **11**, 296–316.

Tanaka, H. L., 1991: a numerical simulation of amplification of low-frequency planetary waves and blocking formations by the upscale energy cascade. *Mon. Wea. Rev.*, **119**, 2919–2935.

Tanaka, H. L., 1998: Numerical simulation of a life-cycle of atmosphere blocking and the analysis of potential vorticity using a simple barotropic model. *J. Meteo. Soc. Japan*, **76**, 983–1008.

Tewelws, S., and H. Wobus, 1954: Verification of prognostic charts. *Bull. Amer. Meteor. Soc.*, **35**, 455–463.

Toth, Z., 1991: Estimate of atmospheric predictability by circulation analogs. *Mon. Wea. Rev.*, **119**, 65–72.

Toth, Z., and E. Kalnay, 1993: Ensemble forecasting at NMC: The generation of perturbations. *Bull. Amer. Meteor. Soc.*, **74**, 2317–2330.

Toth, Z., and E. Kalnay, 1997: Ensemble forecasting at NCEP and the breeding method. *Mon. Wea. Rev.*, **125**, 3297–3319.

Trevisan, A. and F. Pancotti, 1998: Periodic orbits, Lyapunov vectors, and singular Vectors in the Lorenz system. *J. Atmos. Sci.*, **55**, 390–398.

Van den Dool, H. M., 1994: Searching for analogues, how long must we wait?. *Tellus*, **46A**, 314–324.

Wallace, J. M., and D. S. Gutzler, 1981: Teleconnection in the geopotential height field during the Northern Hemisphere winter. *Mon. Wea. Rev.*, **109**, 784–812.

Williford, C. E., T. N. Krishnamurti, R. C. Torres, and S. Cocke, 2003: Real-time multimodel superensemble forecasts of atlantic tropical systems of 1999. *Mon. Wea. Rev.*, **131**, 1878–1894.

List of Symbols

E RMS difference in 500 hPa geopotential height

E_0 Initial RMS difference

E_l One standard deviation of E from the long term mean of the fluctuation in the observed atmosphere

E_∞ Climatological mean of the atmospheric fluctuation of E

H Observation operator

$\mathbf{H}$ Linearized observation operator

$\mathbf{I}$ Identity matrix

J Cost function in 3D-Var

$\mathbf{K}$ Kalman gain matrix

M Nonlinear forecast model

$\mathbf{M}$ Tangent linear model matrix of the nonlinear forecast model

P Limit of predictability

$\mathbf{P}_f$ Forecast error covariance matrix

$\mathbf{P}_a$ Analysis error covariance matrix

$\mathbf{Q}$ Model error covariance matrix

$\mathbf{R}$ Observation error covariance matrix

$\mathbf{R}_e$ Ensemble covariance matrix

$\mathbf{x}_a$ Analysis vector

$\mathbf{x}_f$ Background vector

$\mathbf{x}_o$ Observation vector

$\mathbf{x}_t$ True state vector

Z Geopotential hight

α Error growth rate

β Parameter in Lorenz model

γ Parameter in Lorenz model

σ Parameter in Lorenz model